

©2009

Goki Eda

ALL RIGHTS RESERVED

SOLUTION-PROCESSED THIN FILMS FOR ELECTRONICS FROM
SINGLE-WALLED CARBON NANOTUBES AND GRAPHENE

by

GOKI EDA

A Dissertation submitted to the
Graduate School-New Brunswick
Rutgers, The State University of New Jersey
in partial fulfillment of the requirements

for the degree of

Doctor of Philosophy

Graduate Program in Materials Science and Engineering

written under the direction of

Professor Manish Chhowalla

and approved by

New Brunswick, New Jersey

October, 2009

ABSTRACT OF THE DISSERTATION

SOLUTION-PROCESSED THIN FILMS FOR ELECTRONICS FROM SINGLE-WALLED CARBON NANOTUBES AND GRAPHENE

By Goki Eda

Dissertation Director: Prof. Manish Chhowalla

Single-walled carbon nanotubes (SWNTs) and graphene are sp^2 hybridized carbon nanostructures which exhibit extraordinary electronic properties arising from their unique energy dispersions and dimensionalities. A major issue preventing implementation of these materials into integrated electronic devices is the absence of large-scale controllable synthesis and subsequent manipulation. To circumvent this issue, solution processing of SWNTs and graphene has been proposed. Deposition of thin film networks allows the realization of a new class of materials that are useful for large-area or “macro-electronics” on flexible and inexpensive platforms.

In this thesis, controllable and efficient solution-based deposition of SWNT and graphene thin film networks and their opto-electronic properties are investigated. Topics such as material dynamics in liquid, chemical structures, defects, morphology, and doping are studied utilizing various spectroscopy and microscopy analysis along with complementary electrical measurements. Further insight is provided through demonstrations of proof-of-principle thin film transistors, organic photovoltaics, and field emitters based on solution-processed SWNT and graphene thin films.

ACKNOWLEDGEMENTS

I would like to express my sincere gratitude to my supervisor, Prof. Manish Chhowalla, for his continuous support, guidance, and prodding throughout my graduate career. His enthusiasm and optimism has made my research experience truly enjoyable. I cannot thank him enough for everything he has taught me. I would also like to express my appreciation for the current and former members of the group for all the support and creating a joyful environment to work in. I would especially like to thank Dr. Giovanni Fanchini for his intellectual advice and thought-provoking ideas. I feel very lucky to have worked with him. My thanks also go to Dr. Alokik Kanwal and Dr. Steve Miller for helping me get started in the first year and always being good consultants. I would also like to thank Dr. Cecilia Mattevi and Dr. Hisato Yamaguchi for fruitful discussions and significantly contributing to this thesis. I also enjoyed working with Bhavin Parekh, Varun Gupta, Wojtek Tutak, Sara Reynaud, and HoKwon Kim and thank them for their friendship. My appreciation also goes to my thesis committee members, Prof. Dunbar Birnie III, Prof. Lisa Klein, Prof. George Sigel, Jr., Prof. Adrian Mann, and Prof. Eric Garfunkel, for technical advice and support.

I am grateful for collaborators inside and outside Rutgers University. From Rutgers, I enjoyed the pleasant collaborations and discussions with Sarika Phadke, Maryam Abazari, Ozgur Celik, Daniel Mastrogiovanni, Bumsu Lee, Dr. Wooseok Kim, Mojgan Roushan, and Dr. Xu Du. Many thanks go to Dr. Husnu Unalan from University of Cambridge, and Yun-Yue Lin from National Taiwan University for their patience and hard work during our collaborations. My sincere appreciation goes to Dr. Andre Mkhoyan from Cornell University whose expertise and knowledge in electron microscopy and spectroscopy contributed substantially to my dissertation project.

Finally, my deepest gratitude goes to my wife, Rie, and my family for their continuous support and encouragement.

TABLE OF CONTENTS

Abstract of the dissertation	ii
Acknowledgements	iii
Table of contents	iv
List of tables	viii
List of figures	ix
1 Introduction	1
1.1 Motivation	3
1.2 Chapter outline	3
2 Fundamental electronic structure of single-walled carbon nanotubes and graphene	5
2.1 Structure of graphene	6
2.2 Structure of single-walled carbon nanotubes	7
2.3 Energy dispersion relationship of graphene	9
2.4 Energy dispersion relationship of single-walled carbon nanotubes	10
2.5 Electronic density of states of graphene	12
2.6 Electronic density of states of single-walled carbon nanotubes	13
3 Fundamental electrical properties of single-walled carbon nanotubes and graphene ...	15
3.1 Single-walled carbon nanotubes	16
3.1.1 Metallic single-walled carbon nanotubes	16
3.1.2 Semiconducting single-walled carbon nanotubes	17
3.1.3 Single-walled carbon nanotube bundles and arrays	19
3.1.4 Single-walled carbon nanotube networks	20
3.1.5 Junctions of single-walled carbon nanotubes	22

3.4 Graphene.....	23
3.4.1 Mechanically exfoliated graphene	24
3.4.2 Graphene nanoribbons (GNRs).....	25
3.4.3 Chemically derived graphene.....	27
4 Post-deposition functionalization and metal contact effects on single-walled carbon nanotube thin films	29
4.1 Preparation and functionalization.....	30
4.2 Electrical and optical properties	31
4.3 Functional groups	33
4.4 Morphology and work function.....	35
4.5 Mechanical, thermal, and chemical stability	36
4.6 Effect of annealing and acid treatment on semiconducting thin films	39
4.7 Effect of contact metals on semiconducting thin films	41
4.8 Chapter summary.....	43
5 Bundling of single-walled carbon nanotubes in aqueous suspensions	45
5.1 Measurement apparatus	47
5.2 Experimental observation of suspension dynamics.....	48
5.3 Attenuation of light by individual nanotubes and bundles	50
5.4 Mie scattering for cylindrical particles	52
5.5 Simulation of cross-section enhancement	53
5.6 Calculation of bundle size	54
5.7 Electrical resistance of thin films	55
5.8 Thin film transistor characteristics and suspension dynamics.....	57
5.9 Chapter summary.....	59
6 Chemically derived graphene and its thin films: preparation, chemical and structural properties	60

6.1	Synthesis of graphene oxide	62
6.2	Vacuum filtration of graphene oxide suspensions.....	65
6.3	Reduction of graphene oxide	69
6.4	Chemical structure	69
6.5	Raman spectroscopy	73
6.5.1	Individual graphene sheets and thin films.....	73
6.5.2	Raman mapping.....	76
6.6	Scanning transmission electron microscopy study	78
6.6.1	Atomic structure	79
6.6.2	Electronic structure	81
6.7	Structure-dependent electrical conductivity	85
6.8	Chapter summary.....	87
7	Opto-electronic properties of chemically derived graphene thin films	89
7.1	Optical transmittance and electrical resistivity.....	90
7.2	Optical properties	95
7.3	Graphene-based electrode for photovoltaic devices.....	96
7.4	Temperature-dependent electrical properties	98
7.5	Ambipolar field effect	100
7.6	Effect of reduction.....	102
7.7	Effect of doping.....	104
7.8	Chapter summary.....	106
8	Graphene-based composite thin film transistors and field emitters.....	108
8.1	Semiconducting graphene-based composite thin films	109
8.1.1	Preparation	110
8.1.2	Ambipolar field effect.....	112
8.1.3	Temperature dependent transport.....	114

8.1.4 Effect of graphene sheet size.....	116
8.2 Field emission from graphene-based composite thin films	118
8.2.1 Graphene sheet orientation.....	119
8.2.2 Field emission properties	121
8.2.3 Fowler-Nordheim analysis	124
8.2.4 Field emission stability and emission site distribution.....	127
8.3 Chapter summary.....	128
9 Conclusions and suggested future works.....	129
9.1 SWNT network thin films	131
9.2 Chemically derived graphene thin films.....	132
 Bibliography	 134
Acknowledgement of previous publications.....	151
Curriculum Vita	152

LIST OF TABLES

Table 6.1	2D peak shift as a function of N used to obtain Raman map.....	77
Table 6.2	C K-edge peak positions of graphite, a-C, and GO films	83

LIST OF FIGURES

Fig 1.1 Structure of sp^2 carbon allotropes.....	2
Fig 2.1 Structure of graphene.....	7
Fig 2.2 Structure of SWNTs	8
Fig 2.3 Energy dispersion relationship of graphene	10
Fig 2.4 Energy dispersion relationship of SWNT.....	12
Fig 2.5 Electronic density of states of graphene.....	13
Fig 2.6 Electronic density of states of SWNT	14
Fig 3.1 Characteristics of SWNT FETs	18
Fig 3.2 Characteristics of SWNT bundle and array FETs	20
Fig 3.3 Characteristics of SWNT network TFTs.....	21
Fig 3.4 Electrical properties of crossed SWNT junctions.....	23
Fig 3.5 Characteristics of graphene FETs.....	25
Fig 3.6 Characteristics of GNR FETs	26
Fig 3.7 Characteristics of chemically derived graphene FETs	28
Fig 4.1 Sheet resistance and transmittance of functionalized SWNT thin films	33
Fig 4.2 FTIR and TGA spectra of functionalized SWNTs	35
Fig 4.3 AFM and KPFM images of functionalized SWNT thin films.....	36
Fig 4.4 Stability of functionalized SWNT thin films.....	37
Fig 4.5 Electrical properties of SWNT TFTs.....	40
Fig 4.6 Electrical properties of functionalized SWNT TFTs.....	41
Fig 4.7 Electrical properties of SWNT TFTs with different electrode metals.....	43

Fig 5.1 Schematic of absorbance measurement apparatus.....	48
Fig 5.2 Measured absorbance as a function of time.....	50
Fig 5.3 Schematic of the model used for the interpretation of absorbance.....	51
Fig 5.4 Calculated optical cross-section and bundle size	54
Fig 5.5 Sheet resistance of SWNT thin films versus settling time	56
Fig 5.6 SWNT TFT characteristics versus settling time.....	58
Fig 5.7 On/off ratio versus sheet resistance of SWNT TFT	59
Fig 6.1 Photographs of graphite and GO	64
Fig 6.2 Optical and AFM images of GO sheets.....	65
Fig 6.3 Photographs of GO thin films.....	67
Fig 6.4 Optical and AFM images of r-GO thin films	68
Fig 6.5 Morphology of r-GO thin films	68
Fig 6.6 FTIR spectra of GO before and after reduction.....	70
Fig 6.7 C1s and O1s XPS spectra of GO thin films.....	71
Fig 6.8 Raman spectra of individual GO sheets	74
Fig 6.9 Raman spectra of GO thin films	76
Fig 6.10 Raman maps of r-GO thin films	77
Fig 6.11 STEM-ADF image and SAED of the GO films	81
Fig 6.12 Core-loss and low-loss EELS spectra of a GO sheet.....	84
Fig 6.13 Conductivity of r-GO as a function of the sp^2 carbon fraction.....	86
Fig 6.14 Structural model of GO at different stages of reduction	87
Fig 7.1 Sheet resistance and transmittance of GO thin films.....	92
Fig 7.2 Conductivity and transmittance of GO thin film versus reduction parameters ...	94
Fig 7.3 Transmittance as a function of sheet resistance of r-GO thin films	95
Fig 7.4 Optical constants and absorbance of GO thin films	96

Fig 7.5 Characteristics of OPV with r-GO electrode	98
Fig 7.6 I - V characteristics r-GO thin films at different temperatures	100
Fig 7.7 Characteristics of r-GO TFTs at different temperatures.....	102
Fig 7.8 Characteristics of r-GO TFTs with different reduction conditions	104
Fig 7.9 Characteristics of r-GO TFTs with different doping conditions	106
Fig 8.1 AFM and SEM images of FGS-PS composite thin films	111
Fig 8.2 Characteristics of FGS-PS TFTs in different environment	113
Fig 8.3 Conductivity of FGS-PS TFT as a function of temperature.....	115
Fig 8.4 Field effect mobility FGS-PS TFT as a function of FGS flake size.....	117
Fig 8.5 AFM images of FGS-PS thin films with different deposition conditions	120
Fig 8.6 Lateral resistivity of FGS-PS thin films versus the spin-coating speeds.....	121
Fig 8.7 Field emission characteristics of FGS-PS thin films	123
Fig 8.8 Schematics showing graphene field emitters protruding from the PS matrix ...	125
Fig 8.9 Fowler-Nordheim plots of FGS-PS thin film field emission characteristics.....	127
Fig 8.10 Field emission current stability with time and emission site distribution	128

Chapter 1

Introduction

Carbon is the sixth element of the periodic table and is one of the most abundant elements in the earth's crust. It is found in all life forms, and is the backbone of all organic compounds. Ubiquity of carbon stems from its ability to form different types of chemical bonds. In physical terms, the electronic states of a carbon atom can assume several possible configurations. In carbon, hybridization occurs between $2s$ and $2p$ orbitals to form sp^n state, where n is the number of $2p$ orbitals mixed with the $2s$ orbital. The ability to exhibit

sp^n hybridization gives rise to the formation of a wide variety of molecular and crystalline structures with varied chemical and physical properties. The sp^2 hybridized carbon systems are particularly interesting because carbon molecules with every dimensionality (0 to 3) can be formed. In fact, carbon is the only element in the periodic table which has allotropes from zero to three dimensions¹ (**Fig 1.1**). While graphite, a three dimensional sp^2 carbon allotrope, has been known for centuries², discovery of the fullerene molecules (0-D) in 1985 (Ref. ³), carbon nanotubes (1-D) in 1991 (Ref. ⁴), and graphene (2-D) in 2004 (Ref. ⁵) has sparked tremendous research in the past two decades. These materials have unique and extraordinary optical, electrical, mechanical, and thermal properties arising from their dimensionality and structure¹. Single-walled carbon nanotubes (SWNTs) and graphene share a suite of unusual properties which may be useful for practical applications. For example, their extraordinary strength⁶⁻¹¹ makes them ideal for composites¹²⁻¹⁴, high current carrying capacity¹⁵⁻¹⁸, electrical conductivity^{16, 19} and carrier mobility^{19, 20} for interconnects and ultra-high frequency transistors of microelectronic^{21, 22} and spintronic²³⁻²⁵ circuitries, large thermal conductivity^{26, 27} for heat sinks, chemical stability^{28, 29} for coatings, large surface areas for sensors²⁹⁻³¹ and ultra-capacitors^{32, 33}, to name a few. SWNTs and graphene also provide ideal systems to study fundamental physics associated with low-dimensional charge^{16, 34} and phonon^{35, 36} dynamics. Particularly, discovery of graphene has opened up a pathway to studying relativistic quasiparticles in a benchtop device and has led to observations of peculiar phenomena predicted by quantum electrodynamics³⁷.

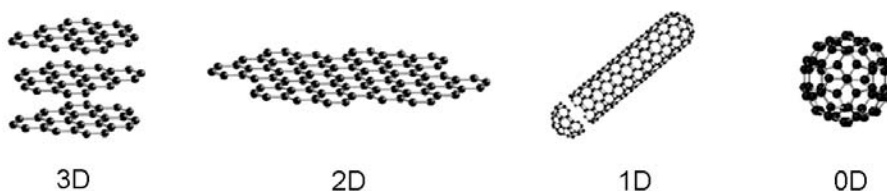


Fig 1.1 Structure of sp^2 carbon allotropes. From left to right, graphite (3D), graphene (2D), carbon nanotube (1D), and fullerene molecule (0D) are shown. Reproduced from Ref. 38.

1.1 Motivation

The predicted technological impacts of SWNTs and graphene are considerable, particularly in the field of nano-electronics as their intrinsically small size and exceptional electrical properties could extend the limit of Moore's law³⁹. However, while SWNTs and graphene could be viewed as the material for next generation of electronics, reports on making them technologically feasible for integration into devices have been lacking. This is attributed to the fact that reliable means of fabricating and manipulating these nano-structures in large quantities are not available. The challenges associated with fabrication and manipulation therefore pose a significant hurdle for translating the extraordinary fundamental properties of SWNTs and graphene into technological innovations and eventual implementation into applications. For example, despite the large amount of effort and resources spent over nearly two decades, carbon nanotubes are still not used in mainstream electronic applications due to two technological obstacles, namely large-area deposition and device integration.

The main goal of this work is to develop the solution-based methods for achieving large-area deposition of SWNTs and graphene in the form of thin film networks and explore their potential as electronic materials. The studies presented in this thesis tackle the deposition and integration-related challenges by depositing 2-dimensional networks of SWNTs and graphene, which can be viewed as new class of thin film electronic materials. Exploiting the novel properties of SWNTs and graphene for various applications related to large-area electronics is the primary aim of this thesis.

1.2 Chapter outline

In the following Chapter, the electronic structures of SWNTs and graphene are introduced. Chapter 3 is a brief overview of the fundamental electrical properties of SWNTs and graphene along with a review of some key experimental results from the

literature. In Chapters 4 through 8, original research results and discussion of solution-processed SWNT and graphene thin films are presented. Specifically, SWNT thin film properties and implications of doping and bundling dynamics are discussed in Chapters 4 and 5. In Chapters 6 through 8, studies on the development of chemically derived graphene-based thin films and their structural, opto-electronic, and field emission properties are presented. Concluding remarks and suggested future work are presented in Chapter 9.

Chapter 2

Fundamental electronic structure of single-walled carbon nanotubes and graphene

Since SWNTs and graphene share the same honeycomb crystal lattice, their electronic structures are closely related. In fact, a commonly used approach for the calculation of SWNT electronic structure involves calculation of the graphene energy dispersion⁴⁰. The main difference in the electronic structures between the two is that quantum confinement in SWNTs is in one dimension (1D) while in graphene the electrons are confined in two dimensions (2D). 1D confinement in graphene can be introduced by

reducing its size to form quasi-one-dimensional graphene nano-ribbons (GNRs)⁴¹. Electronically, graphene is a direct zero band gap semiconductor whereas SWNTs and GNRs can be either metallic or semiconducting depending on their structure^{40, 41}.

In this Chapter, basic concepts and methodology used to understand the electronic structure of SWNTs and graphene are introduced. Some relevant experimental results are also discussed briefly.

2.1 Structure of graphene

A graphene sheet consists of carbon atoms arranged in a honeycomb lattice. The honeycomb structure can be seen as two sets of hexagonal sublattices (**Fig 2.1a**). Unit cell of the lattice consists of two carbon atoms and is defined by lattice vectors $\mathbf{a}_1 = (\sqrt{3} a_{C-C}/2, a_{C-C}/2)$ and $\mathbf{a}_2 = (\sqrt{3} a_{C-C}/2, -a_{C-C}/2)$ where $a_{C-C} = 1.44 \text{ \AA}$ is the C–C bond length⁴². A carbon atom in graphene has three first-nearest neighbors at a distance of 1.44 \AA , six second-nearest neighbors at a distance of 2.49 \AA , and three third-nearest neighbors at a distance of 2.88 \AA (**Fig 2.1a**). Graphene is one atom layer thick with thickness of 3.4 \AA , which is the interlayer distance of graphite⁴³. The lateral size of graphene can be as large as hundreds of microns, which corresponds to few millions of carbon atoms across graphene sheet³⁷. Graphene with lateral dimensions reduced to few nanometers is referred to as graphene nano-ribbons (GNR)⁴⁴. The Brillouin zone of graphene is hexagonal in shape with high-symmetry point Γ , K and M as shown in **Fig 2.1b** (Ref. ⁴²). The lattice structure of graphene can be visualized by scanning tunneling microscope (STM)^{45, 46} (**Fig 2.1c**) and scanning transmission electron microscope (STEM)^{47, 48}. Graphene sheets are extremely compliant to the substrate surface morphology. The topographical corrugations⁴⁶ and charge inhomogeneity⁴⁹ arising from the substrates often obscure the ideal carrier transport properties (**Fig 2.1d**).

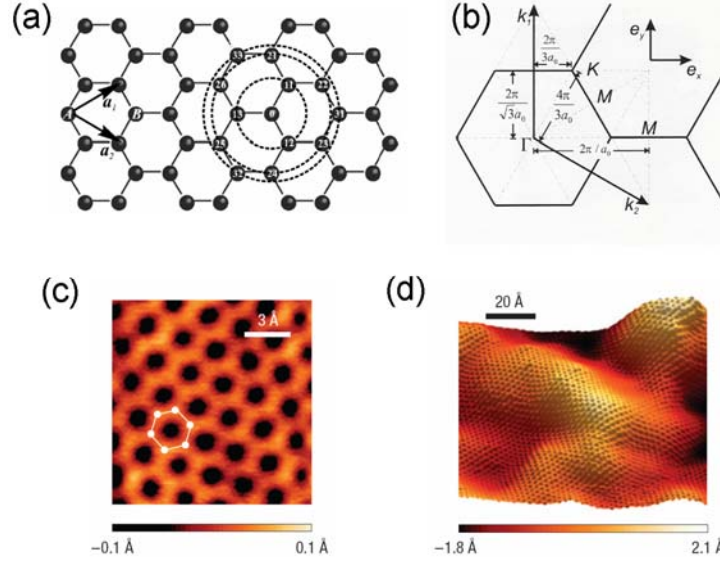


Fig 2.1 (a) Honeycomb structure of graphene showing two sublattice atoms denoted as A and B . a_1 and a_2 are the unit vectors (Reproduced from Ref. ⁴²). The circles indicate the first, second, and third-nearest neighbors of the atom labeled as 0. (b) Brillouin zone of graphene. Points of high symmetry are labeled as Γ , K , and M (Reproduced from Ref. ⁴²). (c) STM image of graphene lattice (Reproduced from Ref. ⁵⁰). (d) STM topographical image of graphene on SiO_2 showing surface corrugations (Reproduced from Ref. ⁵⁰).

2.2 Structure of single-walled carbon nanotubes

Single-walled carbon nanotubes (SWNTs) are hollow cylinders of graphene sheet. The SWNT can be thought of as being formed by rolling up a piece of a graphene ribbon into a seamless tube. This rolling-up can be done in an infinite number of ways depending on the size and orientation of the starting graphene ribbon resulting in infinitely many structures of SWNTs. The structure of a SWNT can be specified by a vector in the honeycomb lattice of the unrolled graphene sheet. This vector is called the chiral vector (C_h) and is expressed using the real space unit vectors a_1 and a_2 as shown in **Fig 2.2**. The two ends of C_h , $(0,0)$ and $(11,7)$, correspond to the crystallographically equivalent sites which coincide upon rolling of the sheet. The chiral vector C_h is generally expressed with a pair of integers (n, m) as shown in **Eq 2.1**.

$$\mathbf{C}_h = n\mathbf{a}_1 + m\mathbf{a}_2 \equiv (n, m), (n, m \text{ are integers}, 0 \leq |m| \leq n) \quad (2.1)$$

Chiral angles θ and ϕ are defined as the angle between the vectors \mathbf{C}_h and \mathbf{a}_1 and $30^\circ - \theta$, respectively. Because of the hexagonal symmetry of the honeycomb lattice, all SWNT types can be expressed with chiral vectors for which $0 \leq |\theta| \leq 30^\circ$, or equivalently $0 \leq |m| \leq n$. A SWNT is called armchair type when $|\theta| = 30^\circ$ or $\mathbf{C}_h \equiv (n, n)$, and zigzag type when $|\theta| = 0^\circ$ or $\mathbf{C}_h \equiv (n, 0)$. All other SWNTs, where $0 < |\theta| < 30^\circ$, are called chiral nanotubes. An example of zigzag, armchair, and chiral SWNTs are shown in **Fig 2.2b**. An atomically resolved STM image of (11,7) is also shown in **Fig 2.2c**. Translational vector \mathbf{T} is a unit vector perpendicular to \mathbf{C}_h , and can be expressed as

$$\mathbf{T} = t_1\mathbf{a}_1 + t_2\mathbf{a}_2 \quad (2.2)$$

where t_1 and t_2 are integers with

$$t_1 = \frac{2m+n}{d_R}, \quad t_2 = -\frac{2n+m}{d_R} \quad (2.3)$$

where d_R is the greatest common divisor of $(2m+n)$ and $(2n+m)$. The unit cell of a SWNT corresponds to the rectangle formed between \mathbf{C}_h and \mathbf{T} .

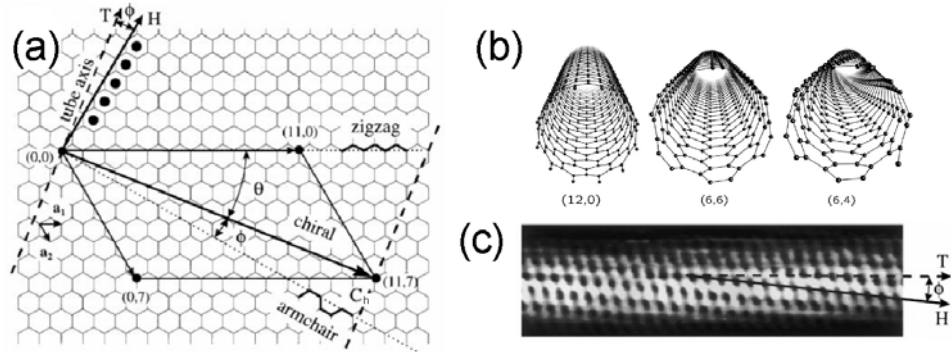


Fig 2.2 (a) Schematic of hexagonal graphene lattice showing unit vectors (\mathbf{a}_1 and \mathbf{a}_2) and an example of a chiral vector (\mathbf{C}_h), chiral angle (θ and ϕ), and translational vector (\mathbf{T}). Vector \mathbf{H} is perpendicular to armchair direction and specifies nearest neighbor hexagon rows marked by the black dots. (b) Structure of (12,0), (6,6) and (6,4) SWNTs (Reproduced from Ref. ⁵¹). (c) STM image of (11,7) SWNT showing \mathbf{T} and \mathbf{H} . (a) and (c) were reproduced from Ref. ⁵².

2.3 Energy dispersion relationship of graphene

Each carbon atom has three electrons in the sp^2 orbital and one electron in the p_z orbital (Here, z refers to the direction normal to the graphene plane). Electrons in the sp^2 orbitals form σ bonds while the electrons in the p_z orbitals form π bonds with neighboring carbon atoms. Electrons in the p_z orbitals, referred to as π electrons, are weakly bound to the nucleus and are delocalized over the graphene sheet. The energy levels of the σ bonds are far from the Fermi level and are generally not involved in the electronic transport and optical properties of an intrinsic graphene. On the other hand, the bonding and anti-bonding states of π electrons meet at the Fermi level and dominate the opto-electronic properties. The electronic structure of graphene is therefore often simply described by π valence and conduction bands. Using the tight-binding approximation, the energy dispersion of π electrons in graphene can be obtained⁴²:

$$E(k_x, k_y) = \pm \gamma_0 \left[1 + 4 \cos\left(\frac{\sqrt{3}k_x a_{C-C}}{2}\right) \cos\left(\frac{k_y a_{C-C}}{2}\right) + 4 \cos^2\left(\frac{k_y a_{C-C}}{2}\right) \right]^{1/2} \quad (2.4)$$

where γ_0 is the nearest neighbor hopping energy (on the order of 2.8 eV)⁴². This equation yields two bands for plus and minus signs, corresponding to bonding (π) and anti-bonding (π^*) states of the two atoms in the unit cell. The two bands can also be regarded as valence and conduction bands. The equation indicates that the two bands are symmetric, which is a consequence of the assumption that the next-nearest hopping energy is negligible. The energy dispersion of graphene calculated considering the next-nearest hopping energy γ_1 to be $0.2\gamma_0$ results in asymmetry of the two bands (**Fig 2.3a**)⁵³. The conduction and valence bands touch at the corners of the Brillouin zone, or K points. These points are also called Dirac points and an expanded view of the dispersion around a Dirac point for $|E| < \sim 1$ eV shows two cones, referred to as Dirac cones, touching at their vertices. The carrier dynamics in graphene can be expressed as a function of momentum relative to the Dirac points $\mathbf{q} = \mathbf{k} - \mathbf{K}$ where $|\mathbf{q}| \ll |\mathbf{K}|$:

$$E_{\pm}(\mathbf{q}) \approx \pm \hbar v_F |\mathbf{q}| \quad (2.5)$$

where v_F is the Fermi velocity expressed as $\sqrt{3}\gamma_0 a_{C-C} / 2\hbar \sim 10^6$ m/s. The Fermi velocity is independent on energy and momentum, which is in striking contrast to the behavior of most materials where velocity is a function of energy, *i.e.* $v = \hbar k / m = \sqrt{2E/m}$. **Eqn. 2.5** is equivalent to Hamiltonian for massless Dirac fermions. Charge carriers in graphene therefore have zero effective mass and behave as relativistic particles³⁴.

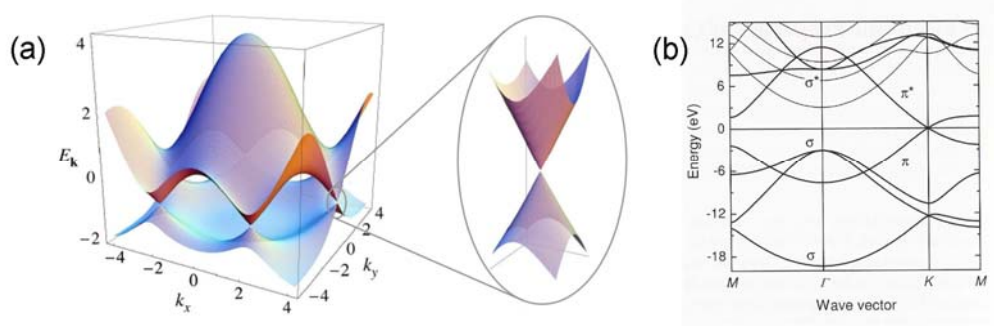


Fig 2.3 Energy dispersion relationship of graphene from (a) tight-binding model ($\gamma_0 = 2.7$ eV and $\gamma_1 = 0.2 \gamma_0$) and (b) ab-initio calculations. An expanded view around Dirac point is shown in (a). (a) was reproduced from Ref. ⁵³ and (b) from Ref. ⁴².

2.4 Energy dispersion relationship of single-walled carbon nanotubes

To a first approximation, the electronic structure of SWNTs can be derived from the dispersion relationship of graphene. In this Section, a commonly used method for deriving energy dispersion relationship of SWNTs from that of graphene, known as zone-folding, is described. The main difference between SWNTs and graphene is the quantum confinement arising from their dimensions. In the case of SWNTs, a periodic boundary condition imposed along the circumference, C_h , requires that the component of the momentum along the circumference, k_{\perp} , is quantized such that

$$C_h = \pi d = v\lambda = v \frac{2\pi}{k_{\perp}} \leftrightarrow k_{\perp} = \frac{2\pi}{C_h} v = \frac{2}{d} v \quad (2.6)$$

where ν is a non-zero integer. In other words, wave function of electrons must have a phase shift of an integer that is a multiple of 2π around the circumference of SWNTs.

On the other hand, the wavevector along the axis of the tube ($\mathbf{k}_{//}$) is continuous because the tube is regarded as infinitely long. The first Brillouin zone in this direction is

$$-\frac{\pi}{T} < \mathbf{k}_{//} \leq \frac{\pi}{T}. \quad (2.7)$$

where T is the translational period. Using orthogonality conditions among \mathbf{C}_h , \mathbf{T} , $\mathbf{k}_{//}$ and \mathbf{k}_{\perp} , expression for $\mathbf{k}_{//}$ and \mathbf{k}_{\perp} can be obtained:

$$\mathbf{k}_{//} = \frac{1}{N} (-t_2 \mathbf{k}_1 + t_1 \mathbf{k}_2) \quad (2.8)$$

$$\mathbf{k}_{\perp} = \frac{1}{N} (m \mathbf{k}_1 - n \mathbf{k}_2) \quad (2.9)$$

where N is the number of hexagons in the nanotube unit cell. The allowed wavevectors appear as a series of parallel lines in the k space of graphene as shown in **Fig 2.4**. The orientation, length, and the density of these lines depend on the chiral indices (n, m) of SWNTs. The band structure of a SWNT with (n, m) index can be found by taking the energy dispersion relationship of graphene along the allowed values of \mathbf{k} given by **Eqn 2.6**. The important result of this approach is that it allows identification of SWNTs with chiral index (n, m) are metallic or semiconducting. For example, if the allowed states of a SWNT touch at the graphene K point, then the SWNT is metallic. Otherwise, the SWNT is semiconducting with a band gap. Specifically, a SWNT is metallic if

$$\mathbf{K} \cdot \mathbf{C}_h = 2\pi p = \frac{1}{3} (\mathbf{k}_1 - \mathbf{k}_2) \cdot (n \mathbf{a}_1 + m \mathbf{a}_2) = \frac{2\pi}{3} (n - m), \quad (2.10)$$

that is

$$3p = n - m. \quad (2.11)$$

In other words, a SWNT is metallic if $n - m$ is a multiple of three.

Approximation of SWNT electronic structure by zone-folding does not take into account the geometry and curvature of the SWNT walls. The zone-folding approach generally gives reliable results for SWNTs with diameters between 0.5 and 1 nm and

correctly predicts the metallic and semiconducting character of the SWNTs. This technique is commonly used because many of the synthesized SWNTs possess diameters in this range.

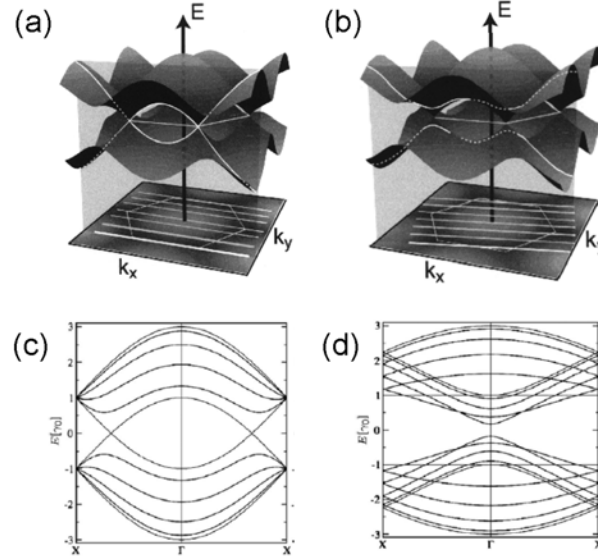


Fig 2.4 Allowed energy states of (a) metallic and (b) semiconducting SWNTs derived from the dispersion relationship of graphene (Reproduced from Ref. ⁵⁴). Energy bands along $K-\Gamma-K$ direction (here, X is equivalent to K) for (a) (5,5) metallic and (b) (10,0) semiconducting SWNTs (Reproduced from Ref. ⁵¹).

2.5 Electronic density of states of graphene

The electronic density of states (DOS) of graphene can be derived from **Eqn 2.4**. In the proximity of Dirac points, DOS ($\rho(E)$) can be derived from **Eqn 2.5**:

$$\rho(E) = \frac{2E}{\pi \hbar^2 v_F^2} \quad (2.12)$$

which shows that DOS of graphene is linearly dependent on E and vanishes at Fermi level as shown in **Fig 2.5a and b**, indicating that graphene is a zero band gap semiconductor. On the other hand, DOS of multilayered graphene is non-linear, similar to most bulk 3D materials. Further, the two bands overlap at the Fermi level, rendering multilayered

graphene a semi-metal. It should also be noted that the degree of band overlap is dependent on the number of graphene layers, approaching the graphite limit with increasing number of layers as shown in **Fig 2.5c**.

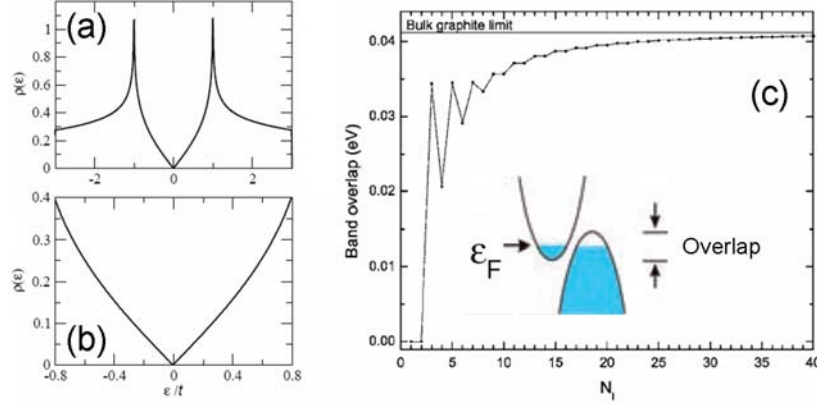


Fig 2.5 (a,b) Electronic DOS of graphene in units of γ_0 plotted in different scales (Reproduced from Ref. ⁵³). (c) Band overlap as a function of the number of graphene layers (Reproduced from Ref. ⁵⁵). Inset shows the schematic of overlapping bands (Reproduced from Ref ⁵).

2.6 Electronic density of states of single-walled carbon nanotubes

The electronic DOS of SWNTs is given by⁵⁶

$$\rho(E) = \frac{2}{l} \sum_i \int dk (k_{||} - k_i) \left| \frac{\partial E^\pm(k_\perp, k_{||})}{\partial k_{||}} \right|^{-1} \quad (2.13)$$

where l is the length of the Brillouin zone and k_i is given by $E - E(k_\perp, k_{||}) = 0$. **Fig 2.6** shows DOS for a (10, 0) zigzag semiconducting SWNT and a (9, 0) zigzag metallic SWNT. DOS of SWNTs consists of spikes referred to as van Hove singularities at energies where energy band has a minimum or a maximum. Metallic SWNTs have finite DOS at the Fermi level while DOS of semiconducting SWNTs has a gap (E_g) at the Fermi level. **Fig 2.6c** shows chiral indices that result in metallic and semiconducting SWNTs. The size of band gap depends on the nanotube diameter d according to

$$E_{gap} = \frac{2\gamma_0 a_{C-C}}{d} \quad (2.14)$$

Assuming $\gamma_0 = 2.7$ eV and $a_{c-c} = 1.44$ Å, **Eqn 2.14** can be rewritten as

$$E_{\text{gap}} = \frac{7.776}{d} \text{ eV} \quad (2.15)$$

for d in units of Å. The relation in **Eqn 2.14** has been experimentally confirmed using scanning tunneling spectroscopy (STS)^{52, 57} as shown in **Fig 2.6d**. Van Hove singularities and the diameter-dependent band gap are unique signatures of SWNTs, which can be observed by various spectroscopic techniques⁵⁸⁻⁶².

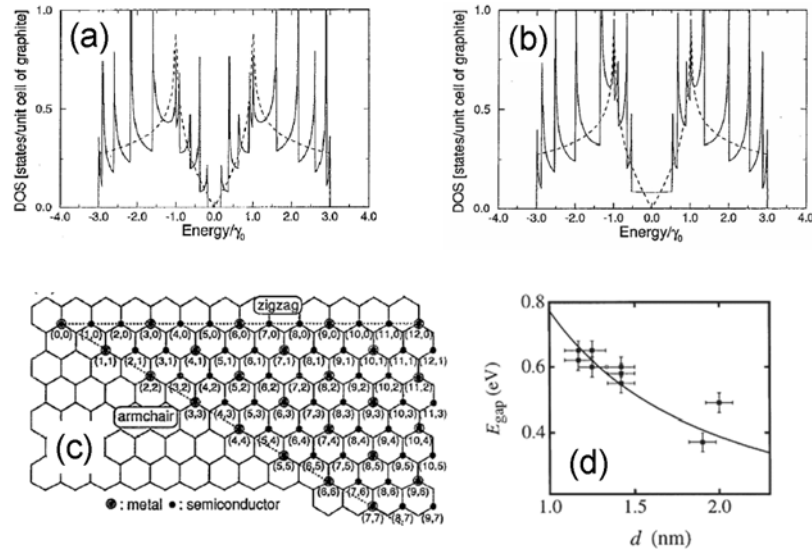


Fig 2.6 DOS of (a) (10,0) semiconducting and (b) (9,0) metallic SWNTs. (c) SWNT lattice showing indices for semiconducting (dot) and metallic (circled dot) SWNTs. (a-c) were reproduced from Ref. ⁴⁰. (d) Energy band gap vs diameter for semiconducting chiral SWNTs measured by STS (Adopted from Ref. ⁵²). The solid line is a fit based on Eqn 2.14.

Chapter 3

Fundamental electrical properties of single-walled carbon nanotubes and graphene

The continuous shrinking of electronic devices poses a significant challenge to the extension of Moore's law. To go beyond Moore's law, novel circuits based on molecules and nanomaterials have been proposed. Single-walled carbon nanotubes (SWNTs) have been viewed as ideal building blocks for nano-scale electronics because of their small size (diameter ~ 1 nm) and their tunable electrical properties. For example, metallic SWNTs are ideal interconnect materials because of their high conductivity, which rivals that of copper.

Semiconducting SWNTs are ideal channel materials for high speed transistors due to their high mobility. A vast amount of effort has been put into unveiling the fundamental properties of SWNTs and integration into devices. Recent discovery of graphene has accelerated interest in carbon-based nano-materials and their application towards nano-scale electronics. In this Chapter, some important results on the fundamental electrical properties of SWNTs and graphene are reviewed.

3.1 Single-walled carbon nanotubes

As discussed in Chapter 2, SWNTs may be metallic or semiconducting depending on their chirality. Current synthesis techniques result in production of nanotubes with evenly distributed chiralities within a certain diameter range. This means that the material is heterogeneous, containing one-third metallic and two-thirds semiconducting SWNTs. Electrical measurements on individual nanotubes and bundles are commonly performed using standard lithographic processes. In the following Sections, the electrical properties of individual SWNTs, their bundles, arrays and networks are described. Implications associated with SWNT junctions are also discussed.

3.1.1 Metallic single-walled carbon nanotubes

Electrical resistance in SWNTs arises from carrier scattering by impurities, defects, and lattice vibrations, similar to bulk materials. However, in the case of SWNTs, small angle scattering is not allowed and only forward and backward motion of carriers contributes to resistance⁶³. Thus the mean free path of carriers within SWNTs is unusually long and transport can be ballistic¹⁶. In the ballistic regime, electrical resistance within the nanotube is negligible whereas in the diffusive regime, *i.e.* for micrometric SWNTs, finite electrical resistance on the order of $10\ \Omega$ is observed⁶⁴. There is another type of resistance associated with the interface between 1-D conductor and 3-D electrode. This is called quantum resistance and is a result of mismatch between the quantized energy states in 1-D

conductor such as SWNTs and continuous energy states in metals. An ideal metallic nanotube with perfect contacts to a metal has a resistance of $R_Q = h/4e^2 = 6.45 \text{ k}\Omega$. Using highly transparent contacts between the nanotube and the electrode, resistance close to this theoretical limit has been observed experimentally⁶⁵.

3.1.2 Semiconducting single-walled carbon nanotubes

Semiconducting SWNTs with diameters between 1~1.5 nm have a band gap 0.5 ~ 1 eV and can be used as the channel material for transistors. FETs using individual semiconducting SWNTs were first demonstrated in 1998 (Ref. ^{64,66}). The typical device configuration is shown in **Fig 3.1a**. Unlike metallic SWNTs, conductance of semiconducting SWNTs can be modulated over 5 – 6 orders of magnitude with gate bias (**Fig 3.1b - d**). Semiconducting SWNTs are typically p-type and turn on with negative gate bias (**Fig 3.1b and c**). After first demonstrations of SWNT FETs, it was soon understood that the interface between SWNT and the electrode play a crucial role in the field modulated transport. Unlike silicon-based FETs in which the bulk conductance is modulated with gate bias, the principle of SWNT FETs in many cases, is based on modulation of contact resistance arising from the formation of a Schottky barrier at the SWNT-metal interface^{67,68}. Because the work function of electrode metals and SWNTs are often different, charge transfer occurs at the interface upon contact. The resulting interface dipole gives rise to a Schottky barrier. Carrier injection into the nanotube is determined by the Schottky barrier width, which can be modulated with gate bias as depicted in **Fig 3.2e and f**. When the gate electrode is negatively biased, energy band of the SWNT bends upwards causing the Schottky barrier to thin and allowing holes to be injected into the SWNT. The carrier injection is suppressed for positive gate bias. These devices are called Schottky barrier transistors.

SWNT FETs can also be operated in MOSFET-like bulk-switched modes. This requires high work function metal such as Pd to form Ohmic contacts¹⁶, a dual gate system

to isolate the effect of the Schottky barrier⁶⁹, or a chemical doping effect to alter the work function of SWNTs^{70, 71}. It has also been shown that when the contact barrier is avoided, SWNT-FETs can be operated in the ballistic regime¹⁶. Ohmically contacted SWNT FETs in non-ballistic regime have been reported to exhibit mobility value as high as 100,000 cm^2/Vs (Ref. ²⁰).

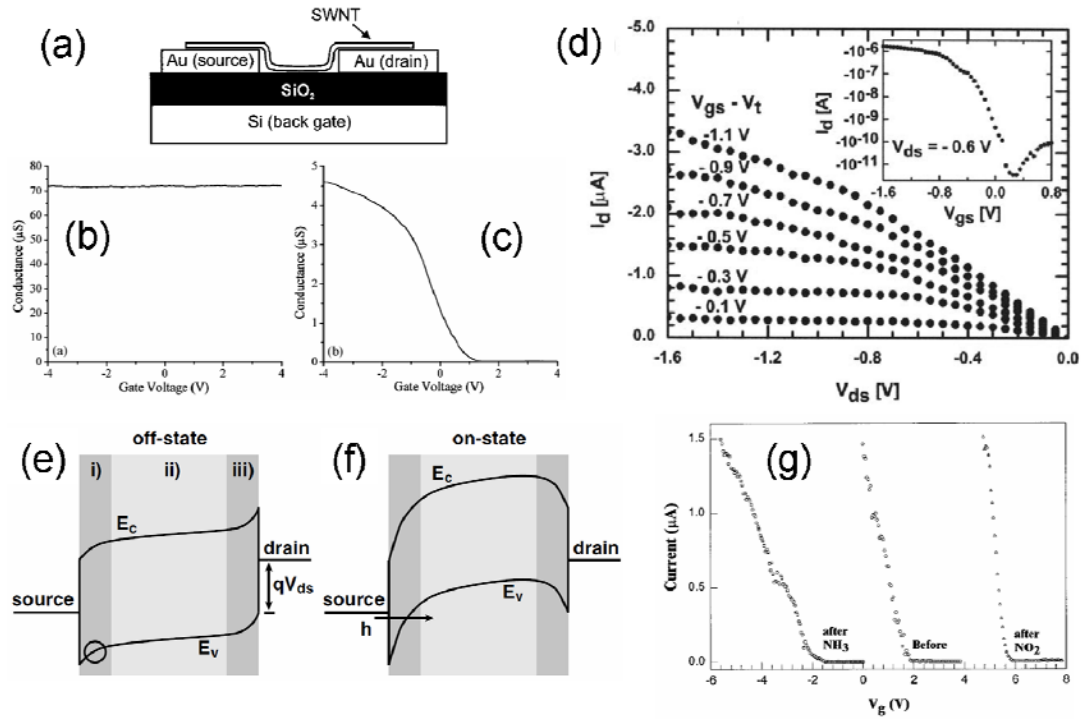


Fig 3.1 (a) Schematic of bottom-gated SWNT FET (Reproduced from Ref. ⁶⁴). (b,c) Transfer characteristics of (b) metallic and (c) semiconducting SWNTs (Reproduced from Ref. ⁷²). (d) I - V characteristics of a SWNT FET at different gate bias (Reproduced from Ref. ⁵⁴). The inset shows the transfer characteristics in log-scale. (e,f) Band diagram of SWNT FETs in the (e) off-state and (f) on-state (Reproduced from Ref. ⁶⁷). (g) Transfer characteristics of SWNT FET before and after exposure to NH₃ and NO₂ gases (Reproduced from Ref. ⁷³).

As in the case of typical semiconductors, doping in SWNTs alters local density of states (DOS) and results in shift of Fermi level. Semiconducting SWNTs are very sensitive

to gaseous molecules^{31, 73} and are unintentionally doped with oxygen and water in ambient conditions. Collins *et al.*³⁰ probed changes in the DOS of a semiconducting SWNT before and after exposure to oxygen using scanning tunneling spectroscopy (STS). The results showed that oxygen doping gives rise to apparent DOS near the valence band. Oxygen doping of SWNTs gives rise to an increase in conductivity. Doping of semiconducting SWNTs can also be monitored by the shift in the threshold voltage in transistor configuration. **Fig 3.1g** shows a negative and positive shift of the threshold voltage after exposing a SWNT-FET to NH_3 and NO_2 gases, respectively⁷³.

3.1.3 Single-walled carbon nanotube bundles and arrays

A major obstacle to effective manipulation of SWNTs is their tendency to adhere to each other or bundle together due to van der Waals interaction¹⁷. Bundling is commonly observed in liquid suspensions where the SWNTs are highly mobile⁷⁴. If a bundle consists of several nanotubes, then there is a high probability that it contains at least one metallic SWNT. The electrical properties of such a bundle are dominated by metallic SWNTs due to their high conductivity which obscures the presence of semiconducting tubes. A bundle containing even one metallic SWNT is therefore not suitable for FETs (**Fig 3.2a and c**). An analogous case to a bundle is an array of SWNTs (**Fig 3.2b**). In either case, FETs cannot be turned off due to significant leakage current carried by metallic SWNTs as shown in **Fig 3.2c and d**. One way of eliminating the contribution of metallic SWNTs in a bundle or array FETs is to apply large current across the device while maintaining the semiconducting SWNTs in the off-state with an appropriate gate bias¹⁷. This causes a large current to be carried only by the metallic SWNTs which eventually leads to their destruction by Joule heating or oxidation. Changes in device characteristics after elimination of metallic SWNTs from bundle and array FETs are also shown in **Fig 3.2c and d**. This technique is commonly used to obtain high performance SWNT FETs^{75, 76}.

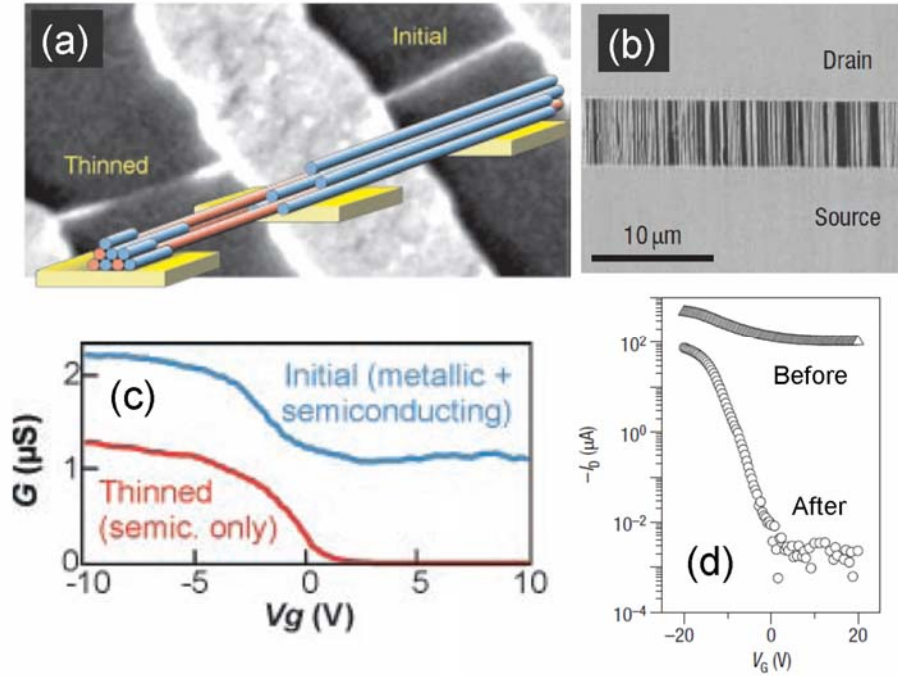


Fig 3.2 Scanning electron micrographs of (a) SWNT bundle and (b) SWNT array FETs. Transfer characteristics of devices before and after elimination of metallic SWNTs for the (c) SWNT bundle FET and (d) SWNT array FETs. (a,c) were reproduced from Ref. ¹⁷ and (b,d) from Ref. ⁷⁷.

3.1.4 Single-walled carbon nanotube networks

As-synthesized SWNTs are often in a form of random networks⁷⁸, as shown in **Fig 3.3a**. Snow *et al.*⁷⁹ proposed to treat such a network of SWNTs as a thin film electronic material. Unlike the devices consisting of individual SWNTs bridging the electrodes, the transport of charges across a network of SWNTs occurs over a number of nanotubes and their junctions. The electrical properties of SWNT networks are mainly determined by the interconnectivity or density of the network. The scaling of SWNT network conductivity with nanotube density can be described reasonably well with a percolation model^{80, 81}. One interesting feature of SWNT networks is that they can behave as either semiconducting or metallic material depending on the network density⁸¹. That is, when the density of SWNTs is above the metallic percolation threshold, it is metallic due to the presence of highly conducting pathways. On the other hand, a SWNT network is semiconducting below the

metallic percolation threshold and can be used as a channel material for TFTs. While the ability to tune the electronic properties is an attractive feature of SWNT networks, the threshold for metallic percolation is not clearly defined and mixed characteristics are often observed⁸². **Fig 3.3b** shows transfer characteristics of SWNT networks with different nanotube densities. A large on/off ratio ($> 10^4$) is achieved for a network with the low nanotube density (1 tube/ μm^2) while significant leakage current is observed for those with higher nanotube densities (> 3 tubes/ μm^2). Low leakage current can also be achieved by increasing the channel length in order to reduce the probability of percolation between metallic SWNTs percolation. **Fig 3.3c and d** show on/off ratio and mobility of SWNT TFTs as a function of nanotube density and channel length. It can be seen that mobilities of up to $50 \text{ cm}^2/\text{Vs}$ and on/off ratios $> 10^4$ can be achieved in random SWNT networks. In **Fig 3.3d**, the influence of channel length is highlighted. The results show that the on/off ratio can be improved with channel length by limiting the percolation of metallic SWNTs.

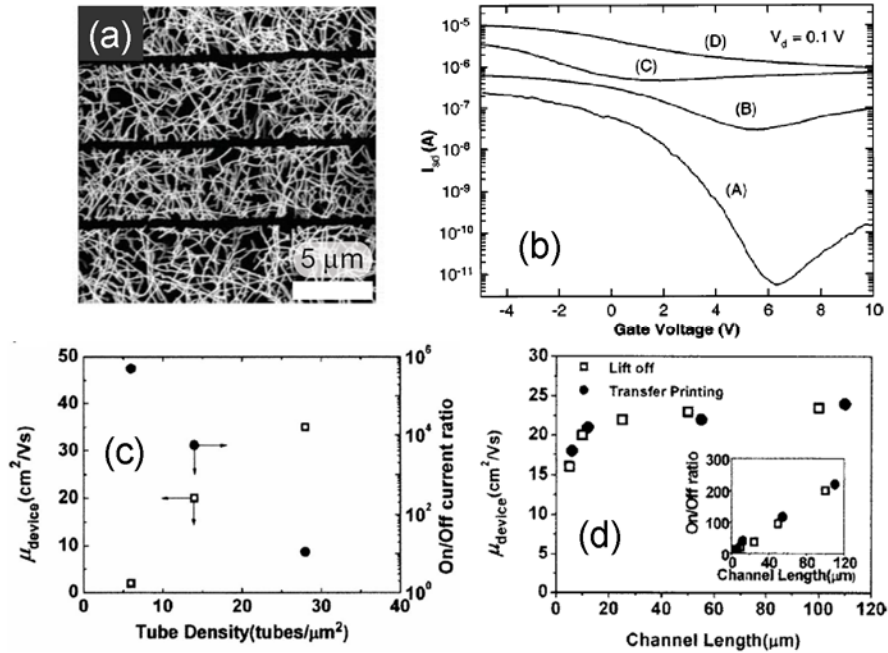


Fig 3.3 (a) CVD grown network of SWNTs (Reproduced from Ref. ⁸³). (b) Transfer characteristics of SWNT network TFTs with different nanotube densities: (A) 1 tube/ μm^2 and (B-D) > 3

tubes/ μm^2 (Reproduced from Ref. ⁷⁹). (c,d) A dependence of field effect mobility and on/off ratio of SWNT network TFTs as a function of (a) nanotube density and (b) channel length (Reproduced from Ref. ⁸²).

3.1.5 Junctions of single-walled carbon nanotubes

Randomly oriented networks of SWNTs consist of a large number of nanotube junctions. In order to drive current across the network, charge carriers traveling along a nanotube must tunnel into another nanotube. The total resistance of SWNT networks therefore arises from junction resistance as well as intrinsic resistance of individual SWNTs. Fuhrer *et al.*⁸⁴ investigated the transport properties of individual SWNT cross junctions (**Fig 3.4a**) and demonstrated that the tunneling transmission coefficients depend on the SWNT species that form the junctions. Specifically, transmission coefficients at the junction formed by two metallic SWNTs (MM), two semiconducting SWNTs (SS), and a metallic and a semiconducting SWNTs (MS) were found to be on the order of 0.1, 0.06, and 0.0002 respectively⁸⁴. That is, the resistance of MS junctions is 2 ~ 3 orders of magnitude higher than that of MM or SS junctions due to the presence of Schottky barrier (**Fig 3.4b-e**). The carriers therefore encounter a tunneling barrier due to a depletion region in addition to the tunneling barriers that are encountered at MM and SS junctions (**Fig 3.4c-e**). The carrier transport along the semiconducting SWNT at the MS junction is even more difficult than tunneling into the metallic SWNT because the tunnel barrier is twice the width of Schottky barrier encountered for MS tube-to-tube tunneling.

The implications associated with nanotube junctions have been investigated in SWNT network devices using atomic force microscope (AFM)-based techniques⁸⁵⁻⁸⁷. The results indicate that the large resistance of MS nanotube junctions severely impedes carrier transport for low density networks below the metallic SWNT percolation threshold⁸⁷. The electric force microscope image in **Fig 3.4 f** shows that the potential across a biased network is non-uniform and sudden voltage drop is observed at nanotube junctions⁸⁷.

Kodama *et al.*⁸⁶ indicated that the junction resistance may be modulated by gate bias in a FET configuration. The conducting AFM images shown in **Fig 3.4g and h** indicate that depending on the gate bias conditions, the conduction paths in the network are restricted due to modulation of junction resistance and semiconducting SWNT carrier concentration.

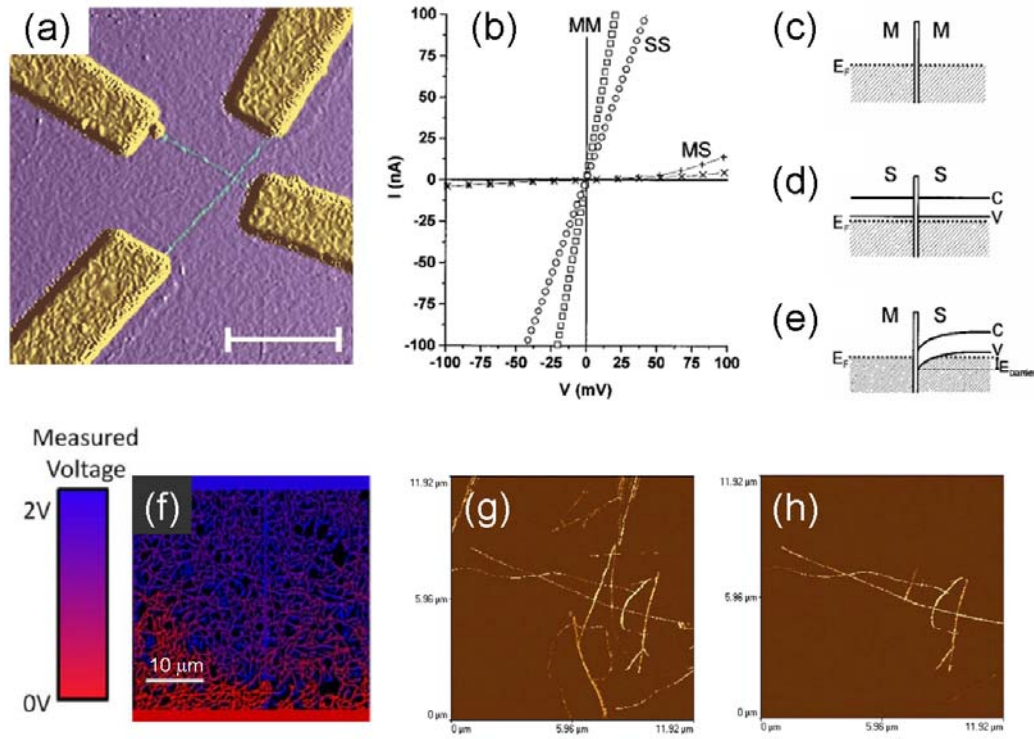


Fig 3.4 (a) AFM image of a crossed nanotube junction. (b) I - V characteristics of MM, SS, and MS junctions. (c-e) Qualitative band diagrams near (c) MM, (d) SS, and (e) MS junctions. (a-e) were reproduced from Ref. ⁸⁴. (f) Electric force microscope image of a biased SWNT network showing non-uniform potential across the channel (Reproduced from Ref. ⁸⁷). (g,h) Conductance AFM images showing a SWNT network in the (g) on-state ($V_g = 0$ V) and (f) off-state ($V_g = 10$ V) (Reproduced from Ref. ⁸⁵).

3.4 Graphene

The electrical properties of graphene are highly sensitive to the quality of the material as well as the conditions in which the measurements are made. The quality of graphene

depends largely on production methods. Graphene sheets obtained by mechanical exfoliation by scotch tape possess minimal defects and exhibit nearly-intrinsic properties³⁷. On the other hand, chemically derived graphene⁸⁸ exhibits properties which are significantly different from those of mechanically exfoliated graphene. The electronic structure of graphene can be engineered by reducing the lateral size of the sheet to make nano-ribbons. In the following Sections, fundamental electrical properties of mechanically exfoliated graphene, GNRs, and chemically derived graphene are reviewed.

3.4.1 Mechanically exfoliated graphene

When graphene is used as the channel material for FET, it can be electrostatically doped with gate bias (**Fig 3.5a and b**). The 2D resistivity (which is equivalent to the sheet resistance) of graphene typically varies by approximately one order of magnitude with gate bias and maximum resistivity is found for $V_g \sim 0$ V. The maximum resistivity occurs when Fermi level coincides with Dirac neutrality point where conduction and valence bands meet. In the absence of doping, the maximum resistivity is found at $V_g = 0$ V. The maximum resistivity at the Dirac point is often observed to be on the order of $h/2e^2 \sim 6.45$ k Ω , where h is the Planck's constant and e is the electronic charge (Ref. ^{5, 34, 89, 90}). Since resistivity greater than $h/2e^2$ is theoretically not achievable for ideal graphene, insulating state or off-state in a graphene FET cannot be reached. The conductivity (inverse of resistivity) of graphene is observed to depend linearly on carrier density (n) or V_g as shown in **Fig 3.5c**. This linear relationship arises from the fact that transport in graphene is limited by charged impurity scattering⁹¹⁻⁹³. Charged impurities arise from the substrates⁴⁹ as well as adsorbed species and limits carrier mobility in graphene⁹⁴. Another extrinsic effect limiting the mobility is the surface phonons at the SiO₂/Si substrate⁹⁵. Values approaching the intrinsic mobility limit of 200,000 cm²/V·s (Ref. ^{96, 97}) at low temperatures were achieved by suspending graphene and reducing charged impurity effects^{19, 98}. Graphene

FETs fabricated on SiO₂/Si substrates typically exhibit mobility values around 20,000 cm²/V·s (Ref. ⁹¹⁻⁹⁴).

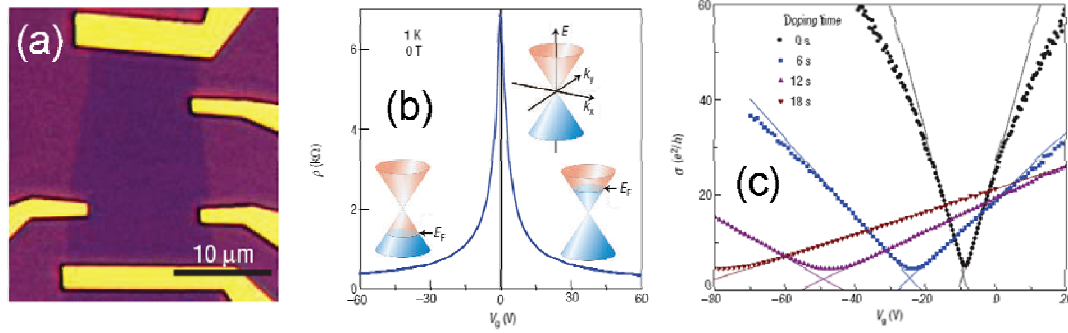


Fig 3.5 (a) Optical micrograph of typical graphene FET fabricated on SiO₂/Si substrate (Reproduced from Ref. ⁹⁴). (b) 2D resistivity as a function of gate voltage for graphene at 1 K. The inset shows the changes in Fermi level at different doping conditions (Reproduced from Ref. ³⁷). (c) Transfer characteristics of a graphene FET at different doping levels. Doping is achieved by depositing potassium atoms (Reproduced from Ref. ⁹⁴).

3.4.2 Graphene nanoribbons (GNRs)

In order for graphene to be used for digital applications, it is crucial that FETs can be “turned off” or become insulating with gate bias. This requires an energy band gap to be introduced in graphene electronic structure. One of the approaches to opening a gap is to reduce the lateral size of graphene to nanometer scale to induce confinement effects. Graphene nano-ribbons (GNRs) have been produced from a single sheet of graphene by electron beam lithography^{44, 99} and scanning tunneling microscope lithography¹⁰⁰. GNRs have also been derived chemically from bulk graphite¹⁰¹. Both lithographically patterned and chemically derived GNRs have been shown to exhibit narrow-band gap semiconductor properties as indicated in **Fig 3.6**. The on/off ratio of GNR FETs increases exponentially with decreasing width (W) in accordance with the theoretical prediction that the band gap of GNRs also varies inversely with W (Ref. ^{102, 103}). Unlike graphene, the on/off ratios of

GNR FETs increase with decreasing temperature due to the presence of the band gap. Smallest GNR that can be patterned by current lithographic technology has a width of ~ 20 nm and a band gap on the order of 30 meV. The effect of this band gap on the FET performance is negligible at room temperature and large on/off ratio ($\sim 10^3$) is only achieved at low temperatures (< 100 K) (**Fig 3.6a**). On the other hand, chemical synthesis results in GNRs with W as small as ~ 5 nm and band gap as large as 0.4 eV. FETs fabricated with these GNRs exhibit on/off ratios on the order of $\sim 10^7$ at room temperature (Ref. ¹⁰¹). It should be noted that the field effect mobilities of GNR FETs are 2 \sim 3 orders of magnitude lower than those of graphene FETs due to edge scattering effects¹⁰⁴.

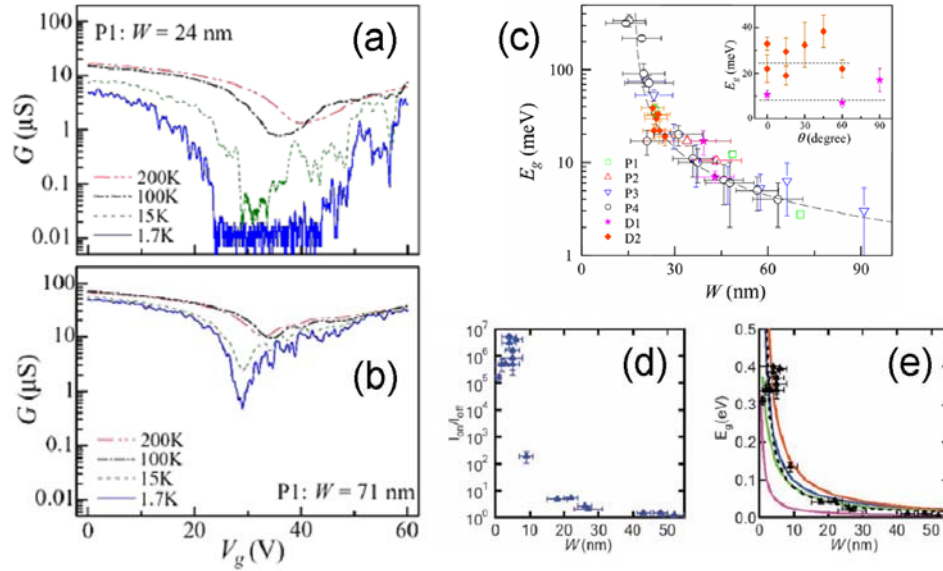


Fig 3.6 (a,b) Transfer characteristics of lithographically patterned GNR FET with (a) $W = 24$ nm and (b) $W = 71$ nm measured at different temperatures (Reproduced from Ref⁹⁹). (c) Energy band gap of lithographically patterned GNR as a function of width. The inset shows energy band gap as a function of edge orientation. The (d) on/off ratio and (e) energy band gap of chemically derived GNRs as a function of width.

3.4.3 Chemically derived graphene

Stankovich *et al.*¹⁰⁵ recently proposed a chemical route for producing large quantity of graphene from graphite. The process involves synthesis of graphite oxide and exfoliation into individual monolayer of graphene oxide (GO). GO can be viewed as graphene sheet with oxygen functional groups attached on the basal plane as well as around the sheet the edges. As-synthesized GO is electrically insulating because oxygen bonding disrupts sp^2 carbon network over which π electrons are delocalized. Reduction of GO partially restores the sp^2 carbon network and renders GO electrically conductive¹⁴. Reduction can be achieved via various routes but thermal annealing and chemical reduction are commonly used. GO sheets can be deposited onto a substrate from aqueous suspensions and lithographically contacted for transport studies as shown in **Fig 3.7a**. **Fig 3.7b and c** show transition of GO from insulator to conductor with gradual reduction treatment. Complete reduction of GO is generally not achieved and the conductivity of reduced GO is typically more than two orders of magnitude lower than the minimum conductivity of graphene due to residual oxygen and disorder^{106, 107}. FETs fabricated using reduced GO exhibit graphene-like ambipolar characteristics but the field effect mobility values is on the order of 1 - 300 $\text{cm}^2/\text{V}\cdot\text{s}$, which is significantly lower than those of ideal graphene^{106, 107} (**Fig 3.7d and e**). The on/off ratio increases with decreasing temperature as in the case of GNRs and values as large as 100 has been observed at low temperatures¹⁰⁷. The proposed conduction mechanism of reduced GO has been inconsistent due possibly to variability in the oxidation and reduction state of the reported reduced GO devices¹⁰⁶⁻¹¹¹. From temperature and field dependence of reduced GO conductivity, activated transport^{109, 110}, thermionic emission^{106, 108}, variable range hopping¹⁰⁷, and space-charge limited transport¹¹¹ have been proposed as potential conduction mechanisms. Wu *et al.*¹⁰⁸ indicated that as-synthesized GO is a semiconductor and forms a Schottky barrier at a metal interface. Jung *et al.*¹¹¹ reported that conduction in reduced GO FETs are not contact limited but trap limited. Chua *et al.*¹¹⁰ suggested that the transport mechanism may depend

on the structure of sp^2 carbon network. It is likely that carrier transport across highly disordered graphene occurs via hopping between intact sp^2 carbon domains. A recent study of hydrogenated graphene, or graphane¹¹², demonstrates that variable range hopping (**Fig 3.7f**) becomes the dominant transport mechanism after some of the atoms in the graphene lattice are converted to sp^3 carbon. Further investigation is essential to understand the correlation between the chemical and electronic structure of GO and transport properties.

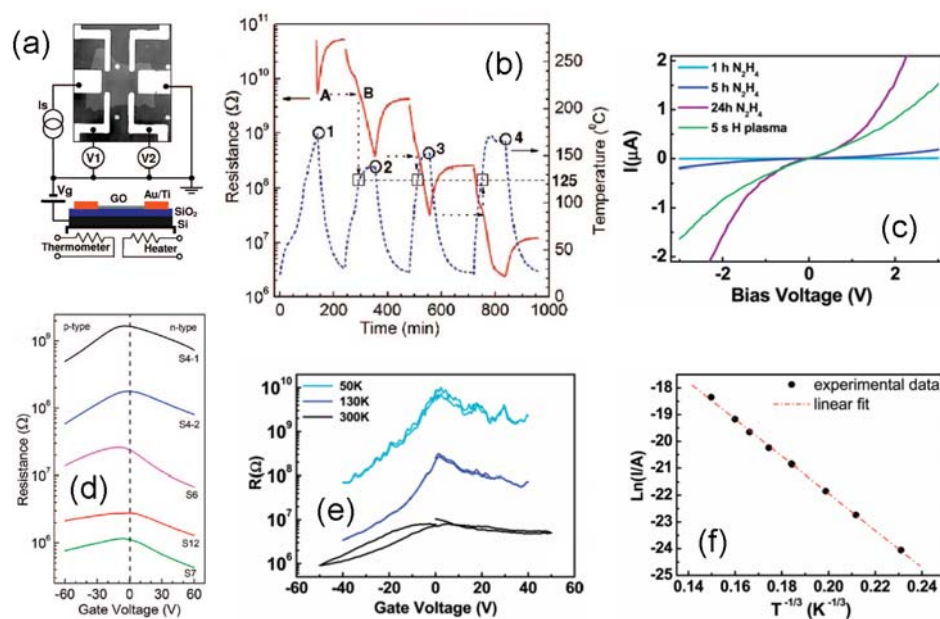


Fig 3.7 (a) Optical micrograph and device schematic of a reduced GO FET. The heater is used to thermally reduce GO. (b) Resistance of GO as a function of time during several annealing cycles. (c) I - V characteristics of GO with progressive chemical reduction. The results for H plasma reduction are also shown. (d) Transfer characteristics for progressively reduced GO. (e) Transfer characteristics of chemically reduced GO at different temperatures. (f) Current of chemically reduced GO fitted with variable range hopping model. (a,b,d) were reproduced from Ref. ¹¹¹ and (c,e,f) from Ref. ¹⁰⁷.

Chapter 4

Post-deposition functionalization and metal contact effects on single-walled carbon nanotube thin films

Transparent and conducting single-wall carbon nanotube (SWNTs) thin films are an interesting class of materials formed by low density networks of the nanotubes⁸⁰. They can be prepared by purifying the SWNTs then transferring them, at room or moderate temperature, onto wide ranging substrates, using a variety of techniques¹¹³⁻¹¹⁵. Their transport properties can be understood in the framework of the percolation theory^{80, 81} and, therefore, can be tuned over several orders of magnitude by adjusting the density of

SWNTs in the network by adjusting preparation conditions.

Typically, transparency of about 80% can be obtained at sheet resistances of ~ 0.5 k Ω /sq^{80, 81}, suggesting that they could be promising candidates for replacing indium-tin oxide (ITO) in organic electronics¹¹⁶⁻¹¹⁸. Although the sheet resistance of SWNT thin films is still higher than that of a 100 nm-thick ITO layer ($10 \sim 30$ Ω /sq)^{119, 120}, the unique morphological features make them efficient hole collectors in organic photovoltaics (OPVs), allowing conversion efficiencies of up to 2.5 % (Ref. ¹¹⁷). A decrease in the resistivity of SWNT films would be beneficial for OPVs, allowing possibility of achieving the state-of-the-art efficiencies of up to 5 % (Ref. ¹²¹).

We have recently reported that SWNTs covalently functionalized in phosphorus tribromide (PBr₃) can be used to prepare thin films with improved transport properties¹²². However, the PBr₃ treatment must be performed in a controlled atmosphere and, being incompatible with many types of substrates, it cannot be used for post-deposition treatment of the films. Covalent functionalization of carbon nanotubes in chlorides has also been reported to significantly decrease their sheet resistance¹²³. However, in order to use functionalized SWNT thin films in organic solar cells, it is important to study their stability upon thermal annealing and compatibility with the most commonly used solvents in solution processed organic photovoltaics.

In this Chapter, we report functionalization of SWNT thin films by exposure to acid and thionyl chloride (SOCl₂). Further we report the effects of acid doping on the properties of SWNT thin film transistors (TFT). The role of metal contacts on the device operation is also described.

4.1 Preparation and functionalization

The SWNT thin films were prepared using vacuum filtration method of Wu *et al.*¹¹³ from HiPCO SWNTs purified in our laboratory^{81, 116, 122, 124, 125}, arc-discharge synthesized SWNTs purified by the supplier (P2 type, Carbon Solutions Inc.¹²⁶) and laser-grown

SWNTs (CNI, purified using the method of Landi *et al.*¹²⁷). Aqueous solutions at 1 wt % of SDS were used to disperse the SWNTs at a concentration of 2 mg/L. Filtration (through 200 nm Millipore ester membranes) volumes ranging from 10 - 80 mL allowed the deposition of SWNT films of different thicknesses and densities¹²⁴. For TFT devices, low density SWNT thin films were prepared by filtering 60 mL of 0.05 mg/mL solutions⁸¹. The ester filter membranes were then transferred onto glass or PET substrates, dried in vacuum for 6 hrs under 250 g/cm² load and etched in consecutive acetone and methanol baths, leaving behind SWNT thin films on the substrates.

The functionalization treatment was carried out by dipping the films for 3 hrs in an azeotropic nitric acid bath (69.7% in HNO₃) and dried with gentle nitrogen flow. Subsequently, the nitric acid treated films were dipped for an additional 3 hrs in a SOCl₂ bath (97% reagent grade, Aldrich Inc.) and again carefully dried. All the treatments were performed in air at room temperature. The transmittance of the films was recorded at normal incidence using a Perkin Elmer Lambda 20 spectrophotometer. The electrical data were obtained from two-point measurements using $\pm 1V$ I - V scans at 100 mV/s. The same films were investigated both before and after functionalization using the same contact distance. Thus, the observed decreases in resistance imply a decrease in sheet resistance and an improvement in conductivity of the same magnitude. For TFT devices, metal electrodes were thermally evaporated onto SiO₂/p-Si substrates prior to thin film deposition unless otherwise noted. Si was used as the gate electrode and SiO₂ (thickness = 300 nm) was used as the gate dielectric.

4.2 Electrical and optical properties

The typical decrease in resistance by SOCl₂ functionalization at a constant transmittance in one of our films is shown in **Fig 4.1a**. It can be seen that the sheet resistance (R_s) decreases after the initial exposure to the 3 hr HNO₃ bath and further decreases after contact with SOCl₂. It can also be observed that the effect of the SOCl₂

treatment is almost instantaneous. Immersion of the film and complete drying leads to instant improvement in the conductivity by a factor of 5. Longer immersion times did not provide any further change in conductivity. In contrast, the transmittance of the thin films was not affected by the SOCl_2 functionalization process (see published paper¹²⁸ for details) which shows that the transmission coefficient of an undoped SWNT thin film overlaps with that of the same film after HNO_3 and SOCl_2 treatments, especially in the visible photon energy range.

We further investigated the role of the preliminary treatment in HNO_3 and the SOCl_2 treatment time. Although not essential in influencing the final sheet resistance or transparency of the SWNT thin films, we found that both of these steps are helpful in improving the stability of the functionalized SWNT thin films. In fact, using our protocol of HNO_3 and long SOCl_2 treatment times, the electrical characteristics of the SWNT thin films remained unchanged in air for several weeks (see **Fig 4.1a**). In contrast, the absence of the HNO_3 treatment and shorter SOCl_2 dipping times led to rapid degradation of the properties under thermal annealing and exposure to air or various solvents relevant for organic electronics.

The transmittance at 550 nm of SOCl_2 treated and the same untreated SWNT thin films as a function of their sheet resistance (R_s) is plotted in **Fig 4.1b**. It can be observed that while our untreated SWNT films exhibit properties comparable to those reported in the literature⁸⁰, the SOCl_2 functionalized films always exhibit lower sheet resistance at all transparency values. In the densest films, sheet resistance as low as 30–40 Ω/sq can be achieved, comparing favorably with ITO, albeit at lower transparency.

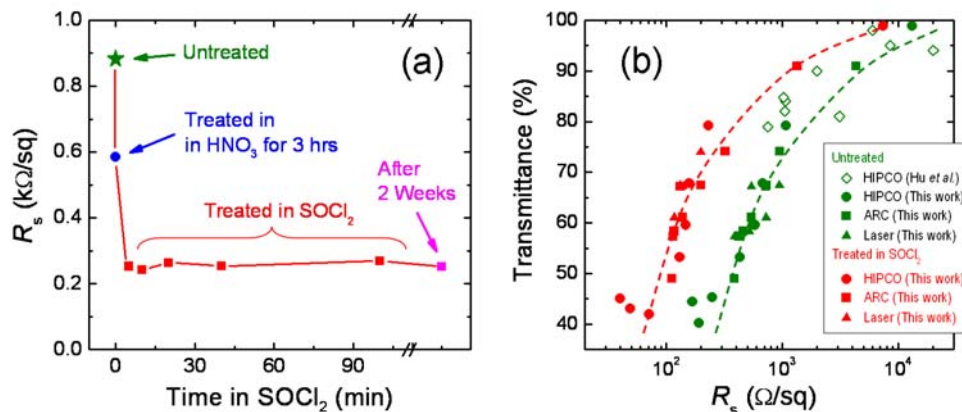


Fig 4.1 (a) The decrease in sheet resistance (R_s) as a function of time for a 40 mL SWNT thin film after HNO_3 and SOCl_2 treatments. (b) Film transmittance at 550 nm versus R_s for the various films found in the literature (Ref. ⁸⁰) and those investigated in this study (Laser, arc-discharge and HiPCO synthesized) and measured before and after the HNO_3 - SOCl_2 treatment.

4.3 Functional groups

Further insight into the effects of SOCl_2 treatment on the structure of SWNTs was obtained through Fourier-transform infrared (FTIR) spectroscopy. These spectra are shown in **Fig 4.2a**. It can be observed that the SWNTs exhibited very weak peaks before functionalization but, after the SOCl_2 treatment, strongly active C-Cl (950 cm^{-1}), C-C (1050 cm^{-1}) and C=O (1700 cm^{-1}) bond stretching modes¹²⁹ and activated C=C modes¹³⁰ (1600 cm^{-1}) can be readily seen. Such vibrations are the result of chemical attachment of functionals to the SWNTs, possibly in the form of acyl-chloride groups, in agreement with the TGA analysis. These findings are also consistent with our recent observations of acyl-bromide (COBr) groups in bromine functionalized SWNTs¹²².

It is interesting to note that, although the treatment in HNO_3 likely introduced some defects at the SWNT ends¹³¹ (and possibly also on the tube sidewalls¹³²), it does not appear to have any detrimental effect on the electrical properties of the SWNT thin films. In fact, after the HNO_3 treatment, we always observed a decrease of the sheet resistance, as demonstrated in **Fig 4.1a**. Such a phenomenon could be explained by assuming that the

dangling bonds or defects formed by the HNO_3 treatment are immediately passivated by hydroxyl (OH) or carboxyl (COOH) groups via formation of strong C–O or C–C bonds with the SWNT skeleton. Typically, defects have detrimental effects on the conductivity of carbon solids since they give rise to non-bonding electronic states lying near the Fermi level, which act as charge traps¹³³. However, C–C and C–O bonds give rise to σ -bonded electronic states, which are rather strong. As such, they do not produce charge-trapping states within the SWNTs.

In order to investigate the effect of temperature on the evolution of SOCl_2 functionals in detail, thermo-gravimetric analysis (TGA) was performed. For these measurements, SWNTs in powder form were soaked in HNO_3 and SOCl_2 baths, without attaching them to a substrate and the sample was recovered by centrifugation. **Fig 4.2b** compares the TGA profiles of untreated and HNO_3 - SOCl_2 treated HiPCO SWNTs. The differential TGA curve of the untreated specimen shows one single broad peak at 600°C , corresponding to the final loss of mass due to the oxidization and sublimation of the SWNTs¹²⁵. In contrast, the TGA curve of the functionalized SWNTs exhibits one additional peak at 450°C which we assign to the release of functionals related to SOCl_2 . This compares well with the temperature required for the release of acyl chloride (COCl) radicals in acetyl chloride and other compounds¹³⁴. Since the functionalized SWNT films are stable well above the annealing temperature of organic devices, SOCl_2 is likely to be useful for improving the conductivity of transparent SWNT films for such applications.

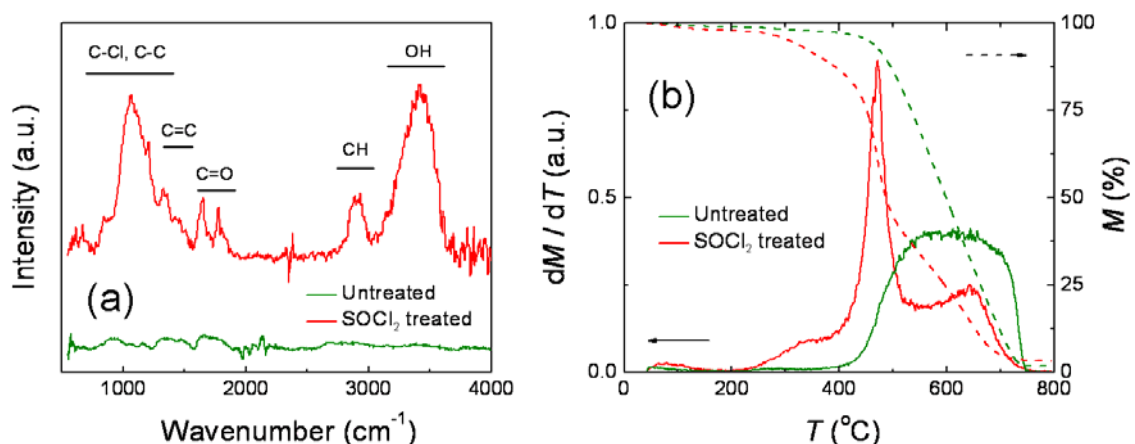


Fig 4.2 (a) FTIR spectra (Nicolet FTIR 6700 spectrometer) of the SWNTs before and after exposure to SOCl₂. The functionalized SWNTs show relatively more prominent peaks, possibly from COOH and COCl attachment. (b) TGA (Perkin Elmer Pyris analyzer) in air of untreated and SOCl₂ treated films from HiPCO SWNTs reporting mass loss (M , dotted lines) and differential mass loss (dM/dT , solid lines) as a function of temperature. The sharp peak at 450 °C may indicate the release of SOCl₂ related functionals. Such a relatively high desorption temperature is a strong indication that the functionals are chemically bonded to the SWNTs.

4.4 Morphology and work function

The atomic force microscopy (AFM) images of the pristine, HNO₃ treated, and SOCl₂ treated SWNT thin films are shown in **Fig 4.3a, b, and c**, respectively. Structurally, the SWNT thin films were observed to be rougher than ITO with average root mean square (rms) values of ~ 25 nm for the pristine films which increased to ~ 35 nm after dipping in HNO₃ and to ~ 40 nm after dipping in SOCl₂. The corresponding local work function mapping Kelvin probe force microscopy (KPFM) images are shown in **Fig 4.3d, e, and f**, respectively. The KPFM measurements reveal that the work function increases from 4.97 eV after acid treatment to 5.07 eV after SOCl₂ treatment compared to 4.86 eV for the untreated SWNT thin films. The different work functions are likely the results of changes in dipole magnitude and direction arising from the charge transfer at the donor-acceptor interface. The HNO₃ and SOCl₂ treatments increase the surface work function via

extraction of electrons from SWNTs due to the formation of carboxyl and hydroxyl groups and the nucleophilic Cl substitution which leads to the formation of COCl bonds^{135, 136}.

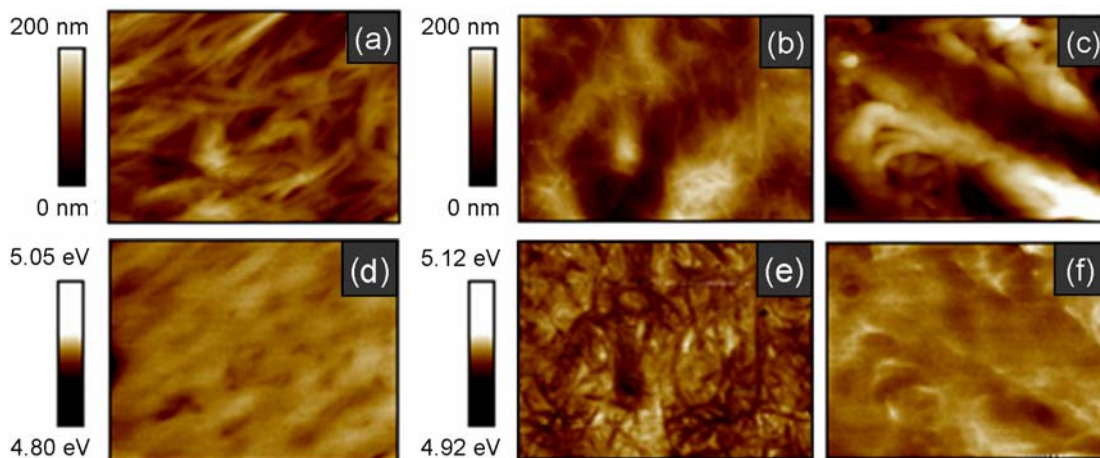


Fig 4.3 Tapping mode AFM (Digital Instruments, Nanoscope III) images of (a) SWNT thin films deposited from a suspension dispersed with SDBS surfactant, (b) treated with nitric acid, and (c) exposed to thionyl chloride. (d), (e) and (f) are the Kelvin probe force microscopy (KPFM) scans revealing that the work function increases from ~ 4.86 eV for the untreated SWNT thin films to ~ 5.07 eV for the Cl treated ones. For all measurements, Pt coated cantilevers at a resonant frequency of 75 kHz were utilized for all measurements.

4.5 Mechanical, thermal, and chemical stability

The SWNT thin films are found to be more flexible than ITO, as demonstrated in **Fig 4.4a** which shows the I - V curves of an ITO and a SOCl_2 treated SWNT thin film (50 mL) on PET before and after bending 10 times at 45° . During such a test, the resistance of ITO thin film increased by 4 orders of magnitude while the resistance of the SWNT thin film remained almost unchanged. We attribute the difference to the strong flexibility of the one dimensional SWNTs compared to the three-dimensional crystalline structure of ITO which can suffer from fatigue effects such as cracks and dislocations.

The effects of thermal annealing of the untreated and SOCl_2 treated thin films in

nitrogen atmosphere are plotted in **Fig 4.4b**. A similar, relatively low, increase of the sheet resistance with annealing temperature can be observed in both the treated and untreated films. Therefore the observed reduction cannot be assigned to the massive release of the SOCl_2 related functionals, which are probably still strongly attached even above $\sim 250^\circ\text{C}$.

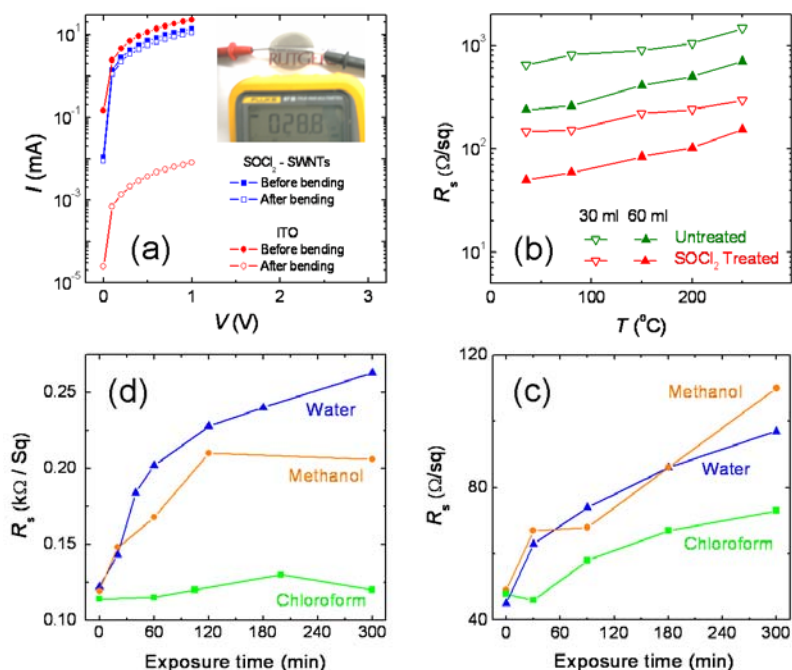


Fig 4.4 (a) I - V characteristics of ITO and SOCl_2 treated SWNT thin films after bending at 45° ten times. The ITO resistance increase by four orders of magnitude while the SWNT thin film conductivity remains almost unchanged. (b) Sheet resistance as a function of annealing temperature for untreated and SOCl_2 treated films (30 mL and 60 mL filtration volumes). (c,d) Sheet resistance as a function of exposure time in solvents for (c) 30 mL and (d) 60 mL SOCl_2 treated SWNT thin films. The lower sensitivity to chloroform can be observed. Even after 5 hours of solvent exposure, the sheet resistance of the SOCl_2 treated SWNT thin films is lower than the corresponding value prior to treatment (i.e. $\sim 950 \text{ } \Omega/\text{sq}$ at 30 mL and $\sim 250 \text{ } \Omega/\text{sq}$ at 60 ml).

Once OH or COOH groups are put in contact with SOCl_2 , a nucleophilic substitution by chlorine takes place so that SWNTs bonded with Cl or COCl are produced. As

demonstrated by our experiments, such functional groups have beneficial effects on the conductivity of SWNTs, in agreement with our previous observations with acyl bromide groups¹²². The mechanism responsible for the beneficial effects of halogenated functionals on the electrical properties of SWNTs in brominated SWNT thin films was elucidated with ab-initio simulations. We have shown that acyl bromide functionals, due to their strong electronegativity, act as electron acceptors, tending to move the Fermi level toward the valence band and to increase the hole density in SWNTs¹²². The movement of the Fermi level is expectably much weaker with acyl chlorides than with acyl bromides and this may result in lower hole density and in higher electron density in chlorinated SWNTs compared to brominated SWNTs. However, even under such conditions, chlorinated functionals are still able to dope SWNTs and improve their transport properties as evidenced by KPFM results. This can also explain the beneficial effects of the preliminary HNO₃ treatment on the thermal stability of SOCl₂ treated SWNT thin films. Indeed, in the absence of such treatment, SWNTs are much less defective and most of the SOCl₂ is simply physisorbed in the form of Cl⁻ ions, rather than being covalently bonded to the nanotubes. Such physisorbed ions can still dope the SWNTs to increase the conductivity but are relatively unstable when exposed to temperature or air.

We have exposed the SWNT thin films to various solvents used in organic electronics to test the stability of attached functional groups. The stability, in terms of the change in electrical properties, of the SOCl₂ treated SWNT thin films dipped in water, methanol and chloroform was investigated and the results are shown in **Fig 4.4c and d**. It is important to note that our films are relatively stable in chloroform even after prolonged exposure. This is significant because chloroform is widely used for spin-coating the polythiophene-fullerene blends used in organic photovoltaics¹²¹. In contrast, the conductivity of the SOCl₂ treated SWNT thin films decreases faster in water and alcohols, which are known to decompose acyl chlorides. However, as can be observed from **Fig 4.4c and d**, such decomposition is rather slow, occurring during temporal scales which are at

least one order of magnitude longer than the time required to assemble an organic solar cell by spin coating.

4.6 Effect of annealing and acid treatment on semiconducting thin films

We recently demonstrated that the SWNT thin films are semiconductors below the percolation threshold of metallic tubes⁸¹. Above the threshold, metallic SWNTs dominate the electrical conduction. In the previous Sections, properties of metallic thin films have been given the primary focus. In this Section and those following, device characteristics of semiconducting thin films are discussed. Semiconducting thin films consist of low density networks of tubes and generally exhibit resistance values that are several orders of magnitude larger than those of metallic thin films. A typical bottom-gated TFT with a SWNT thin film as the channel material as schematically shown in **Fig 4.4a** was studied. Surprisingly, annealing of semiconducting thin films in vacuum at 200 °C resulted in significant decrease in device resistance in contrast to the effect seen in metallic films as discussed in Section 4.5. These results indicate that the origin of electrical resistance in metallic and semiconducting thin films is different. Further, annealing resulted in ~ 1 order of magnitude improvement in field effect mobility and decrease in on/off ratio as shown in **Fig 4.5c**. An increase of off-current by two orders of magnitude suggests improved conduction via metallic tubes after annealing. It is unlikely that rearrangement of metallic SWNTs take place upon mild annealing conditions. Instead, the increase of off-current may be attributed to improved junctions between tubes and those between tubes and electrodes. A recent report by Geng *et al.*¹³⁷ suggests that residues of surfactants used to disperse SWNTs may degrade electrical conductivity of SWNT thin films due to their insulating nature. Removal of residual surfactants from SWNT network therefore leads to improved conductivity. Decomposition of SDS may not necessarily occur at 200 °C. However, this annealing temperature is sufficient to induce melting of SDS and therefore may allow improved π - π interaction between tubes.

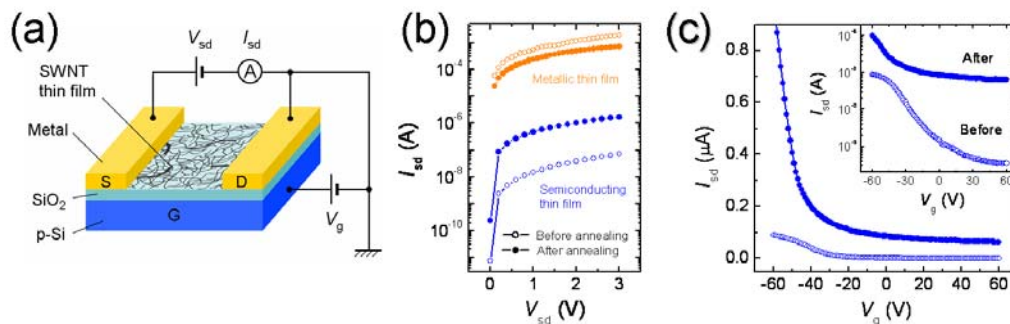


Fig 4.5 (a) Schematic of SWNT thin film transistor (TFT). (b) I - V characteristics of metallic and semiconducting SWNT thin films before and after annealing at 200 °C in vacuum. (c) Transfer characteristics of semiconducting SWNT thin films before and after annealing. Inset shows the same plot in log-scale.

Interpretations of the electrical properties of SWNT TFTs are often obscured by the presence of adsorbed species such as SDS. Geng *et al.*¹³⁷ demonstrated that acid treatment of SWNT thin films leads to removal SDS and achieved improvement of thin film conductivity by a factor of 2.5 similar to the effects observed in this study. Our results of KPFM and FTIR suggest that the improved conductivity may be attributed to doping and passivation effects rather than removal of residual surfactants. In order to gain further insight into the origin of conductivity improvement, we studied the effects of acid treatment on SWNT TFTs. To isolate the effects arising from removal of residual SDS in the thin films, we also fabricated control devices without using SDS. The SDS free devices were fabricated by dispersing SWNTs in chloroform and depositing using vacuum filtration method. The effect of HNO₃ treatment on the device transfer characteristics is shown in **Fig 4.6a and b**. The results clearly indicate that the source-drain current (I_{sd}) becomes nearly independent of gate voltages after HNO₃ treatment. The observed trends are the same for SDS and chloroform dispersed systems. In both cases, a decrease of sheet resistance by ~ 1 order of magnitude was observed indicating that removal of surfactant is

not the dominant cause of improved film conductivity. The effects of HNO_3 are immediate and persist after further treatment in a manner similar to those for SOCl_2 described in Section 4.2. One possible explanation for the significant increase of off-current (I_{sd}) is the degenerate doping of SWNTs by oxygen functional groups. However, further evidence for the doping level is required to understand the observed metallic behavior.

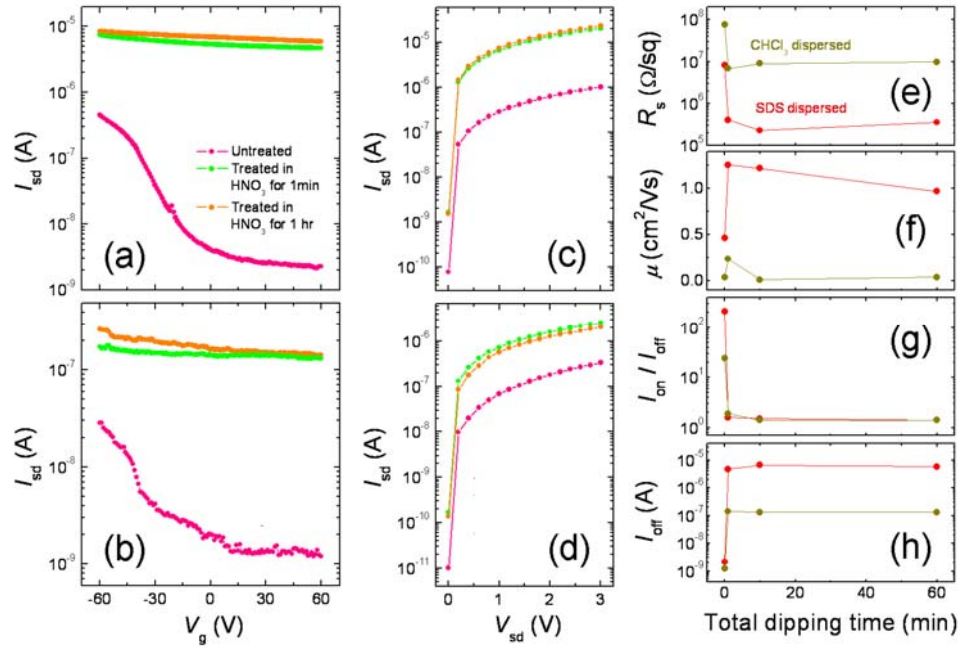


Fig 4.6 (a,b) Transfer characteristics and (c,d) I - V characteristics of SWNT TFTs for different HNO_3 treatment conditions. Effects were investigated for (a,c) SDS- and (b,d) chloroform-dispersed systems. (e) Sheet resistance (R_s), (f) field effect mobility (μ), (g) on/off ratio ($I_{\text{on}}/I_{\text{off}}$), and (h) off-current (I_{off}) of SWNT TFTs as a function of total dipping time in HNO_3 .

4.7 Effect of contact metals on semiconducting thin films

Field effects in SWNT-based transistors often result from modulation of the Schottky barrier formed between semiconducting SWNTs and electrode⁶⁷. Electrode metals and tube-metal interfaces therefore play a crucial role in determining the device characteristics. In random networks of SWNTs, carriers encounter numerous tube-tube junctions between

semiconducting and metallic tubes. A recent study suggests that the field effects in SWNT network TFTs also arise from modulation of junction resistance between a semiconducting and a metallic tube⁸⁶. However, the dominant mechanism of field modulated transport in SWNT network TFTs are not yet understood. We examined characteristics of SWNT TFTs fabricated using different metals and device configurations shown in **Fig 4.7a**. In normal conditions ($V_g = 0$ V) higher current was generally observed for devices with gold (Au) contacts as compared to those with Nickel (Ni) and Aluminum (Al). In metal-on-tube configurations, similar values of field effect mobility and on/off ratio were achieved in all devices. Major effects of metal contacts were observed in threshold voltages as shown in **Fig 4.7c**. More than five devices were tested for each metal and the average threshold voltages for Au, Ni, and Al electrode devices were found to be -10.5, -26.5, and -39.9 V, respectively. In tube-on-metal configurations, devices with Al and Ni electrodes did not show clear turn-on or turn-off behavior. In contrast, Au electrode devices did not show significant deviation in behavior from metal-on-tube counterpart. The results presented in **Fig 4.7c and d** clearly indicate the crucial role of electrodes for optimum device operation. The poor field modulation observed in Al and Ni electrode devices suggests the absence of Schottky barriers at the tube-electrode interface. It is likely that efficient charge transfer between SWNTs and the metal is prevented due to the presence of a thin oxide film on the metal surface due to exposure to ambient prior to nanotube deposition. Al and Ni are known to form such oxide layers in ambient conditions whereas Au is less prone to oxidation.

The threshold shifts shown in **Fig 4.7c** are explained by conjectured band diagram in **Fig 4.7e-g**. As the work function of Au (4.8 ~ 5.1 eV) is nearly the same or slightly larger than that of SWNT thin films (as discussed in Section 4.4), Schottky barriers in Au contacted devices are small (< 0.2 eV). In the normal state ($V_g = 0$ V), carriers can be injected from Au into SWNTs without experiencing a significant energy barrier, i.e. the devices are normally on. On the other hand, Al has a work function well below that of

SWNTs (~ 4.2 eV) and leads to formation of Schottky barriers which maybe as large as 0.6 eV. This manifests as large device resistance in the normal state.

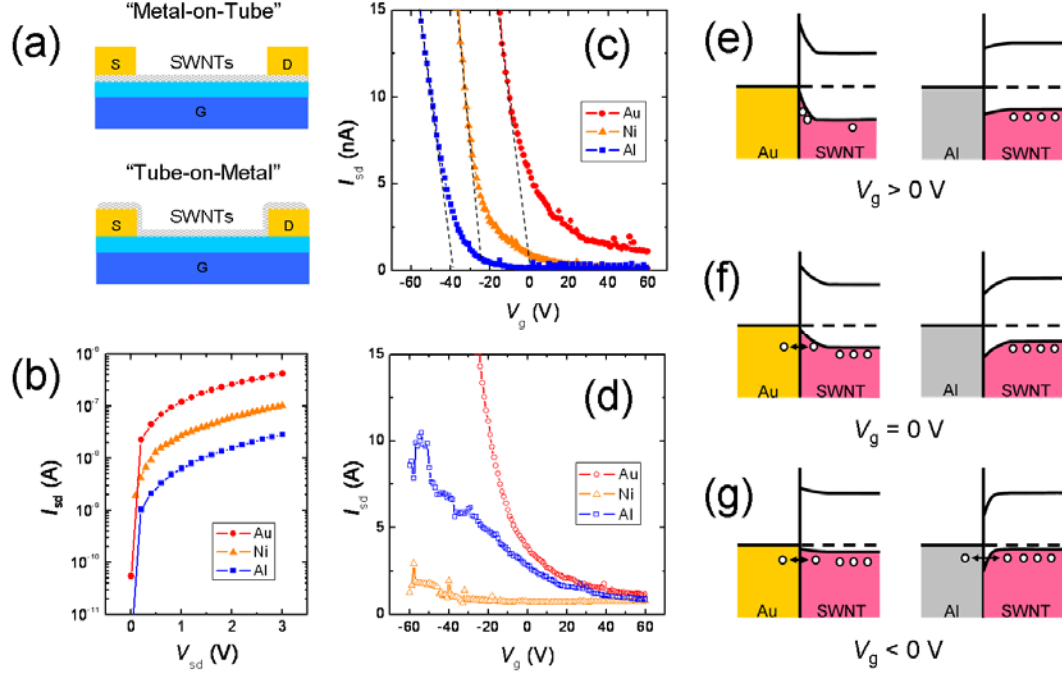


Fig 4.7 (a) Schematic of metal-on-tube and tube-on-metal device configurations. (b) I - V characteristics of metal-on-tube devices with different electrode metals. (c,d) Transfer characteristics of (c) metal-on-tube and (d) tube-on-metal devices with different electrode metals. (e-g) Conjectured band diagram of metal-SWNT interface at three gate bias conditions: (e) $V_g > 0$ V, (f) $V_g = 0$ V, and (g) $V_g < 0$ V.

4.8 Chapter summary

In summary, we have developed a simple room-temperature post-deposition procedure able to reduce the sheet resistivity of transparent and conducting SWNT thin films to values of 40 - 50 Ω/sq , which compares reasonably well with ITO, albeit at lower transparency (i.e. $\sim 50\%$ vs. 80%). We applied our SOCl_2 functionalization procedure after a preliminary treatment in HNO_3 to a wide range of thin films at different densities and prepared from different commercial sources of SWNTs. We suspect that the enhancement

in transport properties upon SOCl_2 treatment is related to the formation of acyl chloride functionals, in analogy to a similar effect we previously observed with acyl bromides¹²². Hole doping upon HNO_3 and SOCl_2 treatment was evidenced by the increase of thin film work functions. The compatibility of our functionalization procedure with commonly used solvents and thermal annealing has also been studied. We found that the SOCl_2 related functionals only slowly decompose in water and methanol, and they are reasonably stable in chloroform and at annealing temperatures of at least 250 °C in a nitrogen atmosphere. Semiconducting SWNT thin films become metallic after HNO_3 treatment possibly due to degenerate doping of semiconducting SWNTs. SWNT TFTs operate in Schottky modulation mode and threshold voltage shifts with electrode material.

Chapter 5

Bundling of single-walled carbon nanotubes in aqueous suspensions

Networks of single-walled carbon nanotubes (SWNTs) are interesting electronic materials that have opened a route to new class of thin film devices⁷⁹. While individual SWNTs have been considered as ideal building blocks for nano-electronics, the intense effort required to disperse¹³⁸, separate¹³⁹, and manipulate them have limited their implementation in electronic devices. In contrast, SWNT thin film electronics takes advantage of ease of processing because it does not require intense molecule-level

manipulation. SWNT thin films can either be grown directly onto substrates at high temperatures (700-900 °C) or more preferably deposited from solution. Solution processing is particularly important for the emerging field of printable electronics where the components of the device can be deposited from suspension or “inks” consisting of nano-particles in solvents using inkjet or roll-to-roll printing onto inexpensive, flexible substrates^{82, 140-143}. Promising results for applications in transparent and conducting electrodes^{116, 117, 144}, thin film transistors^{77, 145} (TFTs), optoelectronic devices¹⁴⁶⁻¹⁴⁸, and chemical sensors³¹ have been reported for a variety of solution processed materials.

In order for solution processed SWNT thin film electronics to be viable, it is crucial that devices with consistent performance be fabricated. One of the primary limitations to reproducibility of SWNT thin film devices is the occurrence of bundling in suspension or during deposition. Bundling is detrimental for the opto-electronic properties of SWNT thin films due to an increase in surface roughness and also their large optical cross-section. In addition, bundles are metallic¹⁷ and therefore give rise to a large off-current in SWNT thin films transistors (TFTs)¹⁴⁵. Furthermore, since bundling often occurs in a non-repeatable manner, it manifests as non-reproducible characteristics in SWNT thin film devices. Therefore, real time monitoring of the bundling dynamics in SWNT suspensions is critical for fabrication of devices with reproducible properties. However, dynamics of SWNT bundle formation in suspensions are not clearly understood. While various spectroscopic^{59, 74, 149, 150} and scattering¹⁵¹⁻¹⁵³ techniques may be used to infer the aggregation state of SWNTs, bundling kinetics in solution are difficult to probe due to complications introduced by sedimentation¹⁵⁴ and diffusion¹⁵³.

In this Chapter, we describe a simple method to monitor the settling behavior of SWNTs in aqueous suspensions. The method involves monitoring absorbance of the suspension at three different heights as a function of time. For well dispersed suspensions, the absorbance was found to be constant for the first ~ 0.1 hours, after which modulations in the data appeared. Specifically, since our AFM and SEM studies of SWNT bundle sizes

from samples taken from the suspensions reveal diameters ranging from a few nanometers up to the order of the wavelength used to measure the absorbance, we show that the modulations can be correlated to resonances predicted by Mie theory of light scattering from cylindrical nano-particles. It should therefore be noted that here the term absorbance refers to attenuation of light by two phenomena: light scattering and absorption effects within the particles. Semi-quantitative interpretation of our absorbance data reveals that the aggregation of SWNTs in the suspension is a highly dynamic process in which an increase in the bundles size occurs upon termination of sonication. According to our observations, gradual bundling takes place until a critical mass is reached (at ~ 10 hours of settling time) when the bundles precipitate. At longer settling times, precipitation of the bundles continue while lighter particles with little tendency to aggregate, presumably individual SWNTs, or very small bundles, remain in suspension. Finally, to correlate the dynamic behavior of SWNT suspensions to electronic characteristics, we have measured the electrical properties of thin films from SWNTs sampled at various times from the center of the vessel. We found that the sheet resistance of the SWNT thin films decreased with settling time, reaching a minimum at ~ 10 hours and subsequently increased to approximately the same value as SWNT thin films deposited from freshly sonicated solutions. The on/off ratio of the SWNT TFTs was also found to follow a similar trend.

5.1 Measurement apparatus

SWNTs synthesized by high-pressure catalytic decomposition of carbon monoxide (HiPCO) purchased from Carbon Solutions, Inc. and thoroughly purified by a process described elsewhere¹²⁵ were used in this study. Purified SWNTs were solubilized in an aqueous solution of 1 wt. % sodium dodecyl sulfate (SDS) at a concentration of 2 mg/L. Prior to performing the optical measurements, the SWNT suspensions were homogenized by bath sonication for 2 hours to achieve a uniform ink. An additional SWNT suspension of 1 wt% SDS and methanol was also investigated for comparison. The dispersion stability

of the methanol containing suspension is poor because methanol has a strong affinity for SDS which causes the surfactant to desorb from the SWNTs¹⁴¹, promoting rapid bundling. The bundling dynamics and dispersion stability of the two suspensions were investigated by monitoring the absorbance of a red diode laser ($\lambda = 655 \text{ nm}$) with photodiodes at three different heights (top, middle, and bottom) of the vessel, as schematically shown in **Fig 5.1**. It should be noted that the term absorbance is used to describe the attenuation of the incident beam as explained in details in Section 5.4. The absorbance at the three levels was recorded every 5 seconds for over 100 hours starting immediately after sonication.

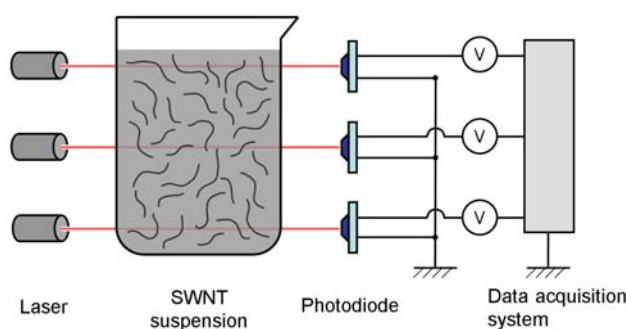


Fig 5.1 Schematic of measurement apparatus. Red lasers ($\lambda = 655 \text{ nm}$) were used to monitor the absorbance.

5.2 Experimental observation of suspension dynamics

The measured absorbance values as a function of time for the two suspensions are plotted in **Fig 5.2a and b**. The data for the methanol containing suspension shown in **Fig 5.2a** follow an expected trend for suspensions of heavy particles. In such systems, sedimentation of bundles of varying masses with different Stokes velocities results in development of a concentration gradient from the top to the bottom of the suspension¹⁵⁵. This is readily seen as decay in absorbance beginning from the top of the suspension. This type of settling behavior can be described by classical equations of motion as demonstrated by Nicolosi *et al.*¹⁵⁴ for sedimentation of MoSI nanowires. In this case, the absorbance

generally remains constant for up to a critical time, after which it decays exponentially, demonstrating that bundling takes place immediately upon the addition of methanol followed by sedimentation.

In contrast, the behavior of absorbance of well dispersed suspension without methanol shown in **Fig 5.2b** is more complex. Absorbance remains relatively constant for all three laser positions up to ~ 0.1 hours above which it decreases and then increases again for several hours, giving rise to two broad features at all three laser positions. The features are more dramatic at the bottom of the vessel possibly due to a higher concentration of material from precipitation. Small modulations superimposed on the broad features can also be readily seen on each curve. Subsequently, exponential decay similar to methanol containing suspension is observed after ~ 10 hours. The anomalous behavior between ~ 0.1 and ~ 10 hours can be attributed to gradually increasing size and amount of SWNT bundles. We will explain the origin of the two broad peaks and also the smaller superimposed modulations in detail below.

Before launching into the theory, major features of the absorbance curve in **Fig 5.2b** can be summarized in terms of three regimes. Regime I is the plateau up to around 0.1 hours implying good dispersion where absorbance is dominated by individual SWNTs and/or limited volume fraction of bundles. Regime II ($0.1 < t < 10$ hours) is characterized by a broad dip and appearance of small modulations arising from increasing bundle size. Finally, regime III ($t > 10$ hours) is characterized by exponential decay due to sedimentation of large bundles. These three regimes are depicted schematically in **Fig 5.2c, d, and e**, respectively.

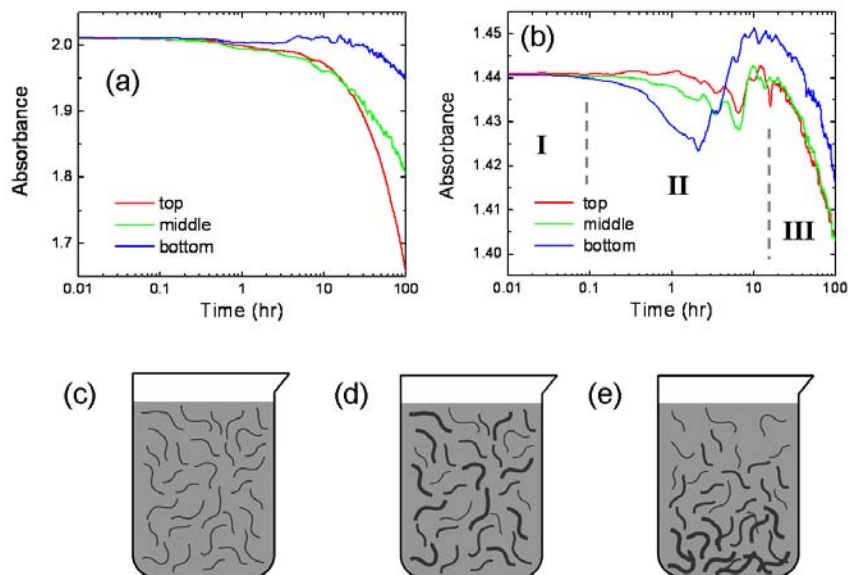


Fig 5.2 Measured absorbance as a function of time for (a) poorly dispersed and (b) well dispersed suspensions. Three settling regimes for well dispersed suspensions are indicated with Roman numerals (see text). Evolution of the state of SWNT suspension is depicted in (c-e). Initially (c) well dispersed SWNTs (d) aggregate into bundles and subsequently (e) precipitate to the bottom with progressing settling time.

5.3 Attenuation of light by individual nanotubes and bundles

In order to obtain insight into the bundling dynamics and a physical picture of the mechanisms involved, we have performed semi-quantitative analysis of the experimental absorbance data. For the analysis, we assume that the measured absorbance of the suspension is a sum of two contributions such that $A_{\text{total}} = A_{\text{indiv}} + A_{\text{bundle}}$ where A_{indiv} is the absorbance due to individual SWNTs or very small bundles (few nanometers in diameter), and A_{bundle} is due to absorbance from large bundles (few tens to hundreds of nanometers in diameter). Therefore, A_{indiv} is primarily influenced by changes in the effective medium consisting of SWNTs and SDS solution. This assumption is based on the fact that from our AFM analysis, SWNT thin films prepared from the suspension typically contain large fraction of well dispersed SWNTs (bundles below ~ 10 nm in diameter) along with a small

fraction of large bundles (> 10 nm in diameter). The contribution of these two terms in measured absorbance is described in **Fig 5.3a** (actual data from **Fig 5.2b** have been used to illustrate the modeled phenomena). The illustration depicts the exponential decay in the effective medium (blue curve) as well as the modulations due to Mie scattering from increasing fraction of bundles with diameters close to being in resonance with the probing wavelength (red curve). For clarity and better interpretation of the contribution from large bundles, the decay in effective medium was modeled with a stretched exponential function and subtracted from the experimental absorbance data. The data for the middle laser in **Fig 5.2b** after subtraction of the effective medium contribution are replotted in **Fig 5.3b**. The plot shows resonance peaks with varying intensities indicating increasing size and variable fraction of bundles. In **Fig 5.3a and b**, the peak positions are labeled as d_0, d_1, d_2 and so on where d_0 is defined as the critical bundle size for the initial principal maximum and the modulations as d_i ($i = 1, 2, 3 \dots$). Below, we semi-quantitatively explain our observations in terms of cross-section enhanced Mie scattering from suspended cylindrical particles¹⁵⁶ and demonstrate how the peak positions in the experimental absorbance data can be used to obtain the size of particles in suspension.

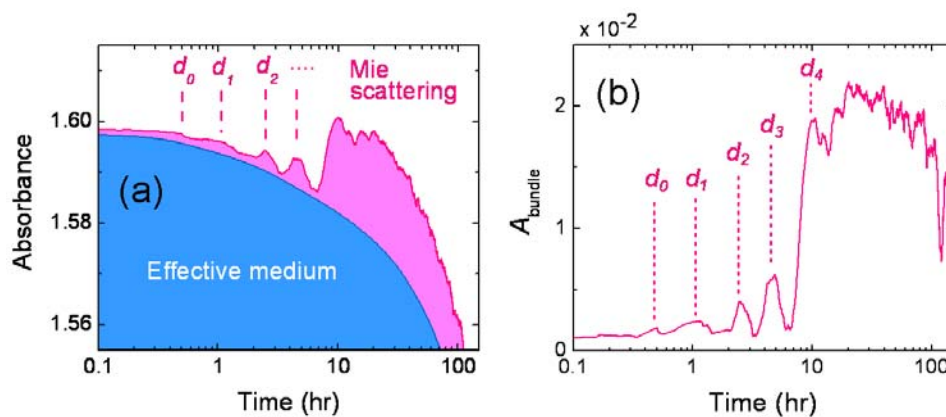


Fig 5.3 (a) Schematic of the model used for the interpretation of optical absorbance with time. The contribution of the small particles in a well dispersed suspension to the absorbance is represented by the blue curve as an exponential decrease in the absorbance due to the depletion of the effective

medium. The contribution of the cross-section enhanced Mie scattering from bundles is represented by the resonance peaks shown in red. The Mie scattering peaks (d_n) are labeled on the red curve. (b) Replotted experimental absorbance data with the contribution from the effective medium subtracted for the middle laser to clearly identify the resonance peaks.

5.4 Mie scattering for cylindrical particles

Attenuation of electromagnetic waves incident on small particles with size comparable to the wavelength is particle-size dependent due to complex interference of scattered electromagnetic waves. The Mie theory provides analytical solutions to the Maxwell equations describing these complex phenomena. Assuming SWNT bundles as infinitely long cylindrical particles attenuating the laser beam, the Mie theory can be applied to model the origin of the observed peaks in **Fig 5.2b**.

Attenuation of a suspension consisting of cylindrical particles can be expressed as:

$$A = \frac{f \cdot Q_{ext}}{\pi d} L \quad (5.1)$$

where f is the volume fraction occupied by the particles, d is the particle diameter, L is the width of the vessel containing the solution, Q_{ext} is the extinction cross-section, resulting from two distinct phenomena: absorption and scattering of incident light by the illuminated particles. Extinction cross-section can be expressed as¹⁵⁶:

$$Q_{ext} = \frac{2}{x} \sum_{n=1}^{\infty} \text{Re} \left\{ b_{0I}(x) + 2 \sum_{n=1}^{\infty} b_{nI}(x) + a_{0II}(x) + 2 \sum_{n=1}^{\infty} a_{nII}(x) \right\} \quad (5.2)$$

where the harmonic coefficients a_{nII} and b_{nI} are related to the n -th order solution of the Maxwell equations for an incident plane wave with boundary conditions determined by the geometry of the particles. These coefficients depend on the diameter of the particles and the refractive index N of the background medium (aqueous solution with 1 wt. % SDS) through the size parameter: $x = 2\pi Nd/\lambda$. The a_{nII} coefficients are related to absorption and scattering of incident radiation polarized perpendicular to the axis of the cylindrical particles, while the b_{nI} coefficients are related to those of incident radiation polarized

parallel to the particle axes. Therefore, for optically anisotropic cylinders, the a_{nII} coefficients depend only on the out-of-axis refractive index of the particles, N_{\perp} , while the b_{nI} coefficients depend only on the in-axis refractive index of the particles, N_{\parallel} :

$$\begin{aligned} a_{n,II} &= \frac{C_n(M_{\perp}, \zeta, x) \cdot V_n(M_{\perp}, \zeta, x) - B_n(M_{\perp}, \zeta, x) \cdot D_n(M_{\perp}, \zeta, x)}{W_n(M_{\perp}, \zeta, x) \cdot V_n(M_{\perp}, \zeta, x) + iD_n(M_{\perp}, \zeta, x)^2} \\ b_{n,I} &= \frac{W_n(M_{\parallel}, \zeta, x) \cdot B_n(M_{\parallel}, \zeta, x) + iD_n(M_{\parallel}, \zeta, x) \cdot C_n(M_{\parallel}, \zeta, x)}{W_n(M_{\parallel}, \zeta, x) \cdot V_n(M_{\parallel}, \zeta, x) + iD_n(M_{\parallel}, \zeta, x)^2} \end{aligned} \quad (5.3)$$

where A_n , B_n , C_n , D_n , V_n and W_n are quantities that, related to the n th order cylindrically symmetric Bessel and Hankel functions¹⁵⁶, preserve information about the geometry of the particles. They depend on $M_{\parallel} = N_{\parallel} / N$ or $M_{\perp} = N_{\perp} / N$ and on the incidence angle, ζ . Except for the zeroth order solutions, both a_{nII} and b_{nI} approach zero for sufficiently large values of n and sufficiently low values of x .

5.5 Simulation of cross-section enhancement

The evaluation of **Eqn 5.2** can then be carried out by retaining a finite number of terms in the summation. In order to determine M_{\parallel} and M_{\perp} , the complex refractive indices of HiPCO SWNTs recently reported by Fagan et al.¹⁵⁷ The extinction cross-section versus the bundle diameter was calculated at several values of N (near values for pure water $N = 1.30$ at $\lambda = 655$ nm) to account for possible changes in the refractive index of the aqueous medium. The results of our calculations for various values of N are summarized in **Fig 5.4a**. The prominent d_0 peak arising from the nucleation of bundles of critical sizes is readily obtained as the initial principal maximum from the calculations. The intervals between the modulations in **Fig 5.4a** represent the change in particle size (Δd) with time. Thus, our calculations suggest that it is possible to obtain the size of bundles as a function of settling time from the intervals between the modulations in the experimental absorbance measurements (**Fig 5.3b**). It can be observed from **Fig 5.4a** that for the most likely values of refractive index for water-SDS effective medium ($N = 1.24 - 1.4$), both d_0 and Δd only weakly depend on N . The inset in **Fig 5.4a** is an enlargement of the calculated results at low

particle sizes to clearly indicate that there are no resonance peaks below d_0 . The values of d_0 and Δd were found to be 34 and 152 nm, respectively, for $N = 1.3$.

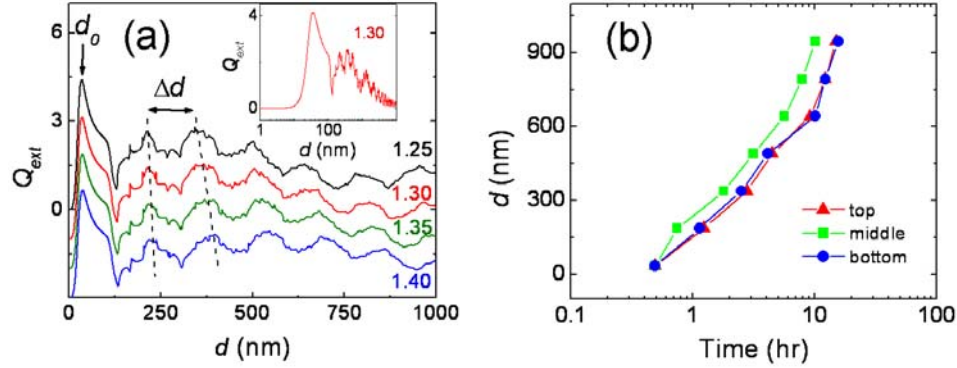


Fig 5.4 (a) Enhanced cross-section Q_{ext} versus bundle size for particles with $N_{//} = 1.7 + i0.7$ and $N_{//} = 3.5 + i2.5$ (realistic values for HiPCO SWNTs) at various medium refractive indices. The initial particle size of the bundles (d_0) was calculated to be ~ 34 nm and each subsequent peak indicates the growth of the bundles by Δd . The curves for $N = 1.3 \sim 1.4$ are offset for clarity. The inset emphasizes that no cross-section enhancement is present for particle sizes below ~ 10 nm. (b) Summary of bundle diameters as a function of time extracted from the absorbance data.

5.6 Calculation of bundle size

The results of our simulations suggest that during the time between two consecutive resonance peaks, bundle diameters increase by ~ 150 nm. The multiple peaks in the absorbance data (**Fig 5.3b**) indicate formation of large bundles, consistent with the fact that we occasionally find bundles of several hundred nanometers in the SWNT thin films. Assuming that each resonance peak in **Fig 5.3b** represents absorbance from the most prevalent bundles within the probed volume, the bundle size as a function of settling time can be extracted by utilizing d_0 and Δd as shown in **Fig 5.4b**. The increase in the average bundle size within the probed volume at the three locations within the vessel can be readily seen. Furthermore, it can also be concluded from **Fig 5.4b** that the estimated bundle size at $t > 10$ hours is sufficiently large for sedimentation to occur according to Stokes Law. This

correlates well with the onset of regime III in **Fig 5.2b**, where precipitation of bundles becomes significant. Therefore, the small modulations in **Fig 5.3b** can be attributed to resonance while the broad increase in absorbance prior to the exponential decay can be attributed to the overall increase in the bundle concentration. It should be noted that the small intensity of resonance modulations superimposed on the broad feature in **Fig 5.2b** and **Fig 5.3b** indicates that the fraction of large bundles is small compared to those of individual SWNTs and small bundles (< 10 nm in diameter).

5.7 Electrical resistance of thin films

In order to investigate the impact of the complex settling behavior on the electronic properties of SWNT networks, thin films were prepared at different times after sonication. We define the time elapsed from sonication as “settling time,” t_s . A small amount of suspension (3 mL) was carefully sampled from the center of the vessel at the same location for all measurements and diluted to 0.05 mg/L with 1 wt% SDS solution. It should be pointed out that bundling rate is greatly reduced at this point due to lower probability of bundle-bundle interactions through dilution. Debundling, which is an irreversible process⁷⁴, is also unlikely. The diluted suspension was then vacuum filtrated to “freeze” the aggregation state into a two dimensional structure. A filtration volume of 60 mL at this concentration was chosen to yield a low density film below the metallic percolation threshold⁸¹. Electrical properties were evaluated for SWNT thin films deposited onto SiO₂/p-Si substrates with evaporated Au electrodes.

Electrical measurements were performed at different locations on the substrates to account for variations arising from fluctuations in tube density within the film. Large channel separation (L_c) of 20 μ m, which is much greater than the length of individual SWNTs, was chosen to ensure that the transport was dominated by percolation¹⁵⁸. Histograms showing the distribution of measured R_s at different t_s are shown in **Fig 5.5a**. The average R_s was found to reach a minimum at $t_s = 10$ h, as clearly shown in **Fig 5.5b**.

This time coincides with the end of regime II discussed earlier in the absorbance data (**Fig 5.2b**), which corresponds to maturing of bundle size before precipitation. A typical AFM image showing the range of bundle sizes in the SWNT thin films deposited after a settling time of 10 hours is shown in **Fig 5.5c**. The changes in R_s in terms of degree of bundling can be qualitatively explained by considering percolation of metallic SWNTs in bundles. That is, due to the high probability that a bundle contains several metallic SWNTs, percolation amongst the bundles effectively acts as a long conducting channel. The gradual increase in R_s for $t_s > 10$ h corresponds with regime III of absorbance spectrum where the number of large bundles decreases at the center of the vessel due to sedimentation. Tube density of the resulting network diminishes and so does the probability of metallic SWNT percolation, resulting in higher R_s . The distribution of bundles within the conducting channel as a function of the settling times is schematically summarized in **Fig 5.5d**.

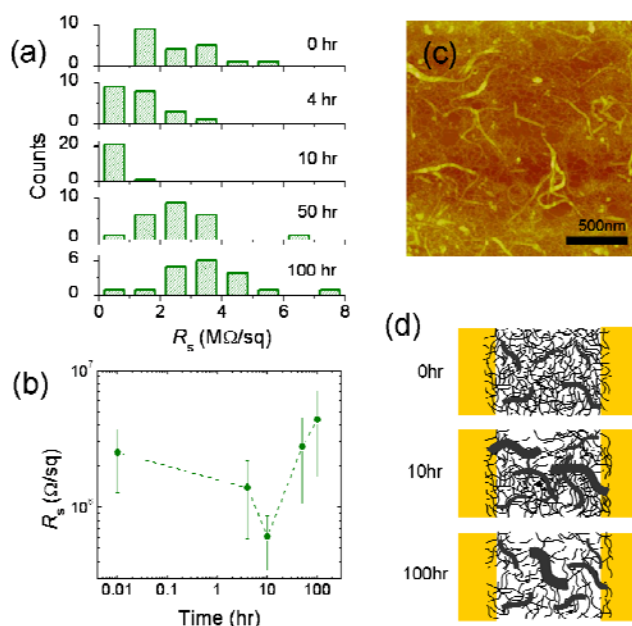


Fig 5.5 (a) Distribution of measured R_s for different t_s . (b) Average sheet resistances (R_s) for SWNT thin films prepared at different settling times. The minimum sheet resistance was found at settling times = 10 hours. (c) Typical AFM image of the prepared thin film showing individual SWNTs and bundles of few tens of nanometers in diameter can be readily observed. (d) Schematic

representation of SWNT network showing different degrees of bundle percolation as a function of the settling time. The schematic shows bundles percolating across the network for settling time of around 10 hours, giving rise to minimum R_s .

5.8 Thin film transistor characteristics and suspension dynamics

Evidence for metallic SWNT percolation was also found in TFT characteristics as shown in Figure 4. All the devices examined in this study exhibited the typically observed p-type behavior¹⁴⁵, as indicated by the transfer characteristics in **Fig 5.6a**. It should be noted that the measurements were made without elimination of metallic SWNTs⁷⁵ in order to understand the effect of bundles on device performance. We chose a large channel length ($L_c = 220 \mu\text{m}$) in order to clearly observe the variations in the on/off ratio of the TFTs. The on/off ratios were found to depend on t_s as shown in **Fig 5.6b**. As it has been discussed by Kocabas *et al.*¹⁵⁹, the on/off ratio of SWNT TFTs is sensitive to percolation of metallic SWNTs which gives rise to a large off current. It is clearly seen that the on/off ratio is suppressed for films prepared in regime II ($t_s = 2 \sim 10$ hours) where large off currents are obtained due to the percolation of bundles. The higher fraction of bundles in the channel is the result of aggregation at these intermediate settling times. In regime III, the on/off ratio recovers by an order of magnitude due to the reduced total amount of metallic SWNTs resulting from precipitation, in agreement with the behavior of R_s .

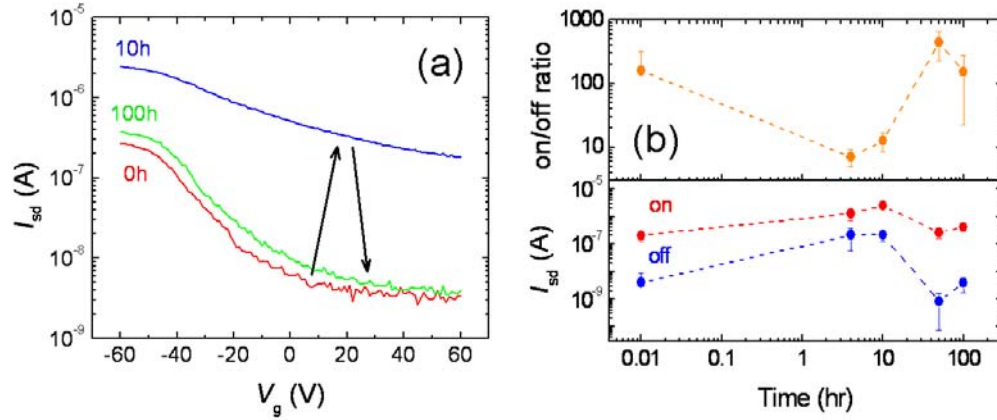


Fig 5.6 (a) TFT characteristics of typical devices for thin films deposited at settling times of 0 hr, 10 hr, and 100 hr. (b) Variation of on/off ratio and on- and off-currents for SWNT TFTs prepared at different settling times. Leakage (off-) current increases more than an order of magnitude during the initial 10 hours giving rise to low on/off ratio.

We further observed that the variation of on/off ratio within each film is typically a function of R_s , as plotted in **Fig 5.7**. It can be seen that the relationship between the on/off ratio and R_s also changes with t_s . For example, while similar on/off ratios are achieved for regimes I and III, there is a distinct horizontal shift (increase in sheet resistance) in the two groups of data. The primary difference in the films prepared in these regimes is the amount of individual SWNTs. In regime III, the number of individual SWNTs is less compared to regime I due to bundling. This implies that the large number of cross junctions⁸⁴ present in films prepared during regime I may give rise to larger R_s . In this respect, the relationship between the on/off ratio and R_s may be a key in understanding the quality of SWNT network.

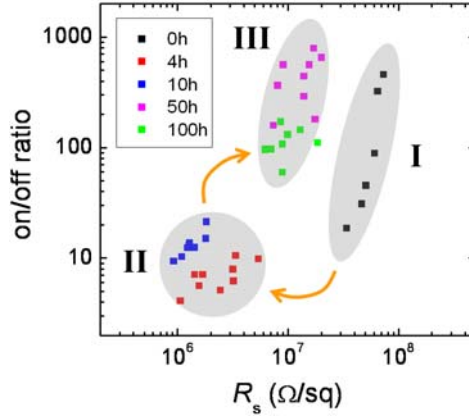


Fig 5.7 On/off ratio of each TFT device mapped against sheet resistance (R_s). The device characteristics mostly fall within the three shaded regions depending on the settling regime.

5.9 Chapter summary

We have presented a simple optical method for diagnosing the bundling and sedimentation dynamics of SWNTs in suspension. This method exploits resonances that arise from Mie scattering of a laser beam by SWNT bundles with sizes in the range of few tens to hundreds of nanometers. With this method, we determined that the bundle diameter increases rapidly with time as soon as agitation by sonication is terminated. We also showed that bundling and sedimentation dynamics in suspension give rise to significant variations in electrical properties of SWNT networks. SWNT thin films containing large bundles exhibit a large off current due to high probability of metallic percolation paths present in the network. In order to obtain SWNT thin films with reproducible properties, it is crucial that the state of suspensions is known. Improvement towards determining and maintaining highly dispersed and stable suspensions is essential for achieving SWNT network devices with enhanced performance and reproducibility.

Chapter 6

Chemically derived graphene and its thin films: preparation, chemical and structural properties

Graphene is a one-atom-thick layer of carbon with remarkable electronic properties that have focused the attention of scientists and engineers³⁷. In particular, graphene is a semiconductor with zero band gap and high carrier mobilities and concentrations, and shows near-ballistic transport at room temperature^{19, 98}. A challenging aspect of graphene integration into electronic devices is the exfoliation of graphite into individual sheets in a controlled, scalable and reproducible way. The reliable technique to produce single layer

graphene of high quality is the micromechanical cleavage using Scotch Tape^{5, 43}. However, this route is not practical for large-scale integration of graphene due to low yield. Exfoliation of individual to few layered graphene sheets via agitation in carefully chosen solvents and achieving a stable suspension has been recently investigated¹⁶⁰. However, the reported yield of single-layered graphene was found to be disappointingly small (< 1 wt%). Growth of graphene on specific substrates (SiC and on transition metals) has also been demonstrated¹⁶¹⁻¹⁶⁴. However, it is unclear if uniform deposition over large areas can be obtained using these methods and whether the grown graphene can be easily transferred onto more desirable substrates. Recent progress on transfer printing of CVD grown graphene appears to be promising for large area electronics^{165, 166}.

Oxidation of graphite offers a route to efficient exfoliation into individual sheets of monolayer graphene oxide (GO)¹⁰⁵. The individual GO sheets can be readily deposited on virtually any substrate over large areas using solution based methods¹⁶⁷. GO is formed with a range of O:C stoichiometries, with oxygen bonded to carbon in the graphene basal plane in the form of hydroxyl and epoxy functional groups (in variable ratios depending on the synthesis protocol)^{168, 169} and as carbonyl and carboxyl groups at the sheet edges. These functional groups make GO sheets strongly hydrophilic and decrease the interaction energy between the graphene layers (the interlayer distance increases from ~ 0.35 nm in graphite to ~ 0.7 nm in oxidized graphite)^{170, 171}. Hence, graphite oxide can be readily exfoliated, forming a stable aqueous dispersion. A complete model to describe the exact ratio and spatial distribution of the functional groups that decorate the graphene lattice has yet to be elucidated¹⁷¹⁻¹⁷³.

Graphene oxide is electrically insulating and must be reduced (using chemical and/or thermal treatment) to make it electrically active¹⁴. Although other methods have been reported¹⁷⁴, the most widely used chemical route to reduce GO in solution as well as after deposition onto substrates is exposure to hydrazine^{106, 107, 167, 175-179}. To further improve the electrical properties of reduced GO (r-GO), the hydrazine treatment is usually

followed by thermal annealing (200-500 °C)^{107, 167, 178}. Although these reduction treatments have yielded reasonably good opto-electronic properties, the final electrical transport properties^{106, 107} (such as field effect mobility in a transistor geometry) are far from those of graphene³⁴. Obtaining optimum electrical properties of r-GO has been challenging due to the lack of knowledge regarding the chemical and structural characteristics of r-GO.

Although various properties of r-GO have been reported, detailed studies correlating the structure with optical and electrical properties have been lacking. Here we present a comprehensive description of electronic properties, chemical state and the structure of uniform GO thin films at different stages of the reduction process. We applied two reduction processes to GO: (i) exposure to hydrazine monohydrate vapor and (ii) thermal annealing in different environments. We also analyzed the suitability of combined hydrazine and thermal reduction treatments to achieve the desired electrical properties. The present reduction methods utilizing hydrazine and high temperature annealing are not ideal for environmental and technological reasons, respectively. However, understanding the structural and chemical changes that occur during reduction may allow the development of alternative processes.

In this Chapter, preparation and characterization of chemically derived graphene and its thin films are described.

6.1 Synthesis of graphene oxide

Oxidation of graphite was conducted using modified Hummer's method described in Ref. ¹⁸⁰. Natural graphite flakes from two different sources (Bay Carbon Inc. and Branwell Graphite Ltd.) have been used. A mixture of 5 g of graphite and 3.8 g of NaNO₃ was placed in a flask cooled in an ice bath. H₂SO₄ (169 mL) was added to the mixture and stirred until homogenized. KMnO₄ (22.5 g) was gradually added over an hour to the solution while stirring. The solution was removed from the ice bath after 2 hours, and was further stirred for 5 days to obtain a brown-colored viscous slurry. The slurry was added to 500 mL

aqueous solution of 5 wt. % H_2SO_4 over 1 hour while being continuously stirred. The mixture was stirred for a further 2 hours. Then H_2O_2 (30 wt. % aqueous solution) was then added to the mixture and stirred for further 2 hours.

The mixture was purified by dispersing and precipitating the above mixture in 500 mL aqueous solution of 3 wt. % H_2SO_4 and 0.5 wt. % H_2O_2 . After two days of precipitation, supernatant solution was removed. This process was repeated ten times. The slurry (0.5 mL) was then dispersed in 500 mL of deionized water by ultrasonication to achieve a clear yellow suspension of exfoliated graphene oxide (GO). The suspension was allowed to stand for more than a month to allow precipitation of residual impurities. Supernatant of this suspension was found to be extremely stable for extended period of time without further precipitation. This parent suspension was diluted to different degrees and used for further study.

The concentration of the resultant GO suspension was determined by first determining the concentration of GO in the slurry. A known amount of slurry was dried over P_2O_5 for 1 week in a vacuum dessicator. From the weight of the dry GO product, the concentration of GO in the slurry was found to be 49 mg/mL. The concentration of the above mentioned supernatant suspension of GO was estimated by monitoring the change in absorbance over the precipitation period. This yielded a value of 12.5 mg/L.

The GO flakes in the suspension are irregularly shaped and therefore specific lateral dimensions are difficult to obtain, however, our AFM, SEM and optical microscopy analysis yield a size range of 200 nm – 20 μm .

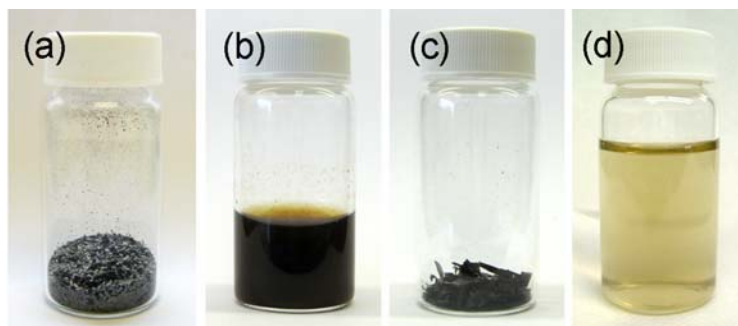


Fig 6.1 Photographs showing (a) pristine graphite flakes, (b) slurry of graphite oxide, (c) dried graphite oxide, and (d) dilute suspension of graphene oxide.

GO is soluble in water due to the presence of carboxyl and hydroxyl groups, allowing it to readily exfoliate into individual sheets in water with mild agitation¹⁰⁵. Optical and atomic force microscope (AFM) images of graphene oxide on SiO₂/Si substrates are shown in **Fig 6.2a and b**. Most graphene flakes were monolayers and the AFM scan profiles show that the height of these flakes is approximately 1 ~ 1.2 nm (**Fig 6.2c and d**) in agreement with previous works^{105, 181}. Monolayers of GO were readily visible on Si substrates with 300 nm SiO₂ as it is also the case for mechanically exfoliated graphene due to optical interference effect¹⁸². It should be noted that ideal single layer graphene has a thickness of 0.34 nm, corresponding to the interlayer spacing of graphite¹⁸³. The large average thickness value of GO sheet is due to the presence of functional groups, structural defects, adsorbates, and trapped molecules^{105, 184}. The depth analysis in **Fig 6.2e** shows that the thickness of the first monolayer is slightly larger than that of each additional layer stacked on top. This is likely due to the presence of trapped molecules between the substrate surface and the first monolayer¹⁸⁴ and also due to the efficient stacking of layers as it will be discussed in Section 6.6.1.

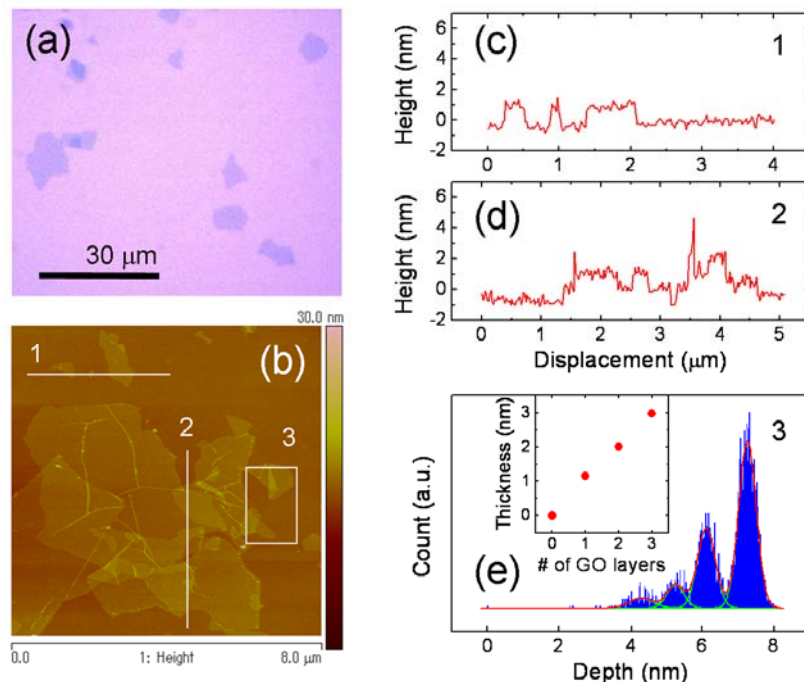


Fig 6.2 (a) Optical and (b) AFM (Nanoscope IV, Digital Instruments) images of GO flakes deposited on SiO_2/Si substrate. Presence of wrinkles and folds are readily observed in (b). The AFM image in (b) was obtained in tapping mode using a probe with a force constant of 40 N/m and tip curvature < 10 nm. (c,d) Height profiles corresponding to lines (1 and 2) shown in (b). Depth analysis of the selected area (indicated as 3) of the AFM image in (b). The four peaks, from the highest to the lowest, correspond to the substrate, monolayer, bilayer, and trilayer regions of the image. Inset shows the AFM thickness of overlapped GO flakes as a function of number of GO layers obtained from depth analysis.

6.2 Vacuum filtration of graphene oxide suspensions

Having achieved uniform suspensions of GO, we next investigated the uniform deposition of GO. We utilized the vacuum filtration method¹¹³ to deposit uniform layers of GO which is then reduced to obtain r-GO. The vacuum filtration method has been utilized to make highly uniform thin films of single-walled carbon nanotubes (SWNTs) for transparent and flexible electronics^{80, 81, 113}. In vacuum filtration, the thickness and homogeneity of the GO films on the filter membrane can be accurately controlled because

the permeation rate of the solvent is controlled by the accumulation of the GO sheets on the pores. As the suspension is passed through the ester filter, the liquid is able to pass through the pores while the GO sheets become lodged. The permeation rate of the solvent is controlled by the accumulation of the GO sheets on the pores so that as the number of GO layers increase at a given location on the porous membrane, the rate of filtration decreases and vice versa at thinner regions. Since individual sheets of GO are sufficiently larger than the pore dimension, growth occurs by creating a uniform continuous thin film of a single layer first and then by building additional layers on top. Thus, the process is self-regulating and allows reasonably good nano-scale control over the film thickness.

The GO suspension obtained was vacuum-filtrated through a mixed cellulose ester (MCE) membrane (Millipore) with 25 nm pores. Controllable deposition of uniform layers was achieved by either varying the filtration volume or the concentration of GO in the suspension. Doubling the concentration has the same effect as doubling the filtration volume. The term effective filtration volume (V_{eff}) used in the following Sections and in the next Chapter refer to the volume of 0.33 mg/L suspension required to achieve the mass deposited by suspension of other concentrations. The filtered GO thin films (shown in **Fig 6.3a**) can be transferred onto a variety of substrates such as glass, SiO₂/Si, Si, PET, ITO and metal films. Transfer can be achieved by placing the membrane with the film side down onto a substrate and dissolving the membrane with acetone, leaving behind a uniform GO thin film. The yield of the transfer process is nearly 100%, independent of the substrate, indicating that van der Waals's interactions give rise to sufficiently strong cohesive forces within the film and also between the GO flakes and the substrate. Indeed, the as-deposited thin films of GO are able to withstand typical lithographic processes (rinsing, blowing with dry nitrogen and deposition of electrodes) without any evidence of delamination. The transparent GO thin films on rigid and flexible substrates (glass, plastic) are shown in **Fig 6.3b and c**.



Fig 6.3 Photographs of GO thin films on (a) filtration membrane, (b) glass, and (c) flexible plastic substrate.

AFM analysis of deposited GO thin films indicates that the thinnest films consist of nearly one monolayer of GO. During filtration process, GO sheets from several nearby pores can overlap, giving rise to regions consisting of 3-5 layers among single monolayers. Optical micrograph in **Fig 6.4a** shows presence of such thicker regions appearing darker in color. A network of monolayer GO sheets obtained with effective filtration volume of 20 mL is shown in **Fig 6.4b**. The AFM image and the corresponding height profile (**Fig 6.4c**) shows that GO sheets are wrinkled or folded giving rise to surface roughness of the film. Thicker and more absorbing thin films were obtained for V_{eff} of 80 mL (**Fig 6.4d**). The thickness of the 80 mL thin films were found to be between 3 to 4 nm corresponding to 3 to 5 layers of GO (**Fig 6.4e and f**).

Scanning electron microscopy (SEM) images of r-GO thin films on SiO_2/Si substrate at four different V_{eff} are shown in **Fig 6.5a-d**. The lighter regions in the SEM images represent either single layer GO or voids between the GO sheets¹⁶⁷. It can be seen that the fraction of voids decreases with filtration volume. As the filtration volume was increased, films began to develop high density of wrinkles, ripples, and folds as shown in **Fig 6.5e and f**. As the film thickness increased, surface roughness also increased (**Fig 6.5g inset**).

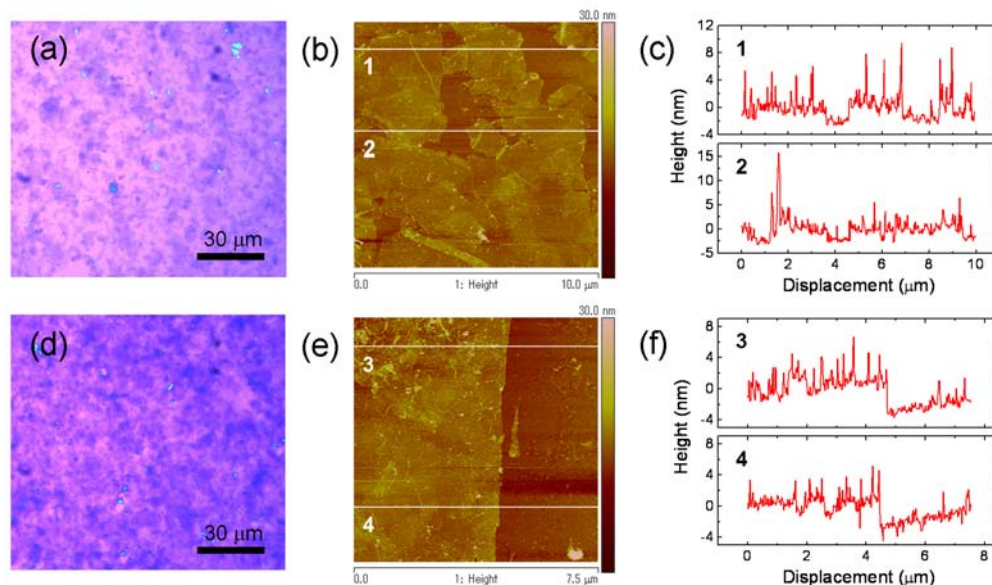


Fig 6.4 (a,d) Optical and (b,e) AFM images of (a,b) 20 mL and (d,e) 80 mL r-GO thin films. Height profiles of (c) 20 and (f) 80 mL films along the lines of the height images in (b) and (e), respectively.

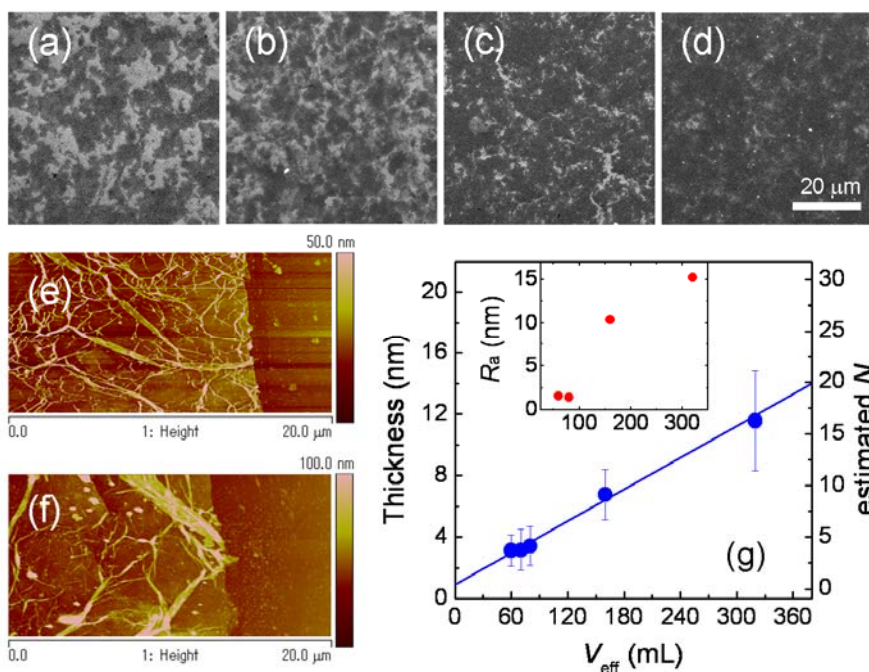


Fig 6.5 (a,-d) SEM images of r-GO thin films with different filtration volumes: (a) 20 mL (b) 30 mL, (c) 50 mL, (d) 70 mL. The scale bar corresponds to 20 μm . AFM images of (e) 160 and (f) 320 mL.

mL films at scratch edges showing surface features. (g) Film thickness as a function of effective filtration volume, V_{eff} . Estimated number of GO layers based on the results of Jung *et al.*¹⁸⁴ is shown as the right Y-axis. The inset shows average roughness (R_a) as a function of V_{eff} .

6.3 Reduction of graphene oxide

GO thin films are electrically insulating and must be reduced in order to make them conducting^{14, 101, 105-107, 111, 167, 176-179, 185-187}. The reduction of GO films can be performed by exposing to hydrazine vapor at room temperature¹⁸⁷ or at slightly elevated temperatures (80 °C)^{106, 107}. Alternatively, GO can be reduced via high temperature annealing (> 550 °C)^{178, 185}. The reduction process is believed to occur by breaking the sp^3 carbon-oxygen bonds and restoring sp^2 hybridized carbon. Elimination of the sp^3 bonds leads to a higher concentration of delocalized π electrons¹⁰⁵ which results in the decrease of electrical resistivity.

The following studies focus on the reduction process via thermal treatment in UHV, Ar/H₂, and N₂ atmosphere on pristine GO thin films and those that have been previously treated with vapor of hydrazine monohydrate at 80 °C. We found that the hydrazine vapor alone is not sufficient to achieve maximum reduction while annealing alone requires relatively high temperatures (> 550 °C)¹⁸⁵. Efficient reduction of the GO thin films was generally achieved via combination of hydrazine vapor exposure and low temperature annealing treatment.

6.4 Chemical structure

Fourier transform infrared (FTIR) spectra of GO powder show peaks of various oxygen functional groups for GO prior to reduction (**Fig. 6.6**). Specifically, epoxy, hydroxyl, and carboxyl groups are readily observed, in agreement with previous reports^{188, 189}. After exposure to hydrazine vapor followed by annealing in inert condition, vibrational modes from these functional groups are no longer visible, indicating efficient reduction

(Fig 6.6).

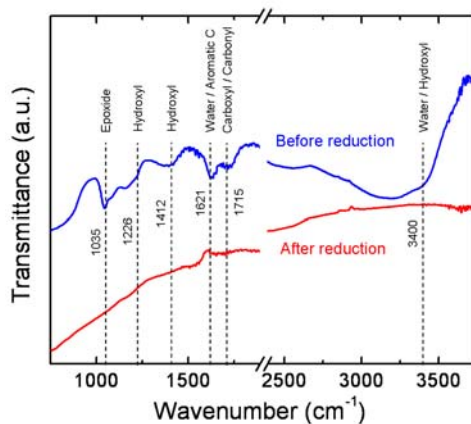


Fig 6.6 FTIR spectra of GO before and after reduction by exposure to hydrazine followed by annealing at 200 °C in vacuum. Peaks corresponding to different functional groups are indicated.

We studied the progressive loss of oxygen functional groups after each step of the reduction process by *in-situ* X-ray photoelectron spectroscopy (XPS) to monitor the evolution of reduction process. The carbon and oxygen 1s core level spectra collected on a GO thin film (~ 7 layers) after *in-situ* annealing at temperatures from 100 to 450 °C are shown in **Fig 6.7 a and b**. GO thin films were deposited on gold-coated substrate (SiO_2/Si) to allow the detection of oxygen. The fits used to extract the various carbon-carbon and carbon-oxygen bonding configurations and their concentrations are indicated in the lowermost spectra in **Fig 6.7a and b**. The C:O ratio was found to be 2.5:1 in pristine GO which is in agreement with values reported for similar oxidation processes^{190, 191}. Under the experimental conditions used here, the XPS sampling depth is lower for the O1s signal than for the C1s by 20% due to the higher binding energy of the O1s electrons¹⁹². Therefore the O1s spectra are slightly more surface specific. This difference becomes more dramatic with increasing thickness of GO films.

The C1s signal of GO consists of five different chemically shifted components which can be deconvoluted into: C=C/C–C in aromatic rings (284.6 eV); C–O (286.1 eV);

C=O (287.5 eV); C=O(-O) (289.2 eV); and $\pi - \pi^*$ satellite peak (290.6 eV) (**Fig 6.7a**). These assignments are in agreement with previous works^{190, 193}. We fitted the C1s peak component related to sp^2 C-C bonding with Doniach-Sunjic line shape while minimizing the asymmetry to isolate the C-C sp^2 fraction from the C-C sp^3 (binding energies in range 285.5 - 286.5 eV (Ref. ¹⁹³)) bonding amount. This allowed us to monitor the evolution of carbon sp^2 bonding with annealing treatment. We found that a maximum carbon sp^2 fraction of $\sim 80\%$ can be obtained with annealing treatment up to 1100 °C (see below).

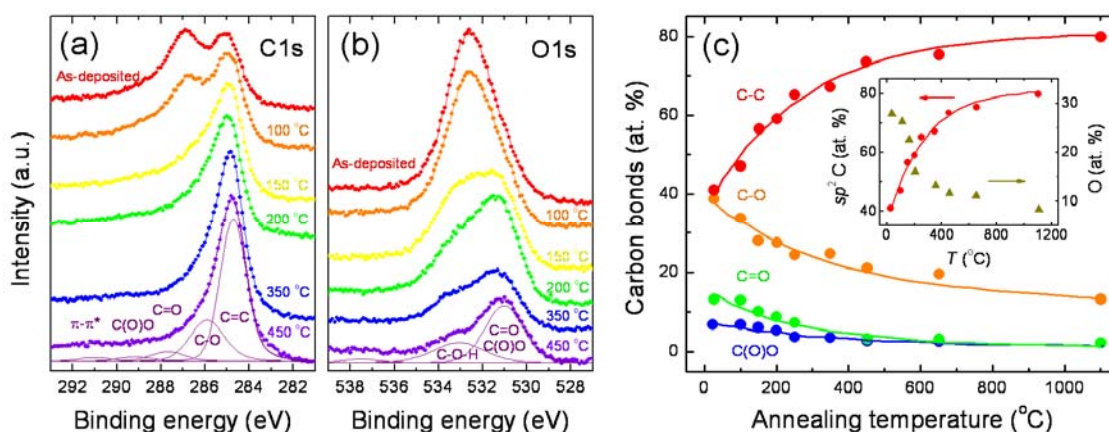


Fig 6.7 (a) C1s and (b) O1s XPS spectra ($h\nu=1253.6$ eV) collected on ~ 7 layered GO deposited on Au (10 nm)/SiO₂ (300 nm)/Si and annealed in UHV at the indicated temperatures for 15 min. The spectra were fitted by Doniach-Sunjic function after subtracting Shirley background. The different components related to various chemical shifts of carbon and oxygen bonds are indicated. (c) The atomic percentages of different carbon bonds identified by XPS as a function of annealing temperature. The solid lines are fits to each data set. The inset shows the sp^2 carbon and oxygen concentration as a function of the annealing temperature.

The spectra in **Fig 6.7a and b** indicate that a large fraction of oxygen atoms form single bonds with the carbon atoms in the basal plane of GO. The C-O bonds (38.7 at. % of carbon atoms in pristine GO) come from epoxy and hydroxyl groups in the basal plane. Based on the XPS results, the GO synthesis method that we utilized (which includes

peracid (KMnO_4) as the oxidant), and Molecular Dynamic (MD) simulations^{168, 169}, we expect that ~ 20 % more epoxy groups are present as compared to hydroxyl groups. Our observations indicate that majority of oxygen species consist of C–O and more oxidized species such as C=O and C=O (–O) are present in lesser amounts. The C=O (13 at. % in GO) compounds mainly arise from single ketones and quinines¹⁶⁸ which decorate the edges of GO sheets but may also be bound to the basal plane as carbonyl groups^{172, 184}. The C(O)OH species (6.7 at. % in GO) are present primarily at the edges of GO sheets^{171, 173, 194}.

The evolution of carbon bonds in GO thin films monitored with XPS as a function of annealing temperature in UHV is summarized in **Fig 6.7c**. The evolution of physisorbed species (H_2O and CO_2) after 15 min of annealing at 100 °C observed by XPS was also confirmed by mass spectroscopy during annealing. The loss of all oxygen groups occurs with temperature, exhibiting higher rate between 100 - 250 °C (**Fig 6.7c**). The C–O component continues to decrease up to 450 °C. The C/O atomic ratio at 450 °C is 7.9, in agreement with values reported in the literature for UHV annealing¹⁹¹. Initially, the O1s peak appears at binding energy of 532.6 eV, in accordance with Ref. ¹⁹⁰ and contains contributions from C=O (531.2eV), C=O(–O) (531.2eV) and C–O (533eV). During annealing, the two components related to C=O and C–O are clearly visible. The fact that we observed C=O peak with higher intensity than the C–O component at annealing temperatures from 200 - 450 °C is attributed to the fact that a portion of the O1s peak incorporates a contribution from trapped CO_2 molecules which are present as by-products of the reduction process. The O1s peak detected for thinner films (1 - 2 layers) annealed between 200 - 450 °C did not show this additional contribution from trapped CO_2 .

The fraction of sp^2 carbon and the oxygen concentration with annealing temperature are shown in the inset of **Fig 6.7c**. It can be seen that the amount of carbon sp^2 bonding concentration increases with evolution of oxygen, reaching a maximum value of ~ 80 % at an oxygen content of ~ 8 at. %. This suggests that the remaining oxygen is responsible for ~ 20 % sp^3 bonding. Thus, annealing up to 1100 °C is not sufficient to completely remove

the oxygen from GO, leaving it partially oxidized and therefore only partially reduced.

6.5 Raman spectroscopy

Raman spectroscopy is a non-destructive technique widely used for investigating structural information of carbon-based materials¹⁹⁵. The main features in the Raman spectra of carbon-based materials are the G and D peaks and their overtones. The first-order G and D peaks appear at around 1580 and 1350 cm^{-1} , respectively. Both peaks arise from vibrations of sp^2 hybridized carbon atoms. The G peak corresponds to optical E_{2g} phonons at the Brillouin zone center and indicates the presence of graphitic carbon¹⁹⁵. The D peak is due to the breathing-like mode of carbon rings which requires a defect for its activation. The D peak intensity therefore provides a measure for the degree of disorder in graphene¹⁹⁵. The overtone of D peak, called the 2D peak, appears around 2680 cm^{-1} and its shift has been correlated with the number graphene layers (N) (Ref. ¹⁹⁶). The 2D peak is due to double resonance process resulting in two phonons with opposite momentum. The 2D peak is present even in the absence of any defects.

In this study, we utilized Raman spectroscopy for two main purposes: to study the structural disorder of as-prepared and reduced GO and to verify thickness and uniformity of vacuum-filtrated graphene thin films.

6.5.1 Individual graphene sheets and thin films

Raman spectra of individual monolayer of GO deposited on SiO_2/Si substrate were obtained before and after reduction treatment as shown in **Fig 6.8**. The general features of the spectra are largely unchanged with reduction treatment. The prominent D peak with intensity comparable to G peak is indicative of significant disorder even after reduction. A weak and broad 2D peak is another indication of disorder¹⁹⁷. It should be noted that for mechanically exfoliated graphene, the 2D peak is sharp with FWHM (full width at half maximum) value on the order of 30 cm^{-1} and has higher intensity compared to the G peak.

A defect activated peak called D+D' is also readily seen near 2950 cm^{-1} (Ref. ¹¹²). Nevertheless, the positions of 2D peak for both spectra are consistent with that of a monolayer of mechanically exfoliated graphene¹⁹⁶.

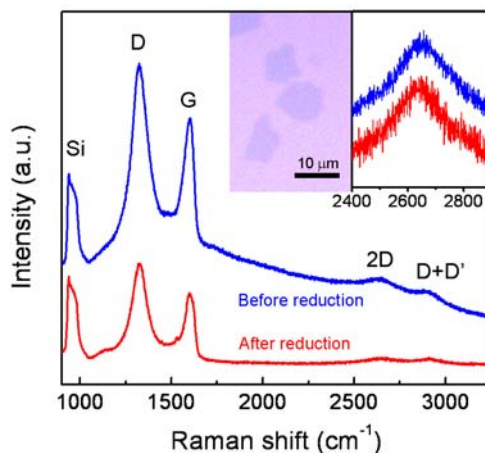


Fig 6.8 Raman spectra of an individual monolayer of GO before and after reduction by exposure to hydrazine vapor and annealing at $200\text{ }^{\circ}\text{C}$ in vacuum. Inset shows optical image of individual flakes of GO and expanded plot of the 2D regions with background and D+D' peak subtracted.

During the thermal reduction process, GO is expected to undergo structural changes due to the loss of oxygen. The carbon atoms in the basal plane may also rearrange during annealing due to the available thermal energy. Such structural changes were investigated by Raman spectroscopy via measurements taken after each annealing step. The Raman spectra of as-prepared and reduced GO thin films consisting of ~ 7 layers are shown in **Fig 6.9**. Results from two types of reduction treatments (annealing at $1100\text{ }^{\circ}\text{C}$ and exposure to hydrazine vapor followed by annealing at $200\text{ }^{\circ}\text{C}$) are plotted. The spectra display the carbon D and G band peaks at ~ 1330 and $\sim 1600\text{ cm}^{-1}$, respectively. The position of the G peak is consistent with that of pristine and hydrazine vapor reduced GO¹⁰⁷. It is well documented¹⁹⁸⁻²⁰¹ that the area ratio of the D and G peaks is a measure of the size of sp^2 ring clusters in a network of sp^3 and sp^2 bonded carbon. Using the empirical

Tuinstra-Koenig relation¹⁹⁹ to obtain the lateral dimension of sp^2 ring clusters, an average graphitic domain size in pristine GO was calculated to be ~ 2.5 nm. For chemical reduction with hydrazine vapor and thermal annealing up to 500 °C, the change in the D to G peak area ratio was found to be negligible, in accordance with our previous work¹⁰⁷. After annealing at 1100 °C (**Fig 6.9**), a slight decrease in the FWHM of D peak was observed, resulting in increase of calculated sp^2 cluster size to ~ 2.8 nm. This observation suggests that even when the sp^2 carbon-carbon bonds are restored by de-oxidation, their spatial distribution in the honeycomb graphene lattice does not generate an expansion of a continuous sp^2 phase. This may be due to the fact that the sp^2 sites are isolated in a way that there is a vacancy in the lattice for every pair of aromatic rings restored as phenol groups. In addition, dangling sp^3 bonds may be also generated from detachment of CO groups, especially at high temperatures (~ 1100 °C). It is well known for graphite that such dangling bonds are difficult to anneal out even at temperatures in excess of 1000 °C^{202, 203}.

The D to G ratios and the corresponding sp^2 cluster size are plotted as a function of annealing temperature as summarized in the inset of **Fig 6.9**. The data from other researchers are also plotted. Our values are in good agreement with the measurements of Yang *et al.*¹⁹¹ and Jung *et al.*¹¹¹ but differ from those of Gomez-Navarro *et al.*¹⁰⁷ and Tung *et al.*¹⁷⁹ who report slightly lower D to G ratios and therefore larger sp^2 cluster sizes (~ 6 nm). It should be noted that the electrical properties of the GO flakes with large sp^2 cluster size are remarkable, with mobility values as high as $300 \text{ cm}^2/\text{V}\cdot\text{s}$ ^{107, 179}. This suggests that large sp^2 domain sizes that are minimally interrupted by sp^3 bonds are essential for approaching electrical properties of intrinsic graphene with r-GO. It should be noted that the origin of the large sp^2 graphitic domain sizes for non-reduced GO in Ref. ^{107, 179} is unclear but may point to incomplete oxidation of graphite. However, this is not supported by their XPS data¹⁷⁹ in which oxygen content of 7 - 8 % is reported, comparable to our results.

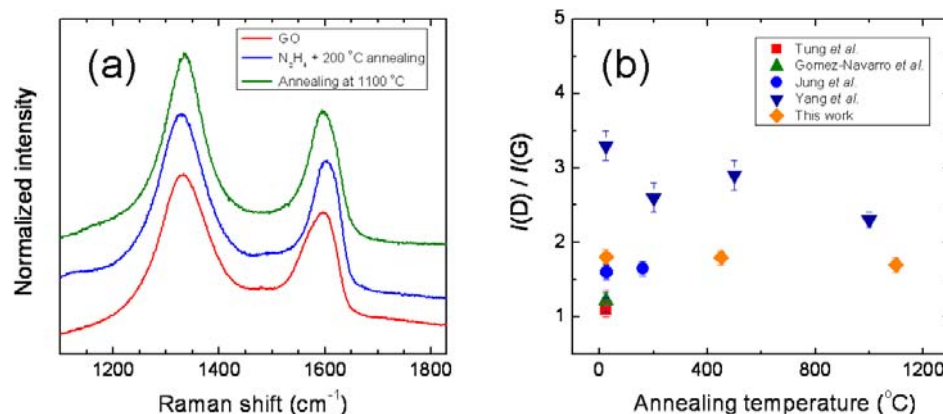


Fig 6.9 (a) Raman spectra of ~ 7 layered GO thin films recorded with $\lambda = 633$ nm laser with a lateral beam dimension of ~ 2 μm . Spectra of pristine GO, GO reduced by exposure to hydrazine vapor at 80 °C followed by annealing at 200 °C and GO reduced only by annealing at 1100 °C in Ar/H₂ are shown. (b) The D to G ratio ($I(D)/I(G)$) as a function of annealing temperature. The values reported in the literatures are also shown.

6.5.2 Raman mapping

In order to verify the thickness of GO thin films measured by AFM, we obtained Raman maps of the film thickness from the 20 (1 - 2 nm) and 80 (3 - 5 nm) mL thin films by monitoring the second order zone boundary phonons peak near 2700 cm⁻¹, or 2D peak¹⁹⁶. The shift in this peak has been correlated with the number of layers in graphene¹⁹⁶. Although the peak intensity is low, careful data collection and analysis of the spectra allowed us to monitor the shift of 2D peak. Raman spectra from a thin ($N \sim 1$) and thick ($N > 5$) regions of a film are shown in **Fig 6.10a and b**. The 2D peak obtained from a monolayer region has single component whereas a distinct relative shift and splitting of the peak can be observed for a thicker region in agreement with the previous report¹⁹⁶. The 2D peak shift of the two spectra ($N \sim 1$ and $N > 5$) was found to be approximately 40 cm⁻¹ wavenumbers (**Fig 6.10b**). In order to obtain a spatial map of N , Raman spectra were obtained at every 1 μm spacing in X and Y direction over a spatial range of 15 $\mu\text{m} \times 12 \mu\text{m}$. Based on the values reported in Ref. ¹⁹⁶ for mono- and multi-layer graphene, we assigned N

for each spectra using the lower and upper bounds of 2D peak position summarized in **Table 6.1**. The Raman maps obtained thus for the 20 and 80 mL reduced GO thin films are shown in **Fig 6.10c and d**. The Raman maps are consistent with the AFM data in that 20 and 80 mL films consist of 1 - 2 and 3 - 5 layers, respectively.

Table 6.1 2D peak shift as a function of N used to obtain Raman map. $\text{pos}(2D)_{\min}$ and $\text{pos}(2D)_{\max}$ are the lower and upper bounds of the range used to assign N for the spectra obtained in this study.

N	$\text{pos}(2D)$ (Ref. ¹⁹⁶)	$\text{pos}(2D)_{\min}$	$\text{pos}(2D)_{\max}$
1	2640	-	2645.0
2	2650	2645.0	2657.5
3 to 5	2675	2657.5	2680.0
> 6	2685	2680	-

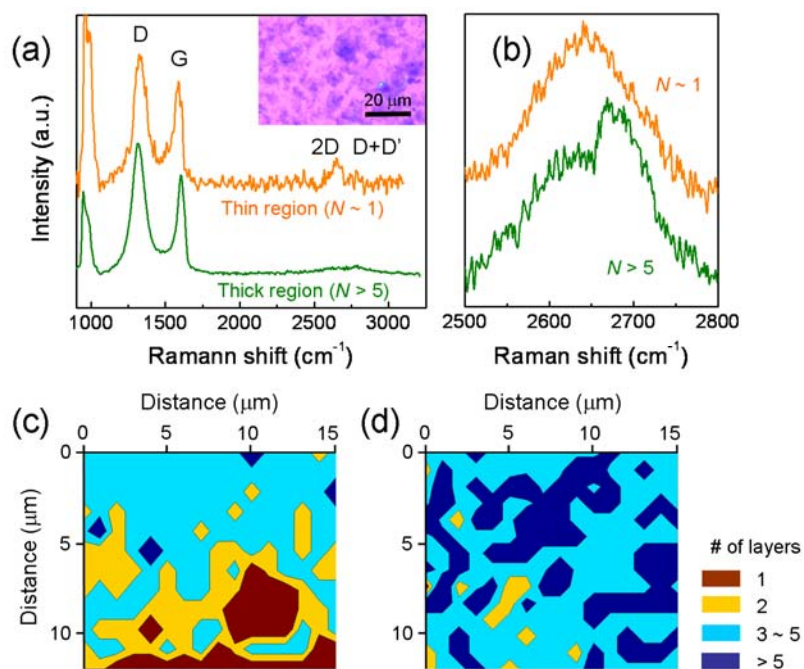


Fig 6.10 (a) Raman spectra for near single layer ($N \sim 1$) and multi-layer regions ($N > 5$) of a r-GO thin film. The inset shows optical image of a film showing thin and thick regions. (b) 2D peak

region of the plot in (a). Raman maps ($15\ \mu\text{m} \times 12\ \mu\text{m}$) for (c) 20 and (d) 80 mL r-GO thin films in which the different colors indicate different number of graphene layers as shown in the legend.

6.6 Scanning transmission electron microscopy study

The structure of GO is often simplistically assumed to be a graphene sheet bonded to oxygen in the form of carboxyl, hydroxyl or epoxy groups²⁰⁴. Several transmission electron microscopy (TEM) observations on graphene and GO have been reported,^{47, 48, 205-207} but a detailed analysis of the atomic and electronic structure for GO has been lacking. Cai *et al.*¹⁹⁴ only recently reported some structural characterization of ^{13}C GO films using nuclear magnetic resonance spectroscopy (NMR). In the following Sections, we elucidate the atomic and electronic structure of GO using composition sensitive annular dark field (ADF) imaging of single and multilayer sheets and electron energy loss spectroscopy (EELS) for measuring the fine structure of the carbon and oxygen K-edges as well as low-loss electronic excitations in a scanning transmission electron microscope (STEM). The results reveal that the structure of GO sheets is predominantly amorphous due to distortions from the high fraction of sp^3 C–O bonds. About 40 % sp^3 bonding was found for O:C ratio of 1:5 in these GO films. Our results suggest that chemical removal of oxygen, using hydrazine for example, may leave behind a highly distorted r-GO, which is likely to have substantially lower carrier mobilities than pure graphene, as has been observed in several device studies.^{106, 107, 167, 186}

STEM combined with EELS is an effective tool for measuring electronic and optical properties of materials.²⁰⁸ A simple and intimate connection between local density of the unoccupied electronic states and the core-level excitations allows direct measurements of both the energy distribution and density of states (DOS) for the levels above the Fermi energy.^{209, 210} The low loss region of EELS measures optical properties by recording electronic transitions between critical points of conduction and valence bands as well as characteristic plasmon excitations, which lead to real and imaginary parts of dielectric

function of the material.²¹¹

The following work on the STEM analysis of GO has been conducted in collaboration with Dr. Mkhoyan at Cornell University. The STEM-ADF images and EELS measurements were carried out in the Cornell VG HB-501 100 kV STEM that produces a focused electron probe of about 2 Å with about 11 mrad convergent angle and a beam current of ~ 15 pA. The microscope is equipped with a cold field emission gun, single-electron sensitive imaging detectors and a parallel electron energy loss spectrometer. ADF images were recorded using single-electron counting yttrium aluminum perovskite scintillator photomultiplier system and the dark counts were adjusted to be above zero by appropriately setting the discriminator level. The signal counts for ADF imaging were monitored and were kept below the saturation limit. Drops of the solution with GO flakes were placed on standard holey-carbon film covered copper grids and air-dried for 10 - 15 minutes. The grids were then loaded into the preparation chamber of the microscope and baked for a few hours at about 100 °C in 10^{-8} Torr vacuum in order to minimize contamination. Samples then were loaded into STEM column for observations. Before conducting any measurements, the GO samples were tested against electron-beam induced damage and possible contamination, which revealed no damage or contamination under the STEM operational conditions used during the main study.

6.6.1 Atomic structure

Composition and thickness sensitive annular dark field (ADF) images were recorded in single electron- counting mode for quantitative analysis. ADF image of several layers of GO suspended over a hole is shown in **Fig 6.11a**. While the mono, bi-, and trilayered films can be imaged, the signal from the single layer was found to be very weak as indicated by the fact that it is barely distinguishable from the hole in the middle of the image. However, a high-magnification ADF image taken from this single sheet reveals not only the sheet but also the variation of intensities within the image. **Fig 6.11b** is one such high resolution

image from a single layer GO. Strong variation of the ADF intensity in the single film suggests that the oxidation of the graphene is uniformly random throughout the sheet. Analysis of the ADF intensities from the dotted regions of **Fig 6.11c** reveals that the thicknesses of the mono-, bi-, and trilayers (relative to the intensity from the hole) scale as 1:1.5:2.0, similar to the AFM results (**Fig 6.2d**). The phenomenon can be explained by effective packing of the GO layers. The random covalent attachment of oxygen on the top and bottom surfaces creates a disordered graphene sheet and introduces roughness. The roughness of the sheets then allows effective packing of the multi-layers as schematically illustrated in **Fig 6.11d**, where oxygen atoms appear as protrusions. The observation of insensitivity of the FWHMs of the peaks in the AFM-histogram (**Fig 6.2d**) and their gradual increase in ADF-histogram (**Fig 6.11c**) with increasing number of sheets is additional confirmation of such packing. A critical observation from the AFM-depth profiles reveals that the GO sheet surface roughness is at least 0.6 nm (**Fig 6.2d**). Since all known C–O bond lengths do not exceed 0.3 nm (Ref. ²¹²) oxygen bonds alone cannot account for 0.6 nm height increase; therefore, the oxidation of graphene must be accompanied by undulations arising from lattice distortions in the original atomic structure of the graphene sheets.

Selected area electron diffraction (SAED) patterns obtained from two multi-layered regions of GO films are presented in **Fig 6.11e and f**. The pattern shown in **Fig 6.11e** is dominated by diffraction rings occurring due to the amorphous nature of the sample. It also shows the presence of some bright spots on the rings which are an indication of some crystallinity in the film. On the other hand, **Fig 6.11f** shows strong diffraction spots with six fold rotational symmetry, indicating that the electron beam is incident along [001]. The innermost diffraction spots are from (100) planes (d -spacing = 0.21 nm) while the outer from (110) planes (d -spacing = 0.12 nm). The two diffraction patterns suggest the presence of both amorphous and crystalline regions in GO sheets.

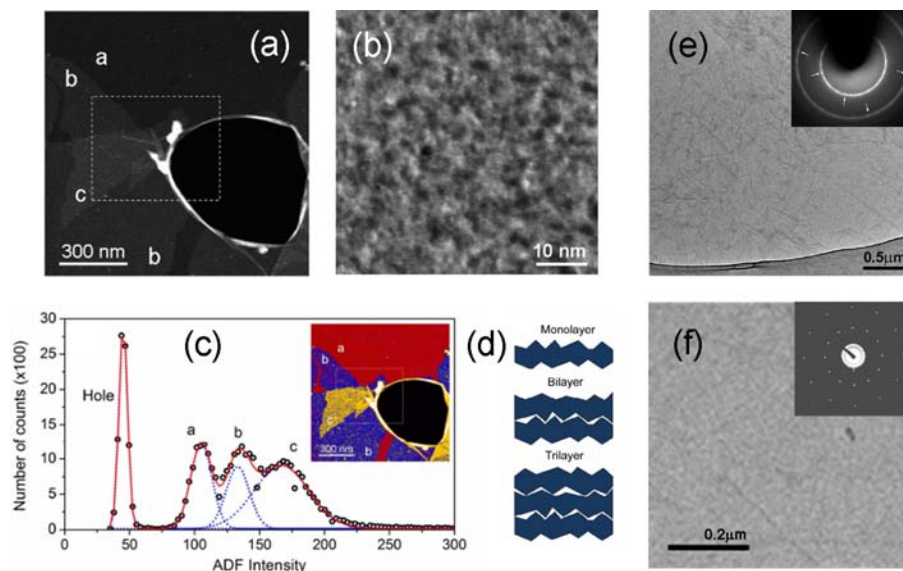


Fig 6.11 (a) STEM-ADF image of the GO films where mono-, bi- and trilayers are labeled as a, b, and c, respectively. Round opening in the middle is a hole through the single film. (b) High-magnification ADF image of monolayer GO film. (c) Histogram of the ADF intensities obtained from dotted area of (a) with distinct intensities from mono-, bi-, trilayer films and hole. The intensity from the hole corresponds to the dark current of the ADF detector. The histogram is fitted with a linear superposition of four Gaussian functions representing each peak and peaks are labeled in accordance with the number of sheets as in (a). The inset is the ADF image in (a) in colors emphasizing hole and different number of GO layers. (d) Simple drawings illustrating monolayer and possible packing of bi- and trilayers. (d,f) Conventional TEM images of multi-layered regions. The insets are the diffraction patterns from corresponding images. The arrows in (e) indicate some of the bright spots on the diffraction rings. Dark area on the top is the shadow of “beam stop” used to block the central spot.

6.6.2 Electronic structure

To study the electronic structure of GO films, core-level EELS spectra of C and O K-edges, which represent the respective $2p$ partial DOS above the Fermi level, were measured from several single GO sheets. **Fig 6.12a** shows the C K-edge recorded from GO film in **Fig 6.11a** and for comparison plotted with C K-edge spectra from amorphous

carbon (a-C) and graphite. It should be noted here that in hexagonal crystals like graphite the fine structure of the core-edges like C K-edge as well as low-loss excitations are sensitive to the orientation of the crystal relative to the incident electron beam and scattered beam collection geometry. All the core-edges and low-loss spectra from graphite and GO films presented here are recorded with electron beam oriented parallel to the c-axis and perpendicular to the sheets and with similar collection geometry.

The fine structure of the C K-edge in GO shows considerable differences relative to those in graphite and a-C.^{208, 213} However, it also indicates the presence of σ^* peak with energy close to that in graphite (peak labeled B in **Fig 6.12a**). The positions of identifiable peaks in a C K-edge in all three materials summarized in **Table 6.2** suggest that both sp^2 and sp^3 bonds are present in GO. To enhance the fine structure in C K-edge, the STEM probe function was removed from the data and the resulting spectrum is shown in **Fig 6.12c**. A spectrum of the O K-edge measured from the same sheet is presented in **Fig 6.12b** and compared with corresponding spectrum in a-SiO₂. The fine structure of O K-edge, which lacks distinct features, indicates the absence of periodicity for the oxygen atoms in the film²⁰⁸. A strong initial and an extended broader peaks are found at 538 and ~ 558 eV, respectively. Since there is no existing carbon-oxide in solid form, the O K-edge spectrum from GO sheets was compared with O K-edge of a-SiO₂, which also has an initial peak at 538 eV and an extended broad second peak at about 560 eV.²¹⁴ Strong similarities between the two are noticeable. These results are in agreement with the ADF image showing random attachment of oxygen atoms on graphene sites during oxidation. Integrated intensities of the C and O K-edges give a 1:5 ratio for number of O to C atoms.

To evaluate the amount of sp^2 and sp^3 carbon bonds in GO films, the spectrum of the C K-edge was fitted to a linear superposition of two spectra, C K-edge from graphite and a-C. After normalizing both spectra, a linear least-squares curve fitting algorithm²¹⁵ was applied to determine coefficients α_1 and α_2 of the fitting function:

$$I(E) = \alpha_1 I^g(E) + \alpha_2 I^{am}(E) \quad (6.1)$$

where $I^g(E)$ and $I^{am}(E)$ are the spectra from graphite and a-C, respectively. For the C K-edge measured from a single monolayer GO (in **Fig 6.11a**), the best fit occurs at $\alpha_1 = 0.15$ and $\alpha_2 = 0.85$, indicating that only 15 % of the carbon atoms inside the films are graphite-like, and 85 % behave a-C-like. This suggests that the atomic structure of GO films should resemble a mostly amorphous 2D sheet of carbon atoms with some of them also bonded to oxygen, rather than an ideal sheet of graphene with surface oxidation. Electron diffraction patterns shown in **Fig 6.11e and f** support this structural model. The portion of sp^3 bonds in a-C used here, based on EELS data analysis,^{208, 216, 217} is estimated to be about 45 %, which leads to an actual amount of carbon sp^3 bonds in the GO to be about 40 %. The partial amorphization of the GO can be explained by modification of the original sp^2 bonds of carbon atoms of the graphene into sp^3 bonds via bonding with oxygen and in the process moving carbon atoms from their original sites to accommodate the off-plane sp^3 bonds.

Table 6.2 Positions of the peaks in C K-edge recorded from graphite, a-C, and GO films. All energies are in eV.

	A (π^*)	B (σ^*)	C	D	E
Graphite	285.4	292.5	298.2	303.4	307.2
a-C	284.7		~ 296		
GO	284.8	292.6	296.7	302.9	

The low-loss EELS spectrum, which is a direct measure of the dielectric response of the film to the external electromagnetic excitation, was recorded from a single monolayer GO sheet and is presented in **Fig 6.12e**. When compared with corresponding spectra from graphite and a-C, significantly lower energy plasma excitations are observed. While in graphite and a-C, the peaks of bulk plasma-loss (combination of π^* and σ^* electronic

excitations) are at 27 and 24 eV, respectively, in GO films it is much lower at 19 eV. The low-energy plasma excitations of the π^* electrons in GO however occur at 5 eV, similar to that in a-C. Since the thickness of the film is only 1 - 2 nm, the origin of 19 eV main plasma resonance in GO films can be fully understood only when a full quantum mechanical description is applied. For specimens with thickness smaller than 5 nm, it is well known that surface plasma excitations are often the dominating mechanisms for energy loss.^{218, 219} But for a few atomic layers thick specimens, such a macroscopic description may not be sufficient. A very recent study by Eberlein *et al.*^{47, 220} that combined EELS measurements with first principle calculations found that the plasmon modes of pure graphene are significantly red-shifted from those found in graphite. They measured the main $\pi^* + \sigma^*$ plasma peak at 14.6 eV and a π^* peak at 4.7 eV. This suggests that in GO the plasma excitations could be related to those in graphene but with substantial blue-shift occurring due to presence of the oxygen and increased number of sp^3 bonds.

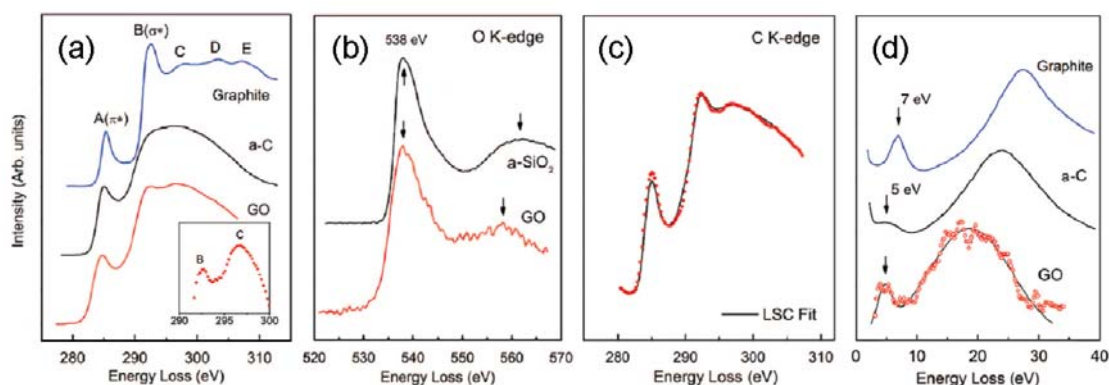


Fig 6.12 Core-loss EELS spectra of (a) C K-edge and (b) O K-edge from the GO film. Both spectra were recorded from the film labeled ‘a’ in Fig 6.11a. The spectrum of C K-edge is presented in comparison with C K-edges measured in graphite and a-C recorded using the same STEM and similar electron-optical conditions. The peaks of the fine structure are labeled A-E. The inset of (a) shows section of the spectrum from GO for better visibility of the positions of the peaks B (or σ^*) and C. The O K-edge is presented in comparison with O K-edge in a-SiO₂ also recorded using the same STEM and similar electron-optical conditions. (c) The spectrum of the C K-edge in GO sheet

after removing of STEM probe function and its best fit to Eqn 6.1. (d) Low-loss EELS spectrum showing plasmon excitations of single monolayer GO. It is presented in comparison with corresponding spectra from graphite and a-C recorded using the same STEM and similar electron-optical conditions.

6.7 Structure-dependent electrical conductivity

To elucidate the mechanisms limiting the electronic properties of r-GO, we investigated the role of residual oxygen and the sp^2 bonding fraction. The plot of conductivity as a function of sp^2 bonding fraction in reduced GO thin films is shown in **Fig 6.13**. Our experimental data along with those from 100 % sp^2 bonded materials (graphene and graphite) are plotted. Extrapolation of the experimental data suggests that it should be possible to obtain the conductivity of polycrystalline graphite ($1.25 \times 10^3 \text{ S cm}^{-1}$)¹⁸⁵ at an sp^2 bonding fraction of ~ 0.87 in reduced GO. Indeed, recent work by Tung *et al.*¹⁷⁹ indicates that achieving an sp^2 fraction of ~ 0.85 in conjunction with large sp^2 domain sizes ($\sim 6 \text{ nm}$ from Raman analysis) yields significantly enhanced electrical performance. The conductivity of single-layered graphene ($6 \times 10^3 \text{ S/cm}$)¹⁹ may be possible by further increasing the sp^2 bonding fraction to 0.95. Although the largest sp^2 bonding fraction in the r-GO reported here is substantial (~ 0.80), the carrier transport is not only determined by the amount of π electrons available but also by their spatial distribution with respect to sp^3 sites resulting from residual oxygen.

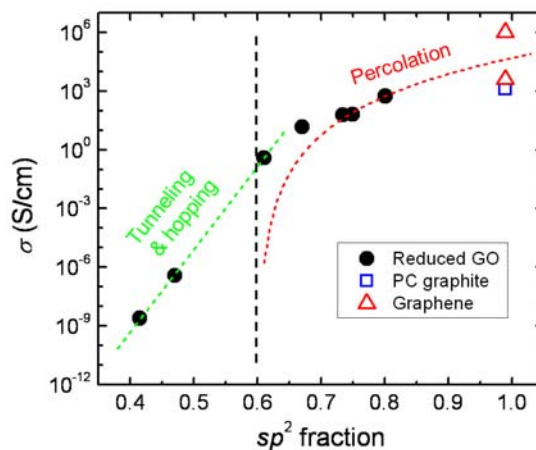


Fig 6.13 Conductivity (σ) of thermally reduced GO as a function of the sp^2 carbon fraction. The vertical dashed line indicates the percolation threshold at sp^2 fraction of ~ 0.6 . Fit to the experimental data reveals two different regimes for electrical transport. Tunneling and/or hopping (green dashed line) are likely to dominate the transport at sp^2 fractions below 0.6 while percolation amongst the sp^2 clusters dominates above the percolation threshold. The conductivity values for $\sim 100\%$ sp^2 carbon materials, namely polycrystalline (PC) graphite and graphene, are given for comparison. The two values of graphene correspond to minimum conductivity (lower triangle) and electrostatically doped on-state conductivity (upper triangle), respectively.

A structural model that captures the essential features of transport through GO at different stages of reduction is indicated by a series of sketches in **Fig 6.14**. In schematic 7a, sp^2 clusters isolated by oxygen atoms (indicated by orange dots) are shown. As the material is progressively reduced, interactions (hopping and tunneling) among the clusters increase (**Fig 6.14b**). Further reduction by removal of oxygen leads to greater connectivity among the original graphitic domains by formation of new smaller sp^2 clusters, in addition to an increase in structural defects and dangling bonds via evolution of CO and/or CO₂ species (especially from epoxy groups), indicated as pentagons in **Fig 6.14c and d**. Thus, transport in the initial stages of reduction occurs via tunneling or hopping among the sp^2 clusters, as indicated by the exponential fit of the data in **Fig 6.13** at low sp^2 fractions. At higher sp^2 concentrations, percolation ($\sigma = A(x-x_c)^\alpha$) amongst the sp^2 clusters of various shapes and

sizes dominates the transport as indicated by the curve fit in **Fig 6.13**. The percolation threshold was found experimentally to occur at sp^2 concentration of 60% which is in agreement with theoretical threshold values for conduction among two dimensional disks²²¹. The critical exponent (α) was found to be 6.53. It is well known from percolation theory that critical exponents greater than 3 are a consequence of strictly geometrical effects (such as thin resistive bottlenecks) and tunneling effects^{222, 223}. Both cases are applicable to r-GO where percolation amongst the sp^2 clusters is mitigated by structural defects such as dangling bonds or resistive bottlenecks formed by limited conduction paths due to the presence of residual oxygen.

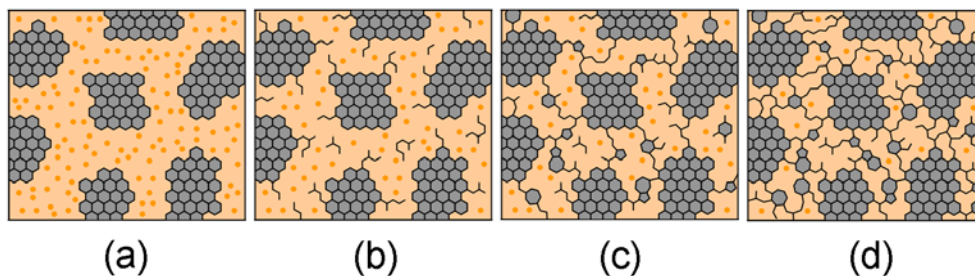


Fig 6.14 Structural model of GO at different stages of reduction by thermal annealing at: (a) room temperature, (b) ~ 100 , (c) ~ 220 , and (d) ~ 500 °C. The grey areas represent sp^2 carbon clusters, orange areas represents sp^3 carbon bonded to oxygen groups (represented by orange dots). At ~ 220 °C, the percolation among the sp^2 clusters initiates (corresponding to sp^2 fraction of ~ 0.6).

6.8 Chapter summary

In summary, fundamental structural and chemical properties of chemically derived graphene and its thin films have been investigated by using AFM, SEM, Raman spectroscopy, FTIR, XPS, STEM, and electrical measurements. Chemical characterization by XPS shows dramatic changes in the chemical state of the material with thermal reduction. For fully reduced GO, we found the oxygen content to be ~ 8 at. % with the sp^2 concentration being 80 %. The structural changes monitored by Raman spectroscopy to

probe the sp^2 graphitic domain sizes revealed little or no increase with annealing. STEM observations confirmed the Raman structural results. By monitoring the electrical conductivity versus the sp^2 fraction, we demonstrated that the presence of residual oxygen (~ 8 at. %) significantly hampers the carrier transport among the graphitic domains.

Electron energy loss spectroscopy (EELS) combined with STEM analysis and AFM-depth profiling shows that GO sheets have substantially different DOS and resonance electron plasma excitation energy than those in graphene and a-C. It also indicates that oxygen atoms attach to graphene sites randomly and convert sp^2 carbon bonds in graphene to sp^3 bonds. While the structural modifications of graphene are dependent on the oxidation level, the results show that a ratio of 1:5 oxygen to carbon atoms is sufficient to induce 40 % of sp^3 carbon bonding. As a consequence, the atomic structure of oxidized graphene is highly distorted, resembling a semi-amorphous solid carbon oxide with undulations resulting in a surface roughness of about 0.6 nm. Our results provide new insight into the structure of GO and indicate that in addition to the removal of oxygen, structural ordering of the remaining graphene sheets is necessary if high mobilities from reduced graphene oxide devices are to be achieved.

Chapter 7

Opto-electronic properties of chemically derived graphene thin films

Graphene is an interesting example of how a nano-scale material can possess extraordinary properties that are substantially different from its bulk counterpart. Electric field dependent transport, a unique signature of single and few layered graphene, has attracted vast amount of interest due to potential applications in electronic devices⁵. Field effects in graphene arise from its semiconductor-like electronic structure where its valence and conduction bands meet with vanishing density of states³⁷. In contrast, bulk graphite is a

semi-metal where overlap of bands gives rise to finite density of states at the Fermi level. The electronic band structure of multi-layered graphene evolves with the number of layers (N) due to breaking of degeneracy, resulting in overlap of valence and conduction bands. Calculations show that the degree of overlap becomes comparable to that of graphite when the number of layers is greater than ~ 10 (Ref. ⁵⁵). The ability to isolate single or few layers of graphite is therefore essential in exploring and exploiting the unique electronic properties of graphene.

One potential route to obtaining a single sheet of graphene is chemical exfoliation via formation of graphite oxide¹⁴ as described in detail in Chapter 6. The advantage of this method is that highly efficient exfoliation of graphite oxide into individual sheets in solution can be achieved. This is in contrast to micromechanical cleavage of graphite via the Scotch tape method⁵, in which the yield of monolayer graphene is too low for technological applications. In Chapter 6, we showed that ultra thin films graphene oxide (GO) can be deposited from solution with reasonably good control over the number of layers using the vacuum filtration method¹⁶⁷. Subsequent reduction of GO partially redeems the electrical conductivity of graphene sheets leading to transparent and semiconducting thin films. These reduced GO (r-GO) thin films exhibit an ambipolar electric field effect, reminiscent of what is typically observed in graphene¹⁰⁷. In this Chapter, we report the opto-electronic properties of r-GO thin films as a function of film thickness, reduction and doping. Further, we discuss the transport properties of r-GO thin films based on temperature dependent studies.

7.1 Optical transmittance and electrical resistivity

In Chapter 6, we have shown that a large fraction (~ 0.4) of carbon in GO is sp^3 hybridized due to attachment of functional groups. Since conjugation is disrupted by the sp^3 hybridized carbon, GO is electrically insulating. Reduction of GO redeems the conjugation and therefore renders GO electrically conducting. Here, we achieved the

reduction of GO by two different routes. One is the two-step reduction by exposure to dimethylhydrazine (DMH) vapor followed by annealing (in nitrogen or vacuum) at 200 °C and the other is pyrolysis at high temperature (~ 1100 °C)^{178, 185}.

Reduction of GO thin films with DMH was conducted by placing the samples in a loosely sealed petri dish which encased a smaller petri dish containing 1 vol. % aqueous solution of DMH. The petri dishes were heated to 80 °C on a hot plate thereby creating a saturated vapor of DMH solution within the petri dish in which the samples were placed. The heater was turned off after 24 hours and the samples were taken out of the petri dish and allowed to dry in air for at least 1 hour. Further reduction was achieved by annealing the films (in nitrogen or vacuum) for 5 hours at 200 °C. Pyrolysis of GO films was conducted in a quartz tube furnace with constant flow of Ar/H₂ (9:1). The furnace temperature was increased at a rate of ~ 15 °C/min, held at 1100 °C for 15 min, and slowly lowered to room temperature.

We have found that by controlling the amount of GO on the substrate (*i.e.* the film thickness) and degree of reduction, it is possible to tune the opto-electronic properties of the thin films. **Fig 7.1** shows the sheet resistance (R_s) and transmittance at $\lambda = 550$ nm as a function of effective filtration volume (V_{eff}) for different reduction treatment. It can be seen from **Fig 7.1a** that the sheet resistance of the DMH-treated GO thin films is nearly independent of V_{eff} below 300 mL. However, annealing at 200 °C in nitrogen (or vacuum) leads to a dramatic reduction in the sheet resistance. The saturation of sheet resistance above V_{eff} of 80 – 100 mL in **Fig 7.1a** is likely due to the fact that at this condition, a continuous thin film without voids is achieved. The reduction process may be effective only for top few layers (1 \sim 5), in which case only those layers that are reduced contribute to electrical conduction. Increasing film thickness does not lead to reduction in sheet resistance because efficient transport only occurs through top few layers. The GO thin films that were annealed at 1100 °C typically had sheet resistance values one to two orders of magnitude smaller than those of films reduced at relatively low temperatures (< 200 °C).

These results are consistent with the results presented in Chapter 6, which indicated that efficient reduction of GO occurs at high annealing temperatures. The corresponding transmittances at $\lambda = 550$ nm as a function of V_{eff} for GO thin films with different degree of reduction are shown in **Fig 7.1b**. It can be seen that the transmittance decreases almost linearly with filtration volumes. The general trend was that transmittance was lower for films that were well reduced and more conducting.

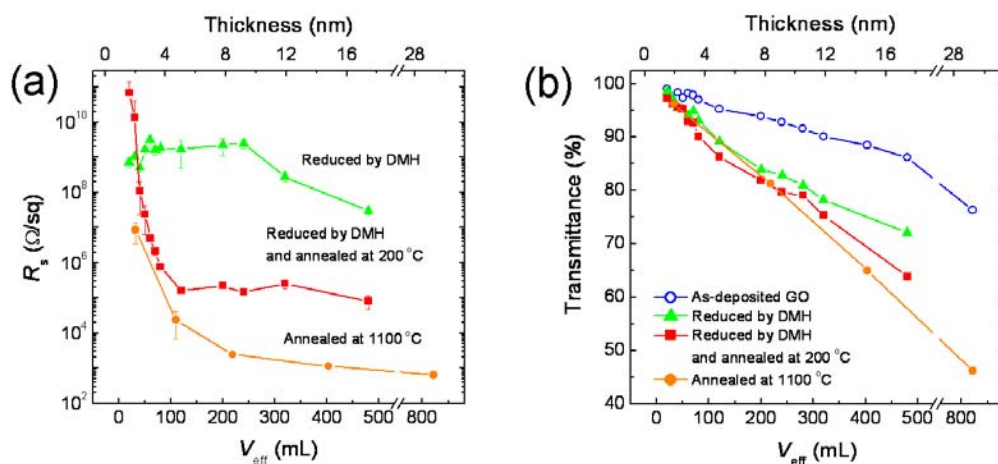


Fig 7.1 (a) Sheet resistance (R_s) and (b) transmittance at $\lambda = 550$ nm as a function of filtration volume for GO thin films with different degree of reduction. The relationship between the thickness and the filtration volume is based on the AFM measurements reported in Chapter 6 and applies only for the reduced samples. Sheet resistance for as-deposited GO is too large to be measured precisely with our measurement apparatus.

We also investigated progressive changes of optical and electrical properties of ~ 3 layer GO thin films at different stages of reduction treatments as summarized in **Fig 7.2**. The increase in conductivity (σ) of GO thin films as a function of exposure time to hydrazine (N_2H_4) vapor at 80 °C is shown in **Fig 7.2a**. The conductivity immediately increases in the initial 30 minute and reaches a saturation value (10 S/cm) after ~ 7 hours of exposure. Further reduction of hydrazine-reduced GO thin films was achieved by

subsequent annealing in Ar/H₂ as shown in **Fig 7.2b**. For comparison, the conductivities of GO thin films directly annealed in Ar/H₂ without prior exposure to hydrazine are also shown. It can be seen that an increase in conductivity up to ~ 550 S/cm can be achieved for both cases at 1100 °C. While hydrazine pre-treatment allowed efficient reduction at relatively low temperatures (< 200 °C), complete reduction was only achieved at 1100 °C. The differences between the as-deposited samples and those pre-treated with hydrazine were negligible at high annealing temperatures. The data for UHV annealed samples (**Fig 7.2b**) suggest that presence of H₂ in the annealing environment does not make significant differences on the reduction process similar to the results reported by Yang *et al.*¹⁹¹. The corresponding transmittance values (at $\lambda = 550$ nm) as a function of annealing temperature (**Fig 7.2c and d**) show that chemical reduction and thermal annealing of GO leads to a progressive decrease in transparency of the thin films, which is consistent with increased concentration of π electrons.

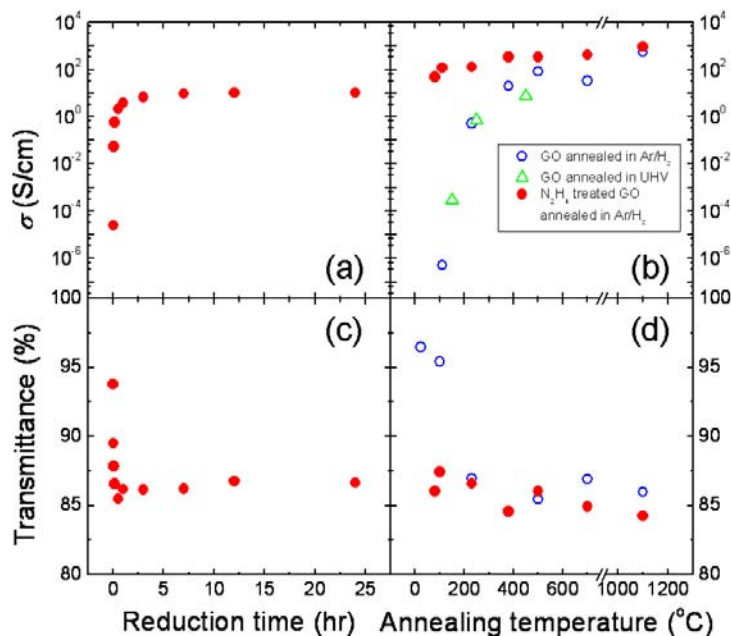


Fig 7.2 (a,b) Conductivity (σ) and (c,d) transmittance ($\lambda = 550$ nm) of ~ 3 layer GO thin film as a function of (a,c) exposure time to hydrazine monohydrate vapor at 80°C and (b,d) annealing temperatures.

To put the results of this study in context with reports in the literature, we compare our data of transmittance versus sheet resistance with several other studies^{107, 167, 178} in **Fig 7.3**. The plot indicates that the transmittance and sheet resistance decrease with reduction and the overall film thickness. The results clearly demonstrate that the opto-electronic properties of r-GO thin films reported by various groups follow similar trends. The red stars represent our values for the same film thickness annealed at increasing temperatures. Our data for films annealed at 1100°C most closely match with the results of Becerril *et al.*¹⁷⁸. Furthermore, the hydrazine monohydrate reduction route shows a larger improvement in properties compared to DMH¹⁶⁷ even without subsequent annealing. The values reported here do not approach those of intrinsic graphene, which has intrinsic sheet resistance and transmittance of $\sim 6\text{ k}\Omega/\text{sq}$ and 98% , respectively. Surprisingly, the sheet resistance and transmittance of graphene thin films produced via exfoliation of graphite in

organic solvents¹⁶⁰ also do not approach the values of intrinsic graphene

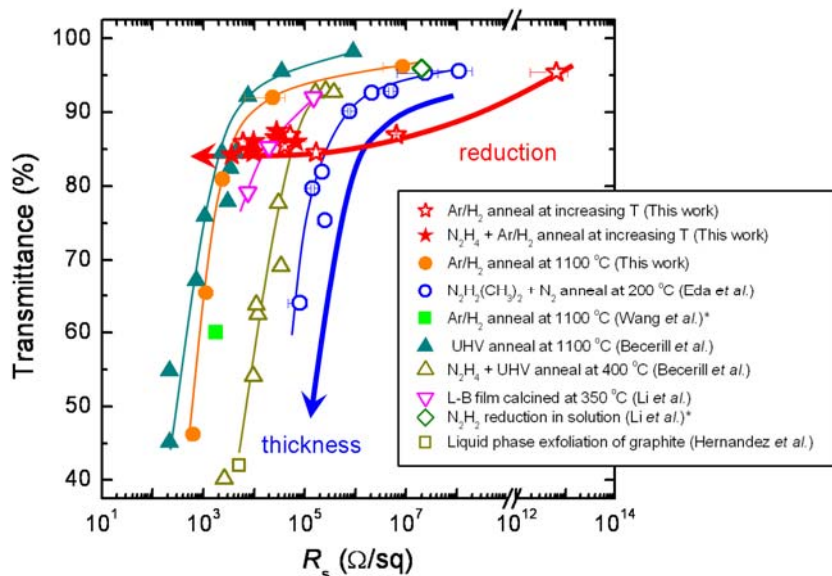


Fig 7.3 Transmittance (at $\lambda = 550$ nm) as a function of sheet resistance of r-GO thin films from various studies reported in the literature. For some literature data indicated by (*), the properties were estimated from the information provided. The red stars represent our values obtained from ~ 3 layer GO thin films annealed at increasing temperatures. The red arrow shows the general trend in the data for samples with constant thickness but with different degree of reduction. The blue arrow shows the general trend in the data for samples with the same reduction treatment but with different film thicknesses. Our data for samples annealed at high temperatures (1100 °C) agree with those of Becerill *et al.*²⁴ who employed a similar reduction process. Annealing at 1100 °C was the most effective reduction route.

7.2 Optical properties

Complex refractive indices for GO thin film before and after exposure to DMH vapor and annealing obtained from spectroscopic ellipsometry are shown in **Fig 7.4a and b**. From the extinction coefficients, it can be inferred that the optical absorption of GO thin films is dominated by $\pi - \pi^*$ transitions, which generally give rise to an absorption peak at 4.5 - 5.5 eV¹³³. The contribution of conduction electrons is minimal in the Visible/Near-UV

photon energy range. The $\pi - \pi^*$ peak intensity is relatively low for as-prepared GO thin film and increases with DMH reduction and subsequent annealing. This effect, which can be related to increased π electron concentration and structural ordering¹³³, is likely the cause for the decrease in transmittance. Annealing also considerably downshifts the peak energy for $\pi - \pi^*$ transitions, which may be attributed to the coalescence of ordered graphitic islands¹³³. The spectra of extinction coefficients obtained by ellipsometry agreed reasonably well with absorbance spectra which showed similar trends with reduction (**Fig 7.4c**).

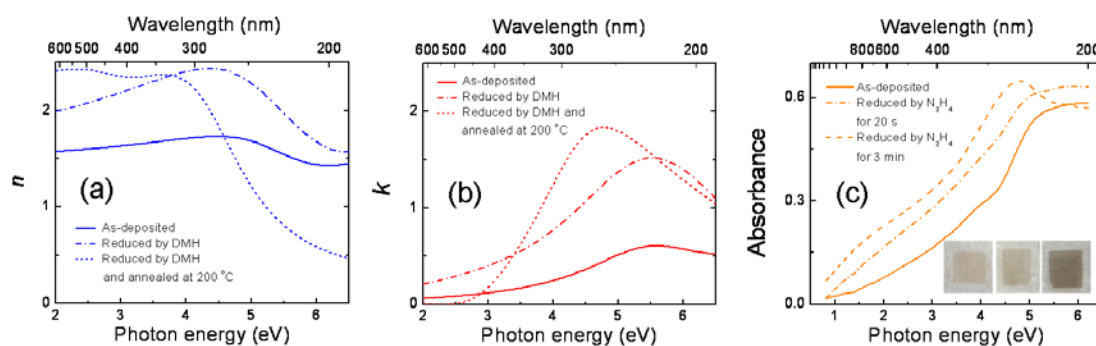


Fig 7.4 Optical constants of GO thin films determined by spectroscopic ellipsometry: (a) real and (b) imaginary part of the complex refractive index. (c) Absorbance as a function of photon energy for ~ 10 layer GO thin film at different stages of reduction. Photographs of the GO thin films are shown in the inset of (c). From the left, as-deposited, 20 second hydrazine-treated, 3 minute hydrazine-treated GO thin films are shown.

7.3 Graphene-based electrode for photovoltaic devices

The results summarized in **Fig 7.3** indicate that the thin films of r-GO can be made sufficiently conducting ($\sigma \sim 500$ S/cm) while keeping the transparency high ($> 85\%$) to be used as transparent conductors. Presently, indium tin oxide (ITO) is used as the transparent and conducting electrode in various types of photovoltaics but since it is not flexible and cannot be deposited on inexpensive substrates at low temperatures, there is a need for a

solution deposited alternative. Here, we demonstrated that r-GO thin film can be used as the transparent hole collecting electrode in organic photovoltaic (OPV). In order to improve the conductivity of the r-GO thin films for working OPV devices, we attempted to dope the thin films with Cl using thionyl chloride (SOCl_2). As we have previously demonstrated Cl doping in SWNT thin films using this method¹²⁸, SOCl_2 treatment of r-GO thin films leads to p-type doping and enhanced sheet conductance. We found that for thin films of r-GO, the sheet resistance can be reduced by a factor of up to five. The details of the doping effect are discussed in Section 7.6.

We have fabricated bulk heterojunction organic photovoltaic (OPV) devices using the P3HT-PCBM (poly (hexyl) thiophene- [6-6] phenyl- C_{61} -butyric acid methyl ester) nano-composite using reduced and SOCl_2 treated GO thin films as the hole collecting electrode. A layer of PEDOT:PSS (poly(3,4-ethylene dioxy-thiophene):poly(styrenesulfonate)) were deposited on top of the reduced and doped GO film prior to the deposition of the active layer (P3HT-PCBM) in order to facilitate hole transport. Thermally evaporated aluminum was used as the top contact. The device schematic is shown in **Fig 7.5a**. A Newport AM1.5 solar simulator operated at 100 mW/cm^2 was used to evaluate the photovoltaic characteristics. The results of the first demonstration of an OPV device with doped graphene are shown in **Fig 7.5b**. The efficiency of the devices was approximately 0.1 %. The data under illumination are far from the ideal diode characteristics and the devices are limited by the large resistance ($\sim 10^5 \Omega/\text{sq}$) of the r-GO electrode. However, since the resistance of the r-GO thin films used here is at least two orders of magnitude higher than that of graphene, the improvement in the sheet resistance of r-GO should lead to a significant improvement in the OPV device performance.

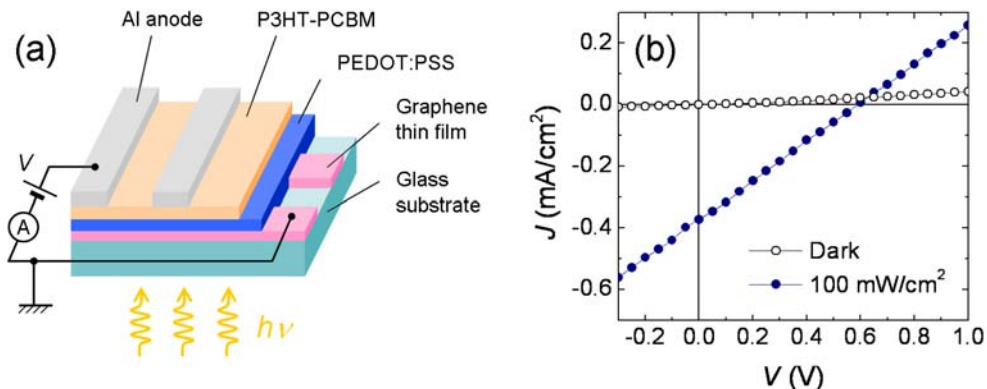


Fig 7.5 (a) Schematic of OPV with r-GO thin films as the transparent electrode. (b) I - V characteristics of OPVs under no illumination and under one sun illumination (100 mW/cm²).

7.4 Temperature-dependent electrical properties

Evolution of electronic structure with material dimensionality is an interesting subject in graphene research. Here, we investigate the evolution of electrical properties of r-GO thin films with material dimensionality, i.e. number of layers. Thin films with different number of layers were prepared by carefully adjusting the filtration volumes. Films prepared by filtrating 20 mL of GO suspension with a concentration of 0.33 mg/L (denoted as 20 mL film in the following discussion) consist of a percolating network of single-layered sheets with overlapped few-layered regions and uncovered regions, or voids. At higher filtration volumes, films become continuous and free of voids. In the following discussions, electrical properties of 20 to 80 mL films, which have average thicknesses ranging from 1.5 to 5 layers, are presented.

Fig 7.6a and b shows I - V characteristics of 20 and 80 mL films, respectively, at different temperatures. Resistivity of 20 mL film is typically several orders of magnitude higher than thicker and more continuous 80 mL film due to limited percolation paths. Moderately non-linear I - V characteristics are prominent for 20 mL film suggesting the presence of a Schottky barrier at the metal contacts¹⁰⁸ and defect mediated conduction due to trap states¹⁰⁷. This behavior of 20 mL film is similar to that of individual sheets of

r-GO^{107, 224}. In contrast, the linear I - V characteristics observed at all temperatures down to 4.2 K for the 80 mL film suggest an Ohmic interface between the film and the metal and the absence of significant trap states.

The temperature dependence of two-terminal low-bias resistance for three r-GO thin films is shown in **Fig 7.6c**. Resistance is normalized to the value at $T = 300$ K in order to make qualitative comparison amongst the films. The resistance is observed to increase with temperature up to around 40 - 100 K, above which the trend is reversed. Origin of this peculiar behavior is likely the two temperature-dependent competing variables; carrier mobility (μ) and density (n). Film conductivity (σ) can be assumed to be $en\mu$, where e is electron charge. At low temperatures ($T < 100$ K), carrier mobility decreases with increasing temperature due to electron-phonon scattering while thermal activation of carriers is suppressed. At higher temperatures ($T > 100$ K), conductivity is enhanced due to higher density of thermally activated carriers. Further complication is introduced by hopping transport, which is expected to occur within¹⁰⁷ and between the r-GO sheets. The results indicate that activated transport becomes less prominent as film thickness increases. A fit to an activated transport model yields activation values of 83.6, 78.5 and 62.4 meV for 20, 50 and 80 mL films, respectively (**Fig 7.6c inset**). The observed temperature dependence of R agrees qualitatively with that of mesoscopic graphite resistivity in which the negative temperature coefficient is only observed for very thin samples (< 20 nm)²²⁵. The temperature dependence of the r-GO thin film resistance is notably different from that of mechanically exfoliated monolayer graphene where resistivity depends weakly on temperature, often increasing with temperature by a factor of less than two²²⁶. It should also be noted that resistivity of bilayer graphene decreases moderately with temperature²²⁶.

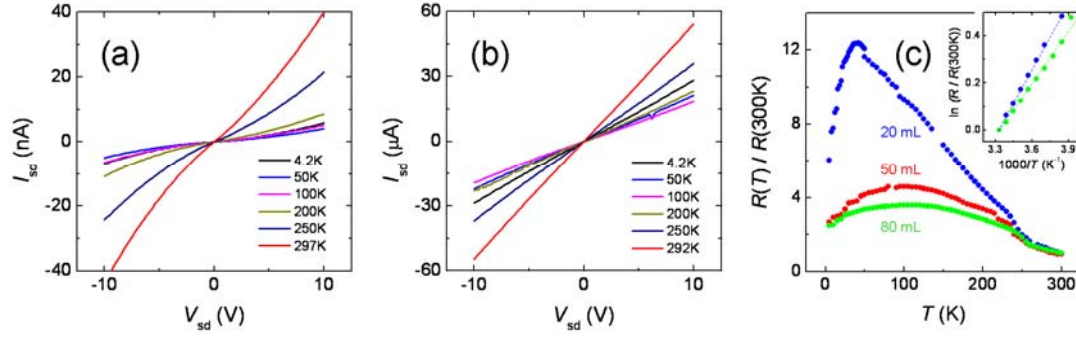


Fig 7.6 I - V characteristics of (a) 20 and (b) 80 mL r-GO thin films at various temperatures. (c) Resistance as a function of temperature ($R(T)$) for 20, 50 and 80 mL films normalized to its value at 300 K. The inset shows a linear fit to Arrhenius plot above 250 K. The data for 50 mL film are not shown in the inset for clarity.

7.5 Ambipolar field effect

In order to translate the opto-electronic properties into devices, we have fabricated TFTs with r-GO thin films. Bottom-gated TFT devices were fabricated by depositing and reducing GO thin film on Si substrates with thermally grown oxide (300 nm). Gold was deposited arbitrarily on the films as source and drain electrodes. Devices with channel lengths ranging from 20 – 210 μ m were tested in order to investigate the uniformity of the thin films. Of the numerous (> 100) devices we tested, all showed uniform transfer characteristics regardless of the channel length. The transfer characteristics at different temperatures for the 20 and 80 mL r-GO thin films are shown in **Fig 7.7c and d**. The low temperature measurements exhibit ambipolar characteristics that are similar to those obtained for graphene. The ‘V’ shape of the ambipolar graphene transfer characteristics is more pronounced for the low temperature measurements of the 20 mL TFTs. In particular, the neutrality point reflecting the density of states of graphene is clearly observed. This is remarkable since transport between the source and drain electrodes in our relatively large scale devices occurs over several graphene sheets (**Fig 7.7b**). The primary difference between the two devices is that the current in the 80 mL TFTs is higher, and the 20 mL

device exhibits sharper turn on behavior compared to the 80 mL film, which is consistent with conduction occurring primarily through one or two layers of graphene. As it will be discussed in the following Section, the TFTs at ambient conditions exhibit typical p-type behavior due to doping effects from adsorbed oxygen, comparable to what occurs in SWNTs³⁰. **Fig 7.7e** shows thin film conductance normalized to its minimum value, G_{\min} as a function of gate bias at $T = 4.2$ K for 20, 50 and 80 mL films. It is clearly seen that 20 mL film is most sensitive to electric field while the 50 and 80 mL films show minimal changes in conductance with gate voltage. This trend is likely to be caused by the screening by the bottom r-GO sheets, which prevent efficient gate control in thicker films. The results also suggest that the density of states at the neutrality point is greater for thicker films making it difficult to turn off the devices, as it is the case for mesoscopic graphite²²⁵. The on/off ratio (defined here as the ratio between the maximum to minimum conductance, G_{\max}/G_{\min}) decreases with increasing temperature for 20 mL film while only minimal changes are observed for 50 and 80 mL films as shown in **Fig 7.7f**. These results suggest possible presence of a band gap in 20 mL film, which is smaller than the thermal energy at room temperature (~ 26 meV) so that the effect is only relevant at low temperatures. A similar trend in on/off ratio has been observed for lithographically patterned graphene nano-ribbons (GNRs), which possess band gap smaller than 50 meV (Ref. ^{44, 99}).

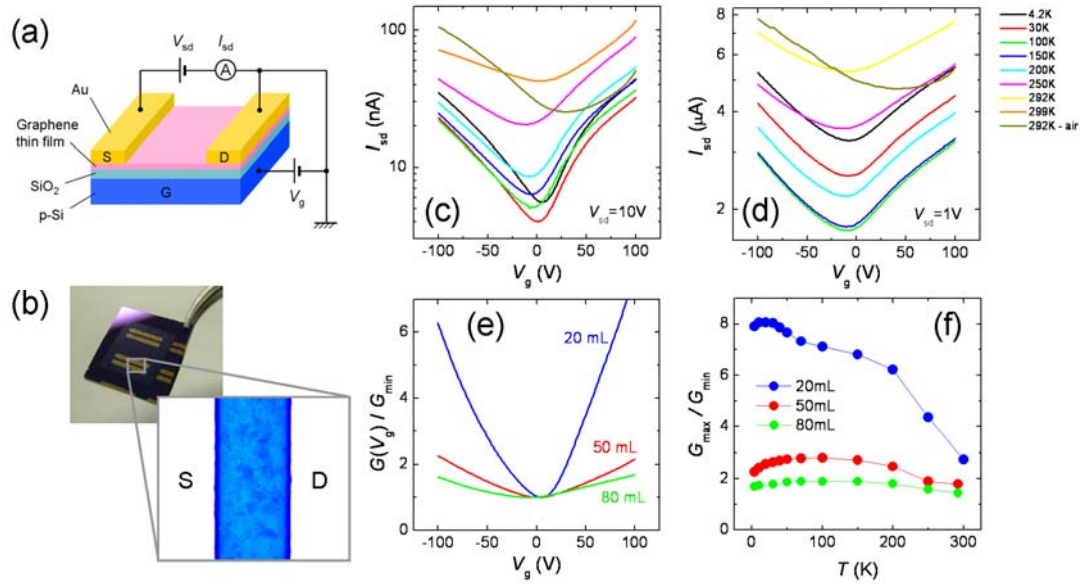


Fig 7. 7 (a) Schematic of r-GO TFT. (b) A photograph of a r-GO TFT with an optical micrograph showing the source (S) - drain (D) region of the device. The channel consists of several r-GO sheets percolating across the electrodes. The channel length is 21 μm . (c,d) Source - drain current (I_{sd}) as a function of gate voltage (V_g) for (c) 20 and (d) 80 mL films measured at different temperatures. Measurements were conducted in vacuum unless otherwise noted. (e) Conductance (G) as a function of gate voltage for 20, 50, and 80 mL r-GO thin films at $T = 4.2$ K. For comparison, the curves are normalized to its minimum value (G_{\min}) which occurs at thresholds voltage (V_{th}). (f) on/off ratio, G_{\max}/G_{\min} , as a function of temperature for 20, 50, and 80 mL r-GO thin films.

7.6 Effect of Reduction

TFTs were fabricated with ~ 3 layer GO thin films reduced at different conditions to evaluate the evolution of mobility and carrier concentration. The transfer characteristics of films annealed in UHV at three different temperatures (150, 250, and 450 $^{\circ}\text{C}$) and those reduced by exposure to hydrazine monohydrate vapor at 80 $^{\circ}\text{C}$ are shown in **Fig 7.8a**. All devices exhibited ambipolar characteristics for the measurements performed in vacuum. The main difference among the three devices is that the ‘V’ shape of the ambipolar graphene transfer characteristics is more pronounced for GO thin films reduced at 150 $^{\circ}\text{C}$

compared to films reduced at 450 °C. The on/off ratio of the film annealed at 150 °C is ~ 10 which decreases to < 2 with further reduction. These results demonstrate the semiconducting nature of mildly reduced GO thin films, which become semi-metallic at higher annealing temperatures. Field effect mobilities (μ) were extracted from the transfer characteristics by:

$$\mu = \frac{L}{WC_{ox}V_{sd}} \frac{\Delta I_{sd}}{\Delta V_g} \quad (7.1)$$

where L and W are the channel length and the width respectively, V_{sd} is the source-drain voltage, I_{sd} is the source-drain current, and V_g is the gate voltage. C_{ox} is the gate oxide capacitance and is obtained by $\epsilon_{ox}\epsilon_0/t_{ox}$ where ϵ_{ox} is the permittivity of the oxide, ϵ_0 is the permittivity of free space, and t_{ox} is the oxide thickness. $\Delta I_{sd}/\Delta V_g$ is the transconductance or the slope of the transfer curve in the linear regime. Electron and hole field effect mobilities were obtained from the electron and hole branches of the $I_{sd} - V_g$ curves. The intrinsic carrier concentration (n) was calculated assuming:

$$\sigma_{s,min} = ne(\mu_e + \mu_h) \quad (7.2)$$

where $\sigma_{s,min}$ is the minimum sheet conductance for $V_g = V_{th}$. The subscript for μ represents electron and hole carriers.

The minimum sheet conductance, carrier concentration, and field effect mobility as a function of the annealing temperature are reported in **Fig 7.8b**. The increase in carrier concentration can be attributed to the creation of π electrons via de-oxidation. The mobility of the devices increased more than three orders of magnitude with reduction level. These results are consistent with our observation that percolation paths of sp^2 carbon forms with progressive reduction process as reported in Chapter 6.

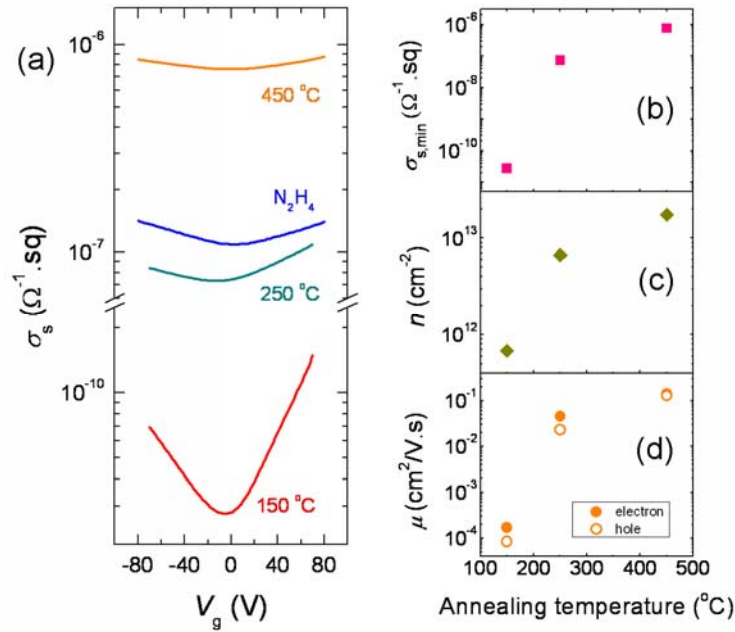


Fig 7.8 (a) Transfer characteristics of ~ 3 layer r-GO thin films annealed at three different temperatures (150, 250, and 450 °C) and those reduced by hydrazine monohydrate vapor. (b) The minimum sheet conductance ($\sigma_{s,\text{min}}$), (c) carrier concentration (n), and (d) field effect mobility (μ) as function of annealing temperature. All measurements were conducted in vacuum.

7.7 Effect of doping

Owing to the semiconducting nature of the r-GO, thin films can be doped under appropriate conditions to achieve appreciable improvements in film conductivity. **Fig 7.9a** shows typically observed unintentional doping in 50 mL film due to oxygen and water vapor in ambient conditions. As-prepared r-GO thin films typically exhibit p-type characteristics in ambient conditions and threshold voltage (V_{th}), at which the film conductivity is minimum, is a large positive value (> 60 V). We observe that removal of adsorbed water vapor by placing films in vacuum results in a shift in V_{th} (**Fig 7.9a**). It is interesting to note that removal of water vapor also leads to sharper turn-on behavior of the devices with lower G_{min} and improved G_{max} . Field effect mobility also improves by a factor of two upon this treatment. This is similar to the effect of charged impurities in

mechanically exfoliated graphene, which severely limits device mobility^{89, 94}. When r-GO thin films are placed in vacuum, ambipolar characteristics become nearly symmetric with threshold voltage close to 0 V (**Fig 7.9a**). This effect can be explained by desorption of oxygen leading to undoping of thin films. When the sample is brought back to ambient, threshold voltage immediately shifts back to large positive value (not shown for clarity). Interestingly, the field effect mobility increases with oxygen doping and decreases with de-doping, which is in contrast to doping in graphene^{89, 94}. This effect was particularly prominent for low-mobility samples. It is likely that the creation of doping levels by adsorbed oxygen facilitated defect mediated transport, thereby improving carrier mobility. The film conductivity at $V_g = 0$ V changes by a factor of two upon exposure to air in our samples.

While doping by oxygen is unintentional, we found that intentional doping which is relatively stable in vacuum can be achieved using thionyl chloride (SOCl_2). We previously showed that conductivity of single walled carbon nanotube (SWNT) thin films can be improved by a factor of about 5 by simply immersing the film in thionyl chloride for one hour¹²⁸. The same treatment on r-GO thin films leads to improvement of film conductivity by a factor of 3 - 5 due to p-type doping by the strongly electronegative chlorine²²⁷ (**Fig 7.9b**). The mechanism for Cl attachment to r-GO is likely to be comparable to the SWNT case where nucleophilic substitution of OH with Cl takes place since there are residual OH groups present on r-GO even after the reduction treatment¹⁰⁵. The transfer characteristics of the device before and after SOCl_2 treatment reveal that unlike the case of oxygen doping, the effect of Cl doping persists in vacuum as shown in **Fig 7.9c**. It can be observed that the threshold voltage remains positive even in vacuum suggesting stable attachment of Cl. Transfer characteristics at $T = 4.2$ K shows that Cl doping leads to asymmetry in ambipolar characteristics (**Fig 7.9d**). The shift of V_{th} as a function of temperature shown in **Fig 7.9e** suggests that the dopants are not activated below 200 K. Further, we observed that the hole mobility improved by a factor of 5 with Cl doping while electron mobility remained almost

unchanged. As discussed above for the case of oxygen doping, it is likely that generation of doping levels facilitates hopping conduction. Breaking the symmetry of ambipolar characteristics is important for practical device applications where unipolar performance is required.

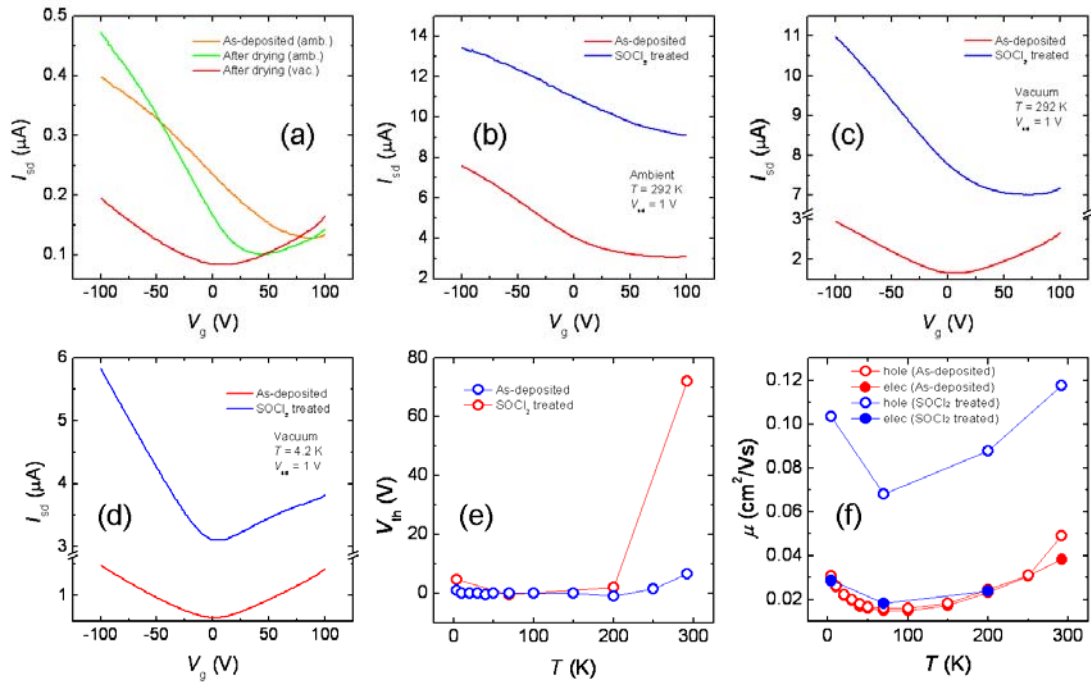


Fig 7.9 (a) Transfer characteristics of 50 mL r-GO thin film in as-prepared condition and after drying measured in ambient condition, and after drying measured in vacuum. The plot represents the transfer characteristics of the same device. Drying of the film was carried out by keeping the film in a vacuum desiccator for three weeks. (b-d) Transfer characteristics of a 30 mL r-GO thin film before and after dipping in SOCl_2 for 1 hour. Measurements were conducted in (b) ambient conditions, (c) in vacuum at room temperature, and (d) in vacuum at $T = 4.2$ K. (e) Threshold voltage and (f) field effect mobility as a function of temperature before and after SOCl_2 treatment.

7.8 Chapter summary

In summary, we have investigated the optical and electrical properties of GO thin films as a function of thickness, degree of reduction, and doping. GO thin films are optically

semi-transparent and electrically insulating but become optically absorbing and electrically conducting with chemical and thermal reduction. By carefully adjusting film thickness and reduction process, r-GO thin films can be made sufficiently conducting ($\sigma \sim 500 \text{ S/cm}$) while keeping the transparency high ($> 85 \%$). We demonstrated the use of r-GO thin films as the hole collecting electrode for organic photovoltaic devices and achieved power conversion efficiency of 0.1 %. In r-GO TFTs, electric field response was found to consistently decrease with increasing film thickness similar to the case of graphene, few layer graphene, and mesoscopic graphite. Specifically, the semi-metallic nature of the material becomes more pronounced as the film thickness increases above 3 - 5 layers. In ambient conditions, thin films consisting of 1 - 2 layers of r-GO layers are p-type semiconductors due to adsorbed oxygen and water vapor. The use of thionyl chloride leads to more stable Cl doping with appreciable improvement in film conductivity, a shift in threshold voltage, and hole mobility.

Chapter 8

Graphene-based composite thin film transistors and field emitters

Graphene-based composites are emerging as new class of materials that hold promise for various applications²²⁸. Graphene, a single sheet of graphite, possesses extraordinary electrical, thermal and mechanical properties arising from its unique structure³⁷. When incorporated into polymer^{14, 229-231} or ceramic¹⁸⁷ matrices, these properties manifest as remarkable improvements in the host material. Graphene-based polymer composites exhibit extraordinarily low electrical percolation threshold (0.1

vol. %) due to large conductivity and aspect ratio of the graphene sheets (atomic thickness and micrometer-sized lateral dimensions)^{14, 231}. The mechanical and the thermal properties of these materials rank among the best in comparison with other carbon-based composites due to strong interactions between polymer hosts and graphene sheets^{228, 230}. The highly conductive nature of graphene and ease of incorporation into polymers and ceramics has also opened up the possibility of their use as transparent conductors¹⁸⁷. In this Chapter, two potential applications of graphene-based composites are introduced. Initially, we focus on the semiconducting nature and field modulated transport properties of the graphene-based composites thin films are described. In the latter part of the Chapter, field emission properties of graphene-based composite thin films are investigated and analyzed.

8.1 Semiconducting graphene-based composite thin films

Graphene is a zero band gap semiconductor exhibiting large electric field effect⁵, allowing doping with electrons or holes via electrostatic gating. The fact that graphene does not have a band gap poses a challenge for digital applications, but its high mobility is attractive for high frequency analog electronics or spintronics^{25, 232}. The semiconducting and robust mechanical properties of reduced graphene have been exploited for macro-scale thin film electronic devices^{167, 176} and high performance resonators¹⁷⁷. Semiconducting behavior, however, has yet to be demonstrated in graphene-based composites. The compatibility of graphene with polymers and ceramics opens up a route towards realization of semiconducting composite materials from electrically passive host materials. That is, introduction of percolating graphene network within an insulating material may render it semiconducting. In the first part of this Chapter, we show that incorporation of functionalized graphene sheets (FGS) in a polystyrene (PS) matrix results in composite thin films that are semiconducting and exhibit ambipolar field effect. These composites can be deposited uniformly over large areas in the form of thin films from solution onto which devices can be fabricated without extensive lithography. The reported solution-based

approach for fabricating thin film transistors (TFTs) from FGS and PS could bring a new dimension to the potential applications of graphene-based composites.

8.1.1 Preparation

The scheme for fabricating graphene-based polymer composites proposed by Stankovich *et al.*¹⁴ utilizes the chemical versatility of graphene oxide (GO), a solution processable precursor to graphene. GO is hydrophilic and disperses mainly in aqueous media but can be chemically functionalized with isocyanate to make it soluble in organic solvents such as dimethylformamide (DMF)¹⁸⁹, commonly used to dissolve many polymers. After dissolving the functionalized GO with a polymer in a solvent, it can be reduced to form a FGS-polymer solution.

The semiconducting graphene based composite thin films were prepared using the method outlined for bulk graphene-based composites¹⁸⁹. Initially, graphite oxide was prepared using the modified Hummers method¹⁸⁰ and functionalized using phenyl isocyanate and dispersed in DMF at a concentration of 1.5 mg/mL. 25.3 mg of linear monodisperse PS (molecular weight = 2,043,000 g/mol, Scientific Polymer Products Inc.) was added to 10 mL of functionalized GO dispersion in DMF and stirred at 60 °C until completely dissolved. A solution consisting of 10 vol. % of FGS in PS was prepared. To reduce functionalized GO, dimethylhydrazine was added to the solution at a concentration of 1 vol. % with respect to the total volume of the solution and the mixture was allowed to stand for 24 hours at 80 °C. The solution obtained thus was spin-coated on degenerately doped Si substrates with 300 nm thermal oxide at 1000 to 4000 rpm to obtain uniform thin films with thickness of 14 to 30 nm. The samples were then baked at 200 °C to remove residual solvent and dimethylhydrazine. Spin-coating and baking were carried out in a glovebox to avoid coagulation of PS due to moisture. Gold source (S) and drain (D) electrodes were thermally evaporated on composite thin films for transport measurements. The Si substrate was used as the gate (G) electrode. Devices with channel lengths ranging

from 14 to 230 μm and channel width of 400 μm were tested. The transport measurements were conducted in a cryostat (ST-500, Janis) with a base pressure of 10^{-5} Torr at temperatures ranging from 4.2 and 370 K. The device structure is schematically shown in **Fig 8.1a**. The size of FGS was found to remain unchanged during the reduction and deposition processes (**Fig 8.1b and c**). The size of FGS is dependent on the size of initial graphite crystals but can be adjusted by ultrasonication of the suspension to break up the individual sheets²³³. In this study, composite thin films consisting of FGS with three different average sizes were prepared from two graphite sources (Bay Carbon Inc. and Branwell Graphite Ltd.). Due to viscous flow of polymer solution during spin-coating, most FGS were found to be lying nearly parallel to the substrate surface (**Fig 8.1c**). Some FGS were nearly exposed at the composite surface as indicated by the higher contrast against the insulating matrix in the SEM (**Fig 8.1d**).

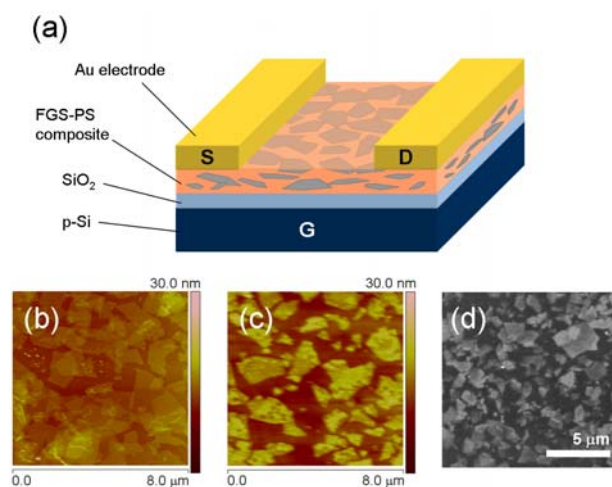


Fig 8.1 (a) Schematic of FGS-PS composite thin film field effect devices. (b) Atomic force micrograph (AFM) of (b) phenyl-isocyanate treated GO and (c) FGS-PS composite thin films. (d) Scanning electron micrograph (SEM) of typical as-deposited FGS-PS composite thin films. Contrast can be seen between conductive FGS (light) and insulating PS matrix (dark).

8.1.2 Ambipolar field effect

The composite thin films were electrically conducting with the sheet resistance being on the order of 1~10 M Ω /sq due to percolation amongst the FGS within the PS matrix. The corresponding conductivity values for the thin films ranged from 1 to 24 S/m, in agreement with the values reported for bulk composites¹⁴. Conductance modulation by bottom-gating was observed in all measured devices and showed ambipolar field effect similar to reduced GO thin film transistors^{107, 167}. Field effect mobility was generally higher for holes than for electrons by a factor of about 2~5 and was generally between 0.1 and 1 cm²/Vs in ambient conditions. Unlike reduced GO, the composite devices were weakly sensitive to unintentional ambient doping, suggesting that majority of FGS responsible for the carrier transport are embedded within the PS. The minima in the transfer characteristic curves were readily visible at threshold voltages of around +20 V which shifted to +16 V when measurements were performed in vacuum (**Fig 8.2a**). At low temperatures in vacuum, the threshold voltage (V_{th}) remained near $V_g = 0$ V and the hysteresis resulting from upward and downward sweeps of the gate voltage was found to be minimal (**Fig 8.2b**). The temperature dependent transfer characteristics in **Fig 8.2c** indicate that the on/off ratio of the devices increases with decreasing temperature, a trend that has also been observed for individual monolayer of reduced GO¹⁰⁷. The on/off ratio with temperature trend observed for FGS-PS thin films suggests that the FGS are well dispersed and remain exfoliated in the PS matrix. The I_{sd} - V_{sd} characteristics of the devices were linear even at 4.2 K, indicating negligible energy barriers at the contacts (**Fig 8.2d**).

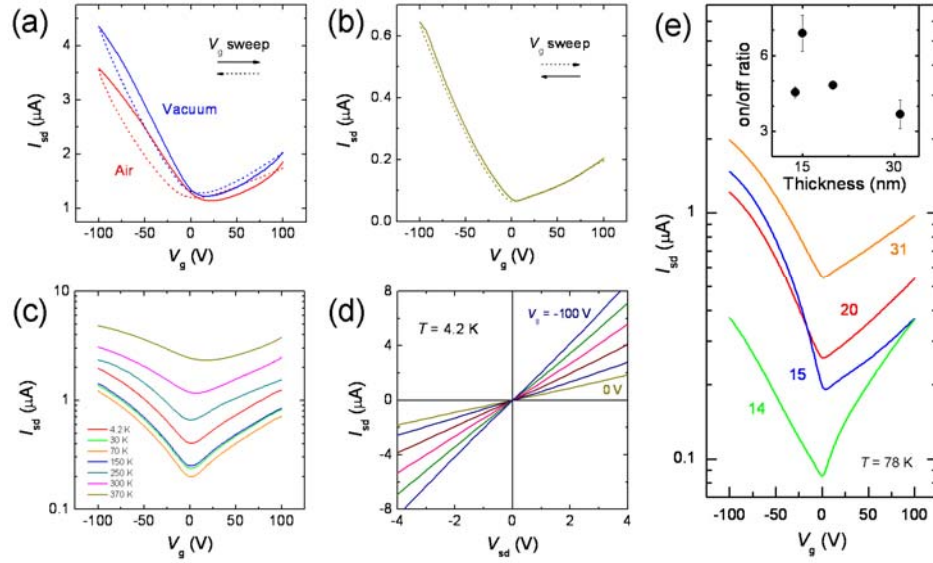


Fig 8.2 (a) Transfer characteristics of a FGS-PS composite thin film in air and vacuum. Hysteresis from different sweep directions of V_g ($V_{sd} = 1$ V) are shown. Transfer characteristics (b) at 90 K in linear scale and (c) at various temperatures in log scale ($V_{sd} = 1$ V). (d) I_{sd} - V_{sd} characteristics with different V_g measured at 4.2 K. (e) Transfer characteristics of thin films with different film thicknesses (indicated in nm) measured at 78 K. The inset shows the on/off ratio as a function of film thickness.

To study the device characteristics with film thickness, the spin-coating speed was varied. The device resistance increased with decreasing film thickness (i.e. increasing spin-coating speed during deposition) as expected. However, the qualitative features of the transfer characteristics remained largely unchanged (**Fig 8.2e**). The on/off ratio did not vary significantly with film thickness indicating that electrostatic screening effects are not critical for the studied thickness range (**Fig 8.2e inset**). These results suggest that our composite thin films consist of nearly one monolayer of graphene sheet along the thickness in the z-direction. It is also worth noting that the device properties remained consistent before and after cooling down to liquid helium temperature. Atomic force microscope (AFM) analysis revealed that the material did not crack or change its morphology upon

lowering of temperature. This observation may suggest that FGS provides structural rigidity to PS against deformation and crack propagation.

8.1.3 Temperature dependent transport

The thin film conductance as a function of temperature (from 4.2 to 370 K) was measured and shown in **Fig 8.3a**. The conductance decreased with decreasing temperature down to about 50 K and increased slightly with further lowering of temperature. Such anomalous behavior has been observed previously in graphitic flakes²²⁵ and reduced graphene oxide thin films¹⁶⁷. It is likely that at temperatures below 50 K, electron-phonon scattering limits the carrier transport. Above 250 K, the temperature dependence can be fitted with a thermal activation model, yielding an activation energy of 87 meV for transport. The FGS-PS composite is a highly disordered system as FGS contain intrinsic defects and are randomly arranged within PS. Therefore, the description of carrier transport through the composite is expected to require a combination of models. That is, there are contributions from thermal activation of carriers, tunneling through the PS matrix, and variable range hopping both within and between the FGS¹⁰⁷. The activation energy obtained above is only a rough estimation of the total energy required for thermal carrier activation and transport.

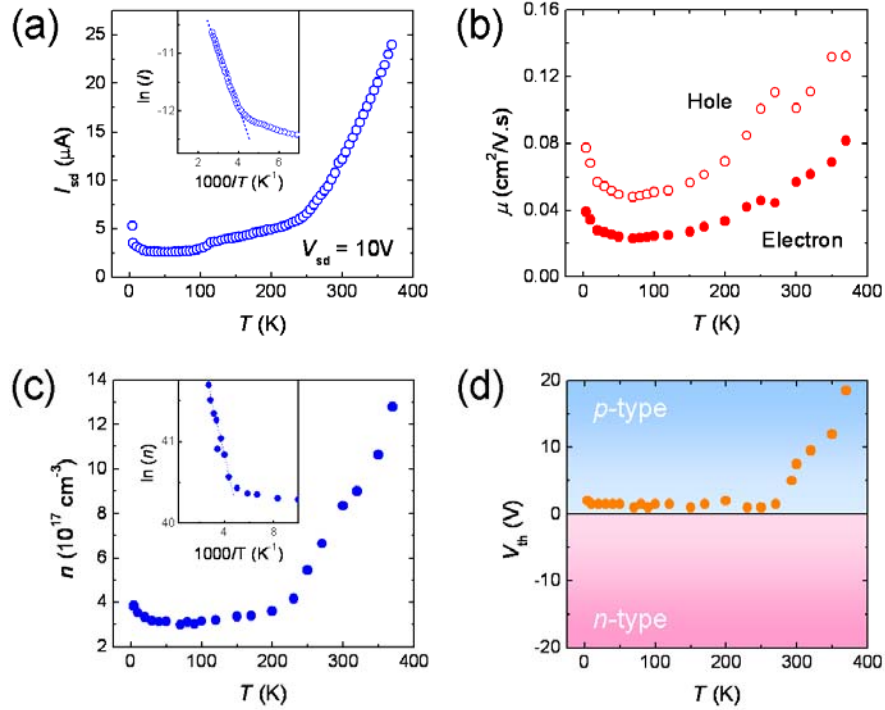


Fig 8.3 (a) Temperature dependence of source-drain current (I_{sd}) with $V_{sd} = 10$ V and floating gate. The current values were recorded for increasing temperatures from 4.2 K up to 370 K. The inset shows the corresponding Arrhenius plot. (b) The electron and hole mobilities, (c) intrinsic carrier concentration, and (d) threshold voltage as a function of temperature.

Further insight into the transport mechanism can be obtained by separating these contributions. The conductivity of the material is expressed as $\sigma = e(n_e\mu_e + n_h\mu_h)$ where e is the electron charge, n is the carrier concentration, μ is the carrier mobility and the subscripts indicate the two charge carrier types, electrons and holes. The mobility for each type of carriers can be extracted from the two branches of the transfer characteristics using $\mu = (L/WC_{ox}V_{sd})g_m$ where L and W are the channel length and the width, C_{ox} is the gate oxide capacitance, V_{sd} is the source-drain voltage, and g_m is the transconductance. Further, the intrinsic carrier concentration (n) can also be calculated by assuming that $n_e = n_h = n$ at the minimum conductivity point¹⁸⁶. The hole and electron mobility and the intrinsic carrier concentration obtained thus are plotted as a function of temperature in **Fig 8.3b and c**. This

analysis reveals that μ and n follow different temperature dependences. The carrier mobility decreases rapidly with increasing temperature up to about 60 K and gradually increases with further increase in temperature. The intrinsic carrier concentration shows similar but more gradual changes below 250 K and then rapidly increases above this temperature. The Arrhenius fit for n above 250 K yields an activation energy of 56 meV, which corresponds to the energy required to activate carriers from defects and doping states. The dopant type can be identified from the threshold voltage shift in the transfer characteristics. For example, positive threshold voltages indicate p-type doping since negative charge carriers must be induced by positive bias to neutralize the excess holes, and vice versa for negative threshold voltages. The device is nearly neutral up to 250 K but becomes increasingly hole-doped above this temperature. This behavior indicates that thermal activation of hole carriers in this temperature regime dominates the transport properties.

8.1.4 Effect of graphene sheet size

The carriers injected into FGS-PS composite thin films must be transported through and between FGS. The carrier mobility may be limited by defects within each FGS and energy barriers at sheet-to-sheet junctions. To gain insight into the effect of sheet-to-sheet junctions, we examined field effect devices fabricated from FGS with three different average sizes (S_{ave}) ranging from 0.44 to 24 μm and three different channel lengths (L) ranging from 14 to 230 μm while other parameters were kept constant. The distribution of the flake sizes are shown in **Fig 8.4a-c**. The devices were found to have uniform conductivity irrespective of the channel length as expected for a system well above the percolation threshold. The field effect mobilities are plotted as a function of a non-dimensional length scale, S_{ave}/L , as in **Fig 8.4d**. The results indicate that the mobility is weakly dependent on flake size and nearly independent on channel length partly similar to the results previously reported for percolating networks of carbon nanotubes⁸². When the

channel length was kept constant, the mobility typically increased with increasing FGS size suggesting that sheet-to-sheet junction is limiting the mobility. The highest electron and hole mobilities of 0.2 and 0.7 $\text{cm}^2/\text{V}\cdot\text{s}$, respectively, were found for FGS composite devices with average flake sizes of 24 μm . This suggests that increasing the average size of FGS may be a key to enhancing the device performance. Another route for improving the device performance is to optimize the reduction conditions¹¹¹ for FGS thereby reducing the defects in the material. Since the typical mobility values reported for reduced GO is 1 - 10 $\text{cm}^2/\text{V}\cdot\text{s}$ ^{167, 186}, there is room for further improvement.

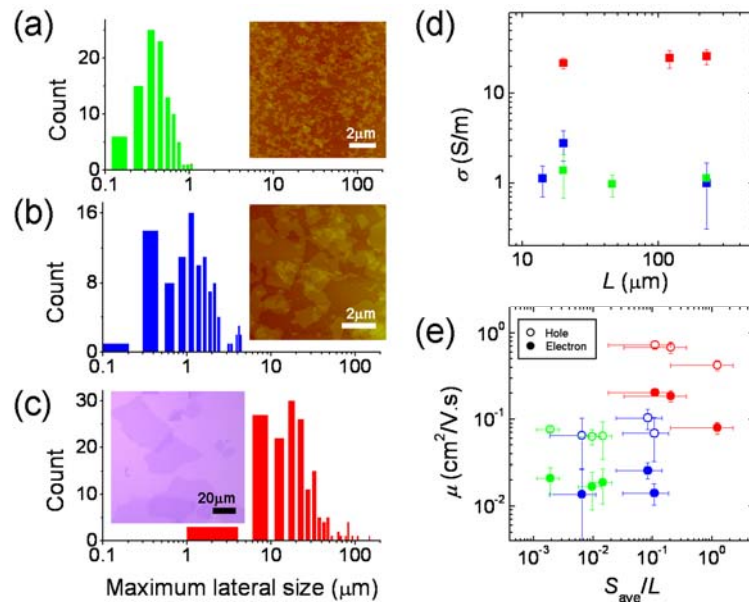


Fig 8.4 (a) Size distribution of FGS produced from graphite obtained from Bay Carbon Inc. and ultrasonicated for 10 hours. (b) Same as (a) but without ultrasonication. The inset of (a) and (b) shows the AFM image of FGS corresponding to these size distributions (c) Size distribution of FGS produced from graphite obtained from Branwell Graphite Ltd. Inset: optical micrograph of FGS corresponding to this size distribution. The average flake size (S_{ave}) for (a), (b) and (c) are 0.44, 1.5, and 22.4 μm , respectively. (d) Device conductivities measured in ambient conditions as a function of channel length. (e) Field effect mobilities as a function of non-dimensional length scale, S_{ave}/L .

The color of symbols in (d) and (e) represents different flake size distribution and corresponds to those of (a) to (c).

8.2 Field emission from graphene-based composite thin films

In the previous Sections, the semiconducting properties of graphene-based composite thin films were discussed. The operation of graphene-based composite TFTs relies on the semiconducting nature of monolayer graphene sheets. In the following Sections, we describe cold cathode field emission properties of graphene-based composite thin films. Field emission, which is an electrophysical phenomenon, is crucially dependent on the geometrical features of the material²³⁴. Although there has been tremendous interest in cold cathode field emission from carbon materials ranging from diamond^{235, 236}, amorphous carbon²³⁷, vertically aligned multi²³⁸⁻²⁴⁰ and single walled carbon nanotubes²⁴¹, and carbon nanosheets²⁴²⁻²⁴⁴, electron emission from graphene has yet to be reported. The geometrical features of graphene should increase field enhancement, allowing the extraction of electrons at extremely low threshold electric fields²⁴⁵. The electric field enhancement factor (β) for laterally macroscopic but atomically thin graphene may be of the order of a few thousand. More uniform and higher current, compared to emission from point sources such as nanotubes, may also be possible due to emission occurring over fairly large area (determined by the edge dimension of the sheet).

To take advantage of the high field enhancement, graphene sheets would have to stand on their edges and not lay laterally flat on the substrate. Vertically oriented carbon nanosheets consisting of several layers with good field emission properties grown at high temperature have been reported²⁴²⁻²⁴⁴. Virtually all deposition methods reported thus far for graphene, yield sheets laying flat on the substrate. Here, we report field emission from randomly but non-laterally oriented graphene in polymer host deposited using a simple solution based deposition method. Our approach utilizes the scheme of composite preparation¹⁴ to realize the concept of field emitting composite film^{246, 247} in which

graphene sheets represent the field emission sites. Field emission is demonstrated to occur at low threshold fields ($\sim 4 \text{ V}/\mu\text{m}$) comparable to those of typical carbon nanotube arrays²⁴⁰ and analogous composite materials based on carbon nanotube²⁴⁸. The field enhancement factor in the emitting samples was extracted to be ~ 1200 , assuming a work function of 5 eV.

8.2.1 Graphene sheet orientation

The basic methodology for preparing field emitting FGS-PS composite thin films is the same as the one described in Section 8.2. In order to achieve uniform distribution of field emitting sites and controllability over graphene sheet orientation, graphene sheets were broken down to average size of about 400 nm (see **Fig 8.4a**). The suspension of FGS and PS in DMF was spin coated in a glovebox onto degenerately doped silicon ($0.002 \sim 0.005 \Omega\cdot\text{cm}$) which had been precleaned using the RCA method to remove native oxide.

The orientation of the graphene in the thin films (thickness = 10-50 nm) can be varied from randomly oriented to laterally oriented by controlling the spin-coating speeds. The AFM images and corresponding line scans of the composite thin films deposited at two shear rates are shown in **Fig 8.5a-d**. The graphene sheets are readily visible in the Figures as sub-micron sized flakes. At low spin-coating speeds, graphene sheets are densely distributed over the substrate (**Fig 8.5a**). The brighter regions in the AFM image in **Fig 8.5a** represent graphene flakes protruding above the surface, as indicated schematically in **Fig 8.5e**. From AFM profilometry, the protrusions typically appear as 5 to 10 nm peaks above the film surface (**Fig 8.5c**). At higher spin-coating speeds, the sheets are sparsely distributed (**Fig 8.5b**) and oriented almost parallel to the substrate surface and often embedded within the PS (**Fig 8.5d**). At low spin-coating speeds, the shear force is sufficiently small to maintain the random orientation of graphene sheets and the polymer solidifies before the sheets align parallel to the substrate surface as schematically described in **Fig 8.5e and f**.

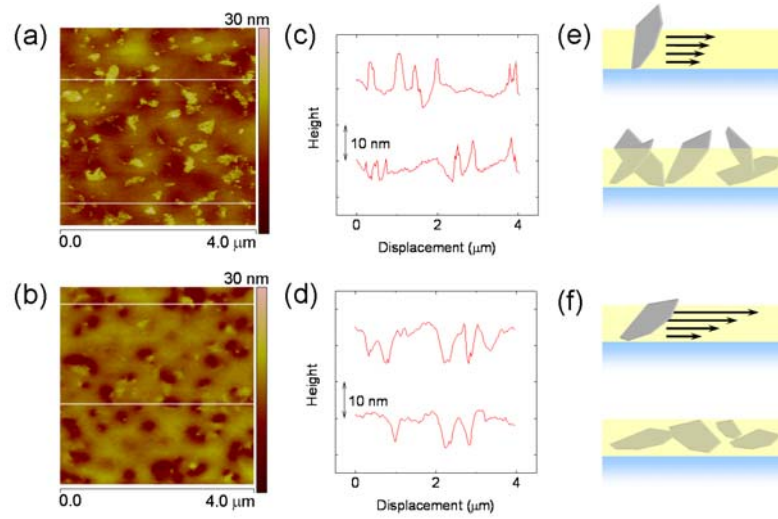


Fig 8.5 (a-d) Atomic force microscope images (AFM, Digital Instruments, Nanoscope IV, tapping mode, force constant = 40 N/m, tip curvature = 10 nm) and corresponding line scans of (a,b) 600 RPM and (b,d) 2000 RPM thin films. Brighter regions readily visible in image (a) represent graphene sheets protruding from the film surface. Schematic of the spin-coating process for the (e) low and (f) high spin-coating speeds. The arrows in the upper panels of (e) and (f) schematically represent the magnitude of the shear force experienced by the graphene flakes which results in either semi-vertical or lateral orientation.

In order for field emission to occur, electrons must be injected from the back contact into the film and then emitted into vacuum. Therefore, efficient conduction through the film and large field enhancement in proximity of the film surface are essential for electron emission. Graphene oxide is insulating but can be reduced to disorder-containing graphene in PS to render the composite thin films conductive¹⁸⁷. The through film resistance were found to be very low but accurate measurements were challenging due to the film thinness. Therefore, we used lateral resistivity to infer the orientation of the graphene sheets. The lateral resistivities ($\sim 30^{0\pm1} \Omega\cdot\text{m}$ at 10 vol. % graphene) were found to be higher for films deposited at low and high spin-coating speeds (**Fig 8.6**). Changes in

lateral resistivity with spin-coating speed can be explained by two effects: changes in the orientation at low spin-coating speeds and decreased percolation of graphene sheets at high spin speeds. That is, as the spin-coating speed is increased, graphene sheets become more preferentially oriented parallel to the substrate, thus facilitating in-plane electrical conduction. However, at very high spin-coating speeds, the distance between graphene sheets increases to the point where percolation amongst the sheets is diminished which decreases the conductivity.

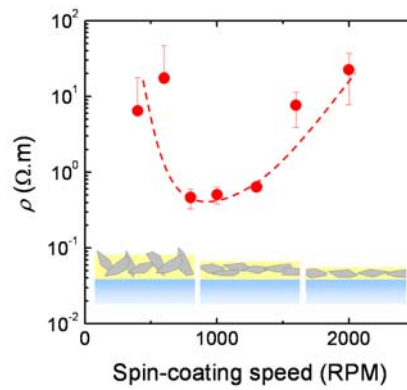


Fig 8.6 The lateral resistivity of the FGS-PS composite thin films versus the spin-coating speeds. Gold was thermally evaporated onto the composite films deposited on glass substrates and used as the electrodes. Two probe measurements were conducted in ambient using a parameter analyzer (hp4140B). The lateral resistivity, ρ , was calculated assuming $\rho = R_s \cdot t$ where R_s is the sheet resistance and t is the film thickness. The dashed line is a guide for the eyes showing the general trends.

8.2.2 Field emission properties

Field emission of the films as a function of the spin-coating speeds deposited on degenerately doped silicon substrates was measured. The measurements were performed for a cathode to anode gap of 30 μm over an area of 14 mm^2 in $< 10^{-5}$ Torr vacuum. The silicon substrate was used as the back contact electrode for the cathode and thermally evaporated aluminum on glass as the anode. Cathode and anode were separated by two

glass fiber spacers having a diameter of 30 μm . In order to confirm that the measured field emission characteristics were due to graphene and not artifacts, measurements of the bare substrate and pure PS were also performed and revealed no emission. It was necessary to apply a few cycles of voltage ramp before stable and repeatable field emission could be observed, similar to the behavior reported for other carbon^{244, 249} and non-carbon²⁵⁰ based field emitters (**Fig. 8.7a**). It is likely that sufficient current density is required to generate a conduction path through thin insulating barriers which may be present within the composite as well as at the surface of protruding graphene sheets. The field emission current density versus the applied field for two films deposited at 600 and 2000 RPMs are shown in **Fig 8.7b**. It can be seen from the Figure that the threshold field required to drive a current of 10^{-8} A/cm^2 is significantly lower for the 600 RPM sample ($\sim 4 \text{ V}/\mu\text{m}$) compared to the 2000 RPM sample ($\sim 11 \text{ V}/\mu\text{m}$). The much lower threshold field for electron emission in the 600 RPM sample suggests significantly higher field enhancement factor. Furthermore, the current from the 2000 RPM sample does not saturate at high fields, suggesting that the emission is limited by the resistance of the thin film. The low threshold field emission and higher current with increasing field further support the AFM and electrical measurement data. The $4 \text{ V}/\mu\text{m}$ threshold field for the graphene composite samples is higher than the lowest threshold fields of carbon nanotubes²⁵¹ and other carbon-based materials^{236, 252} ($0.5 - 1 \text{ V}/\mu\text{m}$) reported in the literature. However, such low threshold fields in carbonaceous materials have been found to be a consequence of local inhomogeneities (i.e. large protrusion) and careful analysis reveals that for uniformly spaced emitters, field emission occurs at several $\text{V}/\mu\text{m}$ (Ref. ²⁴⁰). The maximum current density we obtained was 1 mA/cm^2 , which is below the highest value reported for carbon nanotubes ($\sim 4 \text{ A/cm}^2$)²⁵³ but consistent with vertically aligned nanotubes when space charge within the emitted beam is not mediated²⁵⁴.

In order to confirm that FGS-PS composite configuration allows efficient extraction of electrons into vacuum, we investigated field emission from PS free graphene

thin films prepared using vacuum filtration method introduced in Chapter 6. All graphene sheets in graphene thin films were virtually laying parallel to the substrate. Wrinkles were generally present for thick films providing potential sites for field emission (**Fig 8.7d inset**). In fact, no field emission was observed for extremely thin films (< 5 nm) without significant surface corrugations. Field emission characteristics of graphene thin films deposited on Si substrates are shown in **Fig 8.7d**. Threshold voltage for field emission was above 10 V/ μm for two deposition conditions investigated, which is appreciably higher than the values obtained for graphene composite thin films with semi-vertically oriented graphene sheets.

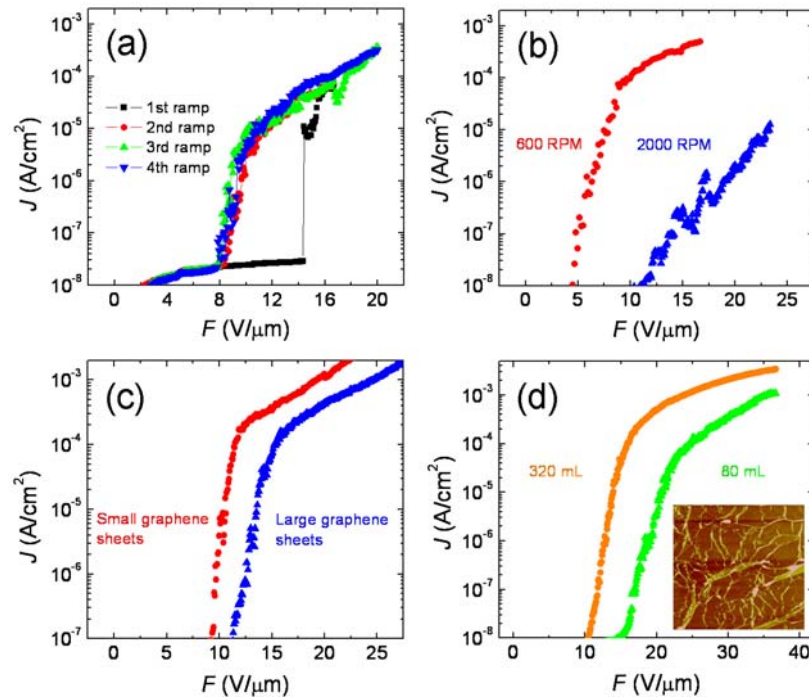


Fig 8.7 (a) Field emission current density as a function of applied field for initial ramp cycles. (b,c) Field emission characteristics of FGS-PS composite thin films as a function of (b) spin-coating speeds and (c) graphene sheet size. The spin-coating speed for thin films in (c) was 1000 rpm for both samples. The average lateral graphene sheet size was 0.44 and 1.51 μm for red and blue plot respectively. (d) Field emission characteristics of graphene thin films prepared at two different

effective filtration volumes of 0.33 mg/L GO suspension (see Chapter 6 and 7 for details). Inset shows an AFM image of surface morphology of a 320 mL thin film (10 μm scan).

8.2.3 Fowler-Nordheim analysis

According to classical Fowler-Nordheim (F-N) theory, the density of field emission current under low field ($< 10^4 \text{ V}/\mu\text{m}$) approximation has the following form:

$$J = \frac{A}{\phi} E^2 \exp\left(\frac{1.03Be^3}{\phi^{1/2}} - \frac{0.95B\phi^{3/2}}{E}\right) \quad (8.1)$$

where A and B are constants expressed in combination of electron charge (e), mass (m), and Planck's constant (h); $A = e^3/8\pi h = 1.5414 \times 10^{-6} \text{ A}\cdot\text{eV}\cdot\text{V}^{-1}$; $B = 8\pi (2m)^{1/2} / 3he = 6.8309 \times 10^9 \text{ eV}^{-3/2}\cdot\text{V}\cdot\text{m}^{-1}$; E is the local electric field in V/m , and ϕ is the material work function in eV . The local electric field (E) is related to the macroscopic electric field (F) far away from the emission sites as $E = \beta F$ where β is the geometrical enhancement factor. The macroscopic electric field (F) is expressed as V/d , where V is the applied voltage and d is the interplanar (cathode-anode) spacing. The geometrical enhancement factor can be extracted from the experimental data by examining $\ln(J/E^2)$ vs $1/E$, which is known as the F-N plot. Assuming the value of ϕ for the FGS to be 5 eV , β can be obtained from the slope of F-N plot as mentioned in the main text. Non-linear regime in the F-N plot indicates statistical distribution of geometrical, structural and electronic characteristics of field emitting sites. To a first approximation, field emission sites are estimated to have normal (Gaussian) distribution in size with average size, r_0 , and standard deviation, σ , in which case Eq 8.1 can be rewritten as:

$$J = CnF^2 \exp\left[-\frac{Dr_0}{F} + \frac{\sigma^2}{2}\left(\frac{D}{F}\right)^2\right] \quad (8.2)$$

where

$$C = \frac{A\pi h^2}{\phi} \exp\left(\frac{10.1}{\sqrt{\phi}}\right)$$

$$D = 0.95B \frac{\phi^{3/2}}{h}$$

and n is the emission site density, which is typically electric field dependent.

For ideal vertically-oriented whisker-shaped point emitters such as nanotubes and nanowires, the geometrical (or field) enhancement factor (β) is estimated to be equal to the aspect ratio of the emitter, h/r where h is the height and r is the radius. This expression is modified as the geometry deviates from the whisker shape. It has been recently calculated that for an ideal two-dimensional metallic field emitter with width w , geometrical enhancement factor can be expressed as $(\pi h/2w)^{1/2}$ (Ref. ²⁵⁵). In the case of FGS-PS composites thin films, field emission site corresponds to protruded graphene sheets, which can either represent edge or point emission source as illustrated in **Fig 8.8**. Latter case exhibit further complication as sharpness of the emitter given by the angle θ (**Fig 8.8**) introduces another degree of freedom. Orientation of graphene sheets with respect to the substrate surface is a common variable in either case (not shown in the Figure for clarity). In addition to the geometrical considerations, other mechanisms such as the triple junction effect²⁵⁶⁻²⁵⁸ could also lead to significant field enhancement. Further investigations are required for determining the exact effects responsible for the field emission in G-PS composites.

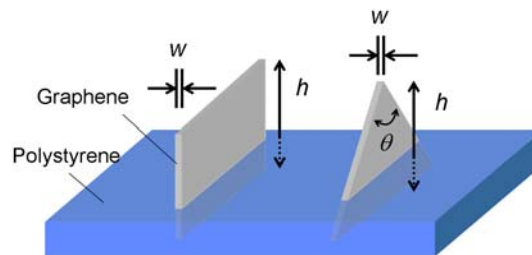


Fig 8.8 Schematics showing graphene field emitters protruding from the PS matrix. Two potential emission sources representing edge (left) and point (right) emitters are illustrated.

The field enhancement factor (β) can be extracted from the field emission data,

assuming that the data in **Fig 8.7b** are described by the Fowler-Nordheim (F-N) equation²⁵⁹. β can be obtained from the linear region of the F-N plot shown in **Fig 8.9a** and assuming the work function of graphene to be 5 eV. The curvature of F-N plot at low field may be attributed to the statistical variation of geometrical, structural and electronic characteristics of field emitting sites²⁶⁰. The β values from the F-N plots were found to be ~ 1200 and 700 for the 600 and 2000 RPM samples, respectively. Similar analysis for field emission characteristics of graphene thin films yielded β values below 300 (**Fig 8.9b**). These results indicate that the presence of PS is necessary to achieve large field enhancement. Thus, it appears that for composite films deposited at 600 RPM, field enhancement is facilitated by the PS matrix²⁴⁸ which enables the graphene sheets to be oriented at some angle with respect to the substrate surface. Besides the morphological and topographical factors mentioned above, field enhancement can also be determined by interfacial effects. Graphene sheets are likely to be covered by PS forming metal-insulator-vacuum (MIV) interface²⁴⁷ or partially exposed forming a triple junction²⁵⁸ which complicates the physical mechanism of field emission^{261, 262}. Image analysis of the samples after the field emission measurements revealed that the surface was largely unchanged, indicating that cold cathode emission is responsible for the observed data and not due to artifacts such as microarcing,

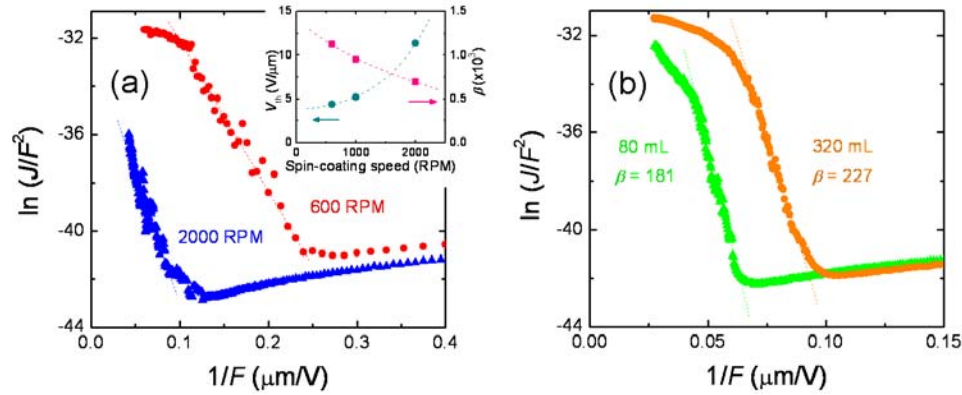


Fig 8.9 Fowler-Nordheim (F-N) plots corresponding to the data in (a) Fig 8.7b and (b) d. The inset shows the trend of the threshold voltage and field enhancement factor as a function of the spin-coating speeds. The dashed line is a guide for the eyes showing the general trends.

8.2.4 Field emission stability and emission site distribution

Stability of field emission current was measured under constant voltage. Emission current typically decayed about one to two orders of magnitude over 10 to 15 hours as shown in **Fig 8.10a**. The decay may be explained by the burn-out of graphene sheets due to constant local heating. Excessive local heating may also cause local melting of PS matrix, which eventually lead to failure of emitters.

Further, distribution of field emission sites was investigated by using ITO/glass as the anode (**Fig 8.10b**). Field emitted electrons bombarding the ITO surface with sufficient energy and density cause the ITO to luminesce allowing the observation of emission sites. **Fig 8.10c** shows a photograph taken at 10 s exposure during the measurement of 1×10^{-5} A field emission current. The area of the ITO coated anode was 14 mm^2 . Several bright spots indicate that emission site is not homogeneously distributed over the sample. ITO requires relatively large electron energy and dose to exhibit noticeable luminescence and therefore low-current emission sites are difficult to identify. Further study is required to conclude the uniformity of field emission.

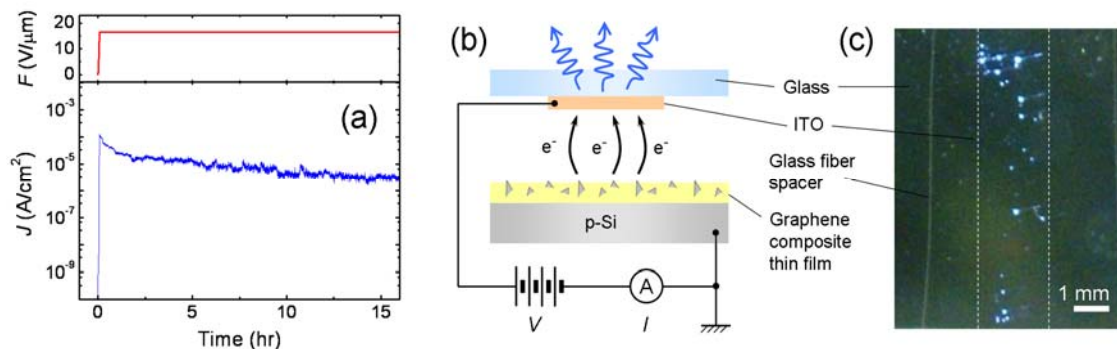


Fig 8.10 (a) Electric field and field emission current density as a function of time. (b) Schematic of experimental configuration for investigating field emission site distribution. (c) Photograph showing luminescent spots of ITO corresponding to the field emission sites.

8.3 Chapter summary

In summary, solution-processable composite thin films consisting of functionalized graphene sheets (FGS) and polystyrene (PS) exhibiting field modulated transport and cold cathode field emission have been described. The FGS are well dispersed and percolating within the PS matrix, giving rise to electrical properties similar to individual monolayer of reduced GO and its thin films. The material is intrinsically hole-doped at room temperature and becomes increasingly p-type at higher temperatures. The carrier mobilities are limited by the disorder of each FGS and the sheet-to-sheet junctions. By depositing the composite such that the sheets are somewhat vertically aligned leads to graphene sheets protruding from the film surface. This allows electron emission to occur at low threshold voltage, making graphene an excellent candidate for field emission applications.

The reported scheme for fabricating composite thin films from graphene and a commodity plastic is highly versatile and scaleable. The ability to deposit semiconducting and field emitting graphene composite thin films from solution may open up exciting routes towards low-cost, macro-scale thin film electronics.

Chapter 9

Conclusions and suggested future works

In this thesis, the potential of SWNT and graphene thin films as solution-processable electronic materials has been explored. We showed that liquid dispersions of SWNTs and graphene can be achieved via appropriate use of surfactants, polymers or chemical modification. Dispersion of SWNTs and graphene in liquid allow controllable and uniform deposition of these materials over large areas as thin films at room temperature with high throughput. We investigated the correlation of optical and electrical properties of SWNT

and graphene thin films with various factors such as network density, film thickness, chemical structures, and doping conditions. We demonstrated that by varying deposition conditions and post-deposition treatments, the properties of thin films can be tuned over a wide range to meet the performance requirements of different types of devices. Low sheet resistance and high transparency of SWNTs and graphene thin films suggest their potential usage as transparent conductors (TC). We have demonstrated that post-deposition functionalization is a simple route towards improving the performance of SWNTs and graphene-based TCs. One of the issues inherent to solution-processing of nano-materials is aggregation in suspension. We have investigated the dynamics of SWNT bundling in solution and identified its negative impacts on the resulting thin film properties. Chemical derivation of graphene from graphite is an emerging field of research with significant potential. We carefully studied the structural properties of graphene oxide which had been poorly understood prior to our work. We identified significant structural disorder in GO arising from the vigorous oxidation process and correlated it to the thin film electrical properties. Our structural and electrical studies provide insight into a potential route towards achieving high performance devices from GO. Further, we investigated the potential application of graphene-based composite thin films as thin film transistors (TFTs) and cold cathode field emitters. The field effect mobility of nearly $1 \text{ cm}^2/\text{V}\cdot\text{s}$ obtained from the TFTs is comparable to that of commercial amorphous silicon TFTs albeit with lower on/off ratio. We observed field emission from graphene-based composite thin films at low threshold fields ($\sim 4 \text{ V}/\mu\text{m}$), indicating that atomically sharp edge of graphene sheets represents sites for large field enhancement.

Our studies demonstrate that SWNT and graphene thin films are new class of materials that exhibit unique optical and electrical properties which may open up avenues for technological implementation into electronic devices. While the current performance of these devices are not optimized, there is significant room for improvements and further understanding of the material is crucial for uncovering its full potential. Below,

recommendations for future works are briefly summarized.

9.1 SWNT network thin films

Difficulties in the study of SWNT network thin films arise from the intrinsic heterogeneity of the materials where both metallic and semiconducting nanotubes are generally present at fixed proportions. Efforts to separate metallic and semiconducting nanotubes have resulted in some success^{139, 263-267}. However, these results have not translated into significant improvements in the SWNT network-based electronic devices. The reason for this is not clear and requires detailed investigation. Recent report by Cao *et al.*⁸³ indicates that it is possible to achieve high performance TFTs with unsorted chemical-vapor-deposition (CVD)-grown SWNT network by carefully designing the geometry of devices. The field effect mobility values of 50 cm²/V·s achieved with these devices are consistently higher by more than an order of magnitude compared to those achieved with typical solution-processed counterparts even when the nanotubes are aligned and sorted^{139, 268}. This comparison suggests that the presence of bundles, which is one of the major differences between the CVD-grown and solution-processed network, play an essential role in limiting the device performance. Our study presented in Chapter 5 verified that presence of SWNT bundles alter the percolation condition of metallic SWNTs and results in large off-state current in TFTs. However, the effect of bundles on the conduction mechanism requires further attention. In tackling this issue, it is crucial to understand how the transport properties of individual bundles differ from those of individual nanotubes. Reich *et al.*²⁶⁹ reported using ab-initio calculations that the electronic structure of individual nanotubes in a bundle is obscured and showed that the band gap of a semiconducting SWNT is reduced. It is of interest to experimentally verify this effect by testing the electrical transport properties of SWNT bundles of known size and composition. Extensive Raman spectroscopy and atomic force microscopy analysis combined with the electrical measurements could provide insight into this issue.

9.2 Chemically derived graphene thin films

A major challenge for graphene based transistors is in rendering the zero band gap graphene into a finite gap semiconductor. This is essential for digital device applications where a transistor must be completely switched off. Intrinsic graphene suffers from this requirement due to finite minimum conductivity on the order of twice the quantum conductance. Interestingly, recent reports suggest that chemically modified graphene are semiconductors with finite band gap^{106, 108, 233, 270}. Experimental studies show that the minimum conductivity of chemically modified graphene is well below that of quantum conductance. Sun *et al.*²³³ and Luo *et al.*²⁷⁰ recently reported broad-spectrum photoluminescence from GO which potentially arises from confinement- or disorder-induced local band gap. These observations prompt detailed investigation on the electronic structure of GO, which is not clearly understood due to its semi-amorphous nature. Our studies reveal that GO is an insulator whereas reduced GO is semi-metallic. It is expected that during the transition from insulator to semi-metal, GO becomes a semiconductor with finite band gap. Careful transport studies combined with spectroscopic analysis of GO with progressive reduction treatment are likely to provide insight into this subject.

To optimize the properties of chemically derived graphene thin film electronic devices, it is also important to explore routes to obtaining high quality material with minimum defects, which allow solution-processing. There are two different approaches for achieving this goal. One is to refine the reduction process for GO and the other is to devise a process for directly exfoliating graphite without oxidation process. Various methods have been recently proposed to achieve efficient reduction of GO in solution^{175, 179, 271-273}. However, little information is available in the literature to conclude the most efficient route of GO reduction. Speculations based on our studies presented in Chapter 6 suggest that combinations of various reduction procedures are expected to result in efficient restoration

of sp^2 carbon network in GO. Hernandez *et al.*¹⁶⁰ recently reported that graphite can be directly exfoliated into individual monolayers in various organic solvents albeit at very low yields and small flake sizes. It was found that various solvents having surface energy value similar to that of graphite are capable of exfoliating graphite. The proposed route is attractive as it obviates the need for rigorous oxidation which results in large concentration of defects in the graphene sheets. In this approach, improvement in the yield and size of graphene sheets is an essential task for technological implementation. The two routes mentioned here do not allow high yield and high quality simultaneously. Based on the knowledge attained in these studies, it is of interest to test whether a combination of the two approaches here provide a route towards producing high yield of graphene sheets with high quality as liquid suspensions. It is expected that detailed characterization of graphite surface energy with moderate oxygen intercalation will allow appropriate choice of solvents for efficiently exfoliating graphite into individual sheets.

Bibliography

1. R. Saito, G. Dresselhaus and M.S. Dresselhaus. Physical Properties of Carbon Nanotubes (Imperial College Press, London, 1998).
2. B.T. Kelly. Physics of graphite (Applied Science Publishers, London, 1981).
3. H.W. Kroto, J.R. Heath, S.C. O'Brien, R.F. Curl and R.E. Smalley. C_{60} : Buckminsterfullerene. *Nature* 318, 162-3 (1985).
4. S. Iijima. Helical microtubules of graphitic carbon. *Nature* 354, 56-8 (1991).
5. K.S. Novoselov, A.K. Geim, S.V. Morozov, D. Jiang, Y. Zhang, S.V. Dubonos, I.V. Grigorieva and A.A. Firsov. Electric field effect in atomically thin carbon films. *Science* 306, 666-669 (2004).
6. M.M.J. Treacy, T.W. Ebbesen and J.M. Gibson. Exceptionally high Young's modulus observed for individual carbon nanotubes. *Nature* 381, 678-680 (1996).
7. M.F. Yu, O. Lourie, M.J. Dyer, K. Moloni, T.F. Kelly and R.S. Ruoff. Strength and breaking mechanism of multiwalled carbon nanotubes under tensile load. *Science* 287, 637-640 (2000).
8. J.P. Salvetat, G.A.D. Briggs, J.M. Bonard, R.R. Bacsá, A.J. Kulik, T. Stockli, N.A. Burnham and L. Forro. Elastic and shear moduli of single-walled carbon nanotube ropes. *Phys. Rev. Lett.* 82, 944-947 (1999).
9. C. Lee, X. Wei, J.W. Kysar and J. Hone. Measurement of the elastic properties and intrinsic strength of monolayer graphene. *Science* 321, 385 (2008).
10. D.-Y. Khang, J. Xiao, C. Kocabas, S. MacLaren, T. Banks, H. Jiang, Y.Y. Huang and J.A. Rogers. Molecular scale buckling mechanics in individual aligned single-wall carbon nanotubes on elastomeric substrates. *Nano Lett.* 8, 124-130 (2008).
11. M.-F. Yu, B.S. Files, S. Arepalli and R.S. Ruoff. Tensile loading of ropes of single wall carbon nanotubes and their mechanical properties. *Phys. Rev. Lett.* 84, 5552 (2000).
12. E.T. Thostenson, Z.F. Ren and T.W. Chou. Advances in the science and technology of carbon nanotubes and their composites: a review. *Compos. Sci. Technol.* 61, 1899-1912 (2001).
13. P.M. Ajayan, L.S. Schadler, C. Giannaris and A. Rubio. Single-walled carbon nanotube-polymer composites: Strength and weakness. *Adv. Mater.* 12, 750 (2000).
14. S. Stankovich, D.A. Dikin, G.H.B. Dommett, K.M. Kohlhaas, E.J. Zimney, E.A. Stach, R.D. Piner, S.T. Nguyen and R.S. Ruoff. Graphene-based composite materials. *Nature* 442, 282-286 (2006).
15. Z. Yao, C.L. Kane and C. Dekker. High-field electrical transport in single-wall carbon nanotubes. *Phys. Rev. Lett.* 84, 2941 (2000).
16. A. Javey, G. Jing, W. Qian, M. Lundstrom and D. Hongjie. Ballistic carbon nanotube field-effect transistors. *Nature* 424, 654-7 (2003).
17. P.G. Collins, M.S. Arnold and P. Avouris. Engineering carbon nanotubes and nanotube circuits using electrical breakdown. *Science* 292, 706-13 (2001).
18. J. Moser, A. Barreiro and A. Bachtold. Current-induced cleaning of graphene. *Appl. Phys. Lett.* 91, 163513 (2007).
19. X. Du, I. Skachko, A. Barker and E.Y. Andrei. Approaching ballistic transport in suspended graphene. *Nature Nanotech.* 3, 491-495 (2008).

20. T. Durkop, S.A. Getty, E. Cobas and M.S. Fuhrer. Extraordinary mobility in semiconducting carbon nanotubes. *Nano Letters* 4, 35-9 (2004).
21. A. Javey, J. Guo, D.B. Farmer, Q. Wang, E. Yenilmez, R.G. Gordon, M. Lundstrom and H. Dai. Self-aligned ballistic molecular transistors and electrically parallel nanotube arrays. *Nano Lett.* 4, 1319-1322 (2004).
22. Y.-M. Lin, K.A. Jenkins, A. Valdes-Garcia, J.P. Small, D.B. Farmer and P. Avouris. Operation of graphene transistors at gigahertz frequencies. *Nano Lett.* 9, 422-426 (2008).
23. K. Tsukagoshi, B.W. Alphenaar and H. Ago. Coherent transport of electron spin in a ferromagnetically contacted carbon nanotube. *Nature* 401, 572-574 (1999).
24. S. Sahoo, T. Kontos, J. Furer, C. Hoffmann, M. Graber, A. Cottet and C. Schonenberger. Electric field control of spin transport. *Nature Phys.* 1, 99-102 (2005).
25. N. Tombros, C. Jozsa, M. Popinciuc, H.T. Jonkman and B.J. van Wees. Electronic spin transport and spin precession in single graphene layers at room temperature. *Nature* 448, 571-574 (2007).
26. E. Pop, D. Mann, Q. Wang, K. Goodson and H. Dai. Thermal conductance of an individual single-wall carbon nanotube above room temperature. *Nano Lett.* 6, 96-100 (2006).
27. A.A. Balandin, S. Ghosh, W. Bao, I. Calizo, D. Teweldebrhan, F. Miao and C.N. Lau. Superior thermal conductivity of single-layer graphene. *Nano Lett.* 8, 902-907 (2008).
28. R. Jackson, B. Domercq, R. Jain, B. Kippelen and S. Graham. Stability of doped transparent carbon nanotube electrodes. *Adv. Funct. Mater* 18, 2548-2554 (2008).
29. F. Schedin, A.K. Geim, S.V. Morozov, E.W. Hill, P. Blake, M.I. Katsnelson and K.S. Novoselov. Detection of individual gas molecules adsorbed on graphene. *Nature Mater.* 6, 652-655 (2007).
30. P.G. Collins, K. Bradley, M. Ishigami and A. Zett. Extreme oxygen sensitivity of electronic properties of carbon nanotubes. *Science* 287, 1801-1804 (2000).
31. E.S. Snow, F.K. Perkins, E.J. Houser, S.C. Badescu and T.L. Reinecke. Chemical detection with a single-walled carbon nanotube capacitor. *Science* 307, 1942-1945 (2005).
32. E. Frackowiak. Carbon materials for supercapacitor application. *Phys. Chem. Chem. Phys.* 9, 1774 - 1785 (2007).
33. M.D. Stoller, S. Park, Y. Zhu, J. An and R.S. Ruoff. Graphene-based ultracapacitors. *Nano Lett.* 8, 3498-3502 (2008).
34. K.S. Novoselov, A.K. Geim, S.V. Morozov, D. Jiang, M.I. Katsnelson, I.V. Grigorieva, S.V. Dubonos and A.A. Firsov. Two-dimensional gas of massless Dirac fermions in graphene. *Nature* 438, 197-200 (2005).
35. J. Hone, B. Batlogg, Z. Benes, A.T. Johnson and J.E. Fischer. Quantized phonon spectrum of single-wall carbon nanotubes. *Science* 289, 1730-1733 (2000).
36. S. Pisana, M. Lazzeri, C. Casiraghi, K.S. Novoselov, A.K. Geim, A.C. Ferrari and F. Mauri. Breakdown of the adiabatic Born-Oppenheimer approximation in graphene. *Nature Mater.* 6, 198-201 (2007).
37. A.K. Geim and K.S. Novoselov. The rise of graphene. *Nature Mater.* 6, 183-191 (2007).

38. J.W. Hill and R.H. Petrucci. General Chemistry (Prentice Hall, NJ, 2002).
39. P. Avouris, Z.H. Chen and V. Perebeinos. Carbon-based electronics. *Nature Nanotech.* 2, 605-615 (2007).
40. R. Saito, M. Fujita, G. Dresselhaus and M.S. Dresselhaus. Electronic structure of chiral graphene tubules. *Appl. Phys. Lett.* 60, 2204-2206 (1992).
41. K. Nakada, M. Fujita, G. Dresselhaus and M.S. Dresselhaus. Edge state in graphene ribbons: Nanometer size effect and edge shape dependence. *Phys. Rev. B* 54, 17954 (1996).
42. S. Reich, C. Thomsen and J. Maultzsch. Carbon Nanotube - Basic Concepts and Physical Properties (Wiley-VCH Verlag GmbH & Co. KGaA, Weinheim, 2004).
43. K.S. Novoselov, D. Jiang, F. Schedin, T.J. Booth, V.V. Khotkevich, S.V. Morozov and A.K. Geim. Two-dimensional atomic crystals. *Proc. Nat. Acad. Sci. U.S.A.* 102, 10451-10453 (2005).
44. Z. Chen, Y.-M. Lin, M.J. Rooks and P. Avouris. Graphene nano-ribbon electronics. *Phys. E* 40, 228-232 (2007).
45. M. Ishigami, J.H. Chen, W.G. Cullen, M.S. Fuhrer and E.D. Williams. Atomic Structure of Graphene on SiO₂. *Nano Lett.* 7, 1643 (2007).
46. E. Stolyarova, K.T. Rim, S. Ryu, J. Maultzsch, P. Kim, L.E. Brus, T.F. Heinz, M.S. Hybertsen and G.W. Flynn. High-resolution scanning tunneling microscopy imaging of mesoscopic graphene sheets on an insulating surface. *Proc. Natl. Acad. Sci.* 104, 9209-9212 (2007).
47. M.H. Gass, U. Bangert, A.L. Bleloch, P. Wang, R.R. Nair and A.K. Geim. Free-standing graphene at atomic resolution. *Nature Nanotech.* 3, 676-681 (2008).
48. J.C. Meyer, C. Kisielowski, R. Erni, M.D. Rossell, M.F. Crommie and A. Zettl. Direct Imaging of Lattice Atoms and Topological Defects in Graphene Membranes. *Nano Lett.* 8, 3582-3586 (2008).
49. J. Martin, N. Akerman, G. Ulbricht, T. Lohmann, J.H. Smet, K.v. Klitzing and A. Yacoby. Observation of electron-hole puddles in graphene using a scanning single-electron transistor. *Nature Phys.* 4, 144-148 (2008).
50. Y. Zhang, V.W. Brar, F. Wang, C. Girit, Y. Yayon, M. Panlasigui, A. Zettl and M.F. Crommie. Giant phonon-induced conductance in scanning tunnelling spectroscopy of gate-tunable graphene. *Nat Phys* 4, 627-630 (2008).
51. J.-C. Charlier, X. Blase and S. Roche. Electronic and transport properties of nanotubes. *Rev. Mod. Phys.* 79, 677-732 (2007).
52. J.W.G. Wildoer, L.C. Venema, A.G. Rinzler, R.E. Smalley and C. Dekker. Electronic structure of atomically resolved carbon nanotubes. *Nature* 391, 59-62 (1998).
53. A.H.C. Neto, F. Guinea, N.M.R. Peres, K.S. Novoselov and A.K. Geim. The electronic properties of graphene *Rev. Mod. Phys.* 81, 109 (2009).
54. P. Avouris, J. Appenzeller, R. Martel and S.J. Wind. Carbon nanotube electronics. *Proc. IEEE* 91, 1772 (2003).
55. B. Partoens and F.M. Peeters. From graphene to graphite: Electronic structure around the K point. *Phys. Rev. B* 74, 075404 (2006).
56. J.W. Mintmire and C.T. White. Universal density of states for carbon nanotubes. *Phys. Rev. Lett.* 81, 2506 (1998).

57. T.W. Odom, H. Jin-Lin, P. Kim and C.M. Lieber. Atomic structure and electronic properties of single-walled carbon nanotubes. *Nature* 391, 62-4 (1998).
58. M.J. O'Connell, S.M. Bachilo, C.B. Huffman, V.C. Moore, M.S. Strano, E.H. Haroz, K.L. Rialon, P.J. Boul, W.H. Noon, C. Kittrell, J. Ma, R.H. Hauge, R.B. Weisman and R.E. Smalley. Band gap fluorescence from Individual single-walled carbon nanotubes. *Science* 297, 593-596 (2002).
59. S.M. Bachilo, M.S. Strano, C. Kittrell, R.H. Hauge, R.E. Smalley and R.B. Weisman. Structure-assigned optical spectra of single-walled carbon nanotubes. *Science* 298, 2361-2366 (2002).
60. T.W. Odom, J.-L. Huang, P. Kim and C.M. Lieber. Structure and electronic properties of carbon nanotubes. *J. Phys. Chem. B* 104, 2794-2809 (2000).
61. H. Kataura, Y. Kumazawa, Y. Maniwa, I. Umezu, S. Suzuki, Y. Ohtsuka and Y. Achiba. Optical properties of single-wall carbon nanotubes. *Synth. Met.* 103, 2555-2558 (1999).
62. A.G. Souza Filho, A. Jorio, J.H. Hafner, C.M. Lieber, R. Saito, M.A. Pimenta, G. Dresselhaus and M.S. Dresselhaus. Electronic transition energy E_{ii} for an isolated (n,m) single-wall carbon nanotube obtained by anti-Stokes/Stokes resonant Raman intensity ratio. *Phys. Rev. B* 63, 241404 (2001).
63. T. Ando and T. Nakanishi. Impurity scattering in carbon nanotubes – absence of back scattering –. *J. Phys. Soc. Jpn.* 67, 1704-1713 (1998).
64. R. Martel, T. Schmidt, H.R. Shea, T. Hertel and P. Avouris. Single- and multi-wall carbon nanotube field-effect transistors. *Appl. Phys. Lett.* 73, 2447-9 (1998).
65. J. Kong, E. Yenilmez, T.W. Tombler, W. Kim, H. Dai, R.B. Laughlin, L. Liu, C.S. Jayanthi and S.Y. Wu. Quantum interference and ballistic transmission in nanotube electron waveguides. *Phys. Rev. Lett.* 87, 106801-1 (2001).
66. S.J. Tans, R.M. Verschueren and C. Dekker. Room temperature transistor based on a single carbon nanotube. *Nature* 393, 49-52 (1998).
67. J. Appenzeller, J. Knoch, V. Derycke, R. Martel, S. Wind and P. Avouris. Field-modulated carrier transport in carbon nanotube transistors. *Phys. Rev. Lett.* 89, 126801-1 (2002).
68. S. Heinze, J. Tersoff, R. Martel, V. Derycke, J. Appenzeller and P. Avouris. Carbon nanotubes as Schottky barrier transistors. *Phys. Rev. Lett.* 89, 106801-1 (2002).
69. L. Yu-Ming, J. Appenzeller, J. Knoch and P. Avouris. High-performance carbon nanotube field-effect transistor with tunable polarities. *IEEE Trans. Nanotech.* 4, 481-9 (2005).
70. C. Jia, C. Klinke, A. Afzali and P. Avouris. Self-aligned carbon nanotube transistors with charge transfer doping. *Appl. Phys. Lett.* 86, 123108-1 (2005).
71. C. Xiaodong, M. Freitag, R. Martel, L. Brus and P. Avouris. Controlling energy-level alignments at carbon nanotube/Au contacts. *Nano Letters* 3, 783-7 (2003).
72. T. Durkop, B.M. Kim and M.S. Fuhrer. Properties and applications of high-mobility semiconducting nanotubes. *J. Phys.: Condens. Matter* 16, R553–R580 (2004).
73. J. Kong, N.R. Franklin, C. Zhou, M.G. Chapline, S. Peng, K. Cho and H. Dai. Nanotube molecular wires as chemical sensors *Science* 287, 622 - 625 (2000).

74. T.J. McDonald, C. Engtrakul, M. Jones, G. Rumbles and M.J. Heben. Kinetics of PL quenching during single-walled carbon nanotube rebundling and diameter-dependent surfactant interactions. *J. Phys. Chem. B* 110, 25339-25346 (2006).
75. R. Seidel, A.P. Graham, E. Unger, G.S. Duesberg, M. Liebau, W. Steinhoegl, F. Kreupl, W. Hoenlein and W. Pompe. High-current nanotube transistors. *Nano Lett.* 4, 831-4 (2004).
76. T. Fukao, S. Nakamura, H. Kataura and M. Shiraishi. Solution-processed single-walled carbon nanotube transistors with high mobility and large on/off ratio. *Jpn. J. Appl. Phys.* 45, 6524-6527 (2006).
77. S.J. Kang, C. Kocabas, T. Ozel, M. Shim, N. Pimparkar, M.A. Alam, S.V. Rotkin and J.A. Rogers. High-performance electronics using dense, perfectly aligned arrays of single-walled carbon nanotubes. *Nature Nanotech.* 2, 230-236 (2007).
78. A.M. Cassell, J.A. Raymakers, J. Kong and H.J. Dai. Large scale CVD synthesis of single-walled carbon nanotubes. *J. Phys. Chem. B* 103, 6484-6492 (1999).
79. E.S. Snow, J.P. Novak, P.M. Campbell and D. Park. Random networks of carbon nanotubes as an electronic material. *Appl. Phys. Lett.* 82, 2145-2147 (2003).
80. L. Hu, D.S. Hecht and G. Gruner. Percolation in transparent and conducting carbon nanotube networks. *Nano Lett.* 4, 2513-2517 (2004).
81. H.E. Unalan, G. Fanchini, A. Kanwal, A. Du Pasquier and M. Chhowalla. Design criteria for transparent single-wall carbon nanotube thin-film transistors. *Nano Lett.* 6, 677-682 (2006).
82. S.H. Hur, C. Kocabas, A. Gaur, O.O. Park, M. Shim and J.A. Rogers. Printed thin-film transistors and complementary logic gates that use polymer-coated single-walled carbon nanotube networks. *J. Appl. Phys.* 98, 114302 (2005).
83. Q. Cao, H.-s. Kim, N. Pimparkar, J.P. Kulkarni, C. Wang, M. Shim, K. Roy, M.A. Alam and J.A. Rogers. Medium-scale carbon nanotube thin-film integrated circuits on flexible plastic substrates. *Nature* 454, 495-500 (2008).
84. M.S. Fuhrer, J. Nygard, L. Shih, M. Forero, Y. Young-Gui, M.S.C. Mazzoni, C. Hyounghoon Joon, I. Jisoon, S.G. Louie, A. Zettl and P.L. McEuen. Crossed nanotube junctions. *Science* 288, 494-7 (2000).
85. M. Stadermann, S.J. Papadakis, M.R. Falvo, J. Novak, E. Snow, Q. Fu, J. Liu, Y. Fridman, J.J. Boland, R. Superfine and S. Washburn. Nanoscale study of conduction through carbon nanotube networks. *Phys. Rev. B* 69, 201402 (2004).
86. Y. Kodama, R. Sato, N. Inami, E. Shikoh, Y. Yamamoto, H. Hori, H. Kataura and A. Fujiwara. Field-effect modulation of contact resistance between carbon nanotubes. *Appl. Phys. Lett.* 91, 133515 (2007).
87. M.A. Topinka, M.W. Rowell, D. Goldhaber-Gordon, M.D. McGehee, D.S. Hecht and G. Gruner. Charge transport in interpenetrating networks of semiconducting and metallic carbon nanotubes. *Nano Lett.*, In press (2009).
88. K.A. Mkhoyan, A.W. Contryman, J. Silcox, D.A. Stewart, G. Eda, C. Mattevi, S. Miller and M. Chhowalla. Atomic and electronic structure of graphene-oxide. *Nano Lett.* 9, 1058-1063 (2009).
89. Y.W. Tan, Y. Zhang, K. Bolotin, Y. Zhao, S. Adam, E.H. Hwang, S. Das Sarma, H.L. Stormer and P. Kim. Measurement of scattering rate and minimum conductivity in graphene. *Phys. Rev. Lett.* 99, 246803 (2007).

90. Y.B. Zhang, Y.W. Tan, H.L. Stormer and P. Kim. Experimental observation of the quantum Hall effect and Berry's phase in graphene. *Nature* 438, 201-204 (2005).
91. T. Ando. Screening effect and impurity scattering in monolayer graphene. *J. Phys. Soc. Jpn* 75, 074716 (2006).
92. S. Adam, E.H. Hwang, V.M. Galitski and S.D. Sarma. A self-consistent theory for graphene transport. *Proc. Natl. Acad. Sci.* 104, 18392-18397 (2007).
93. E.H. Hwang, S. Adam and S.D. Sarma. Carrier transport in two-dimensional graphene layers. *Phys. Rev. Lett.* 98, 186806 (2007).
94. J.-H. Chen, C. Jang, S. Adam, M.S. Fuhrer, E.D. Williams and M. Ishigami. Charged-impurity scattering in graphene. *Nature Phys.* 4, 378 (2008).
95. J.-H. Chen, C. Jang, S. Xiao, M. Ishigami and M.S. Fuhrer. Intrinsic and extrinsic performance limits of graphene devices on SiO₂. *Nat Nano* 3, 206-209 (2008).
96. M. Jones, W.K. Metzger, T.J. McDonald, C. Engtrakul, R.J. Ellingson, G. Rumbles and M.J. Heben. Extrinsic and intrinsic effects on the excited-state kinetics of single-walled carbon nanotubes. *Nano Lett.* 7, 300-306 (2007).
97. S. Fratini and F. Guinea. Substrate-limited electron dynamics in graphene. *Phys. Rev. B* 77, 195415 (2008).
98. K.I. Bolotin, K.J. Sikes, Z. Jiang, G. Fudenberg, J. Hone, P. Kim and H.L. Stormer. Ultrahigh electron mobility in suspended graphene. *Sol. Stat. Comm.* 146, 351-355 (2008).
99. M.Y. Han, B. Ozyilmaz, Y.B. Zhang and P. Kim. Energy band-gap engineering of graphene nanoribbons. *Phys. Rev. Lett.* 98 (2007).
100. L. Tapasztó, G. Dobrik, P. Lambin and L.P. Biró. Tailoring the atomic structure of graphene nanoribbons by scanning tunnelling microscope lithography. *Nature Nanotech.* 3, 397 - 401 (2008).
101. X. Li, X. Wang, L. Zhang, S. Lee and H. Dai. Chemically derived, ultrasmooth graphene nanoribbon semiconductors. *Science* 319, 1229-1232 (2008).
102. S. Young-Woo, L.C. Marvin and G.L. Steven. Energy Gaps in Graphene Nanoribbons. *Phys. Rev. Lett.* 97, 216803 (2006).
103. V. Barone, O. Hod and G.E. Scuseria. Electronic structure and stability of semiconducting graphene nanoribbons. *Nano Lett.* 6, 2748-2754 (2006).
104. W. Xinran, O. Yijian, L. Xiaolin, W. Hailiang, G. Jing and D. Hongjie. Room-temperature all-semiconducting sub-10-nm graphene nanoribbon field-effect transistors. *Phys. Rev. Lett.* 100, 206803 (2008).
105. S. Stankovich, D.A. Dikin, R.D. Piner, K.A. Kohlhaas, A. Kleinhammes, Y. Jia, Y. Wu, S.T. Nguyen and R.S. Ruoff. Synthesis of graphene-based nanosheets via chemical reduction of exfoliated graphite oxide. *Carbon* 45, 1558-1565 (2007).
106. S. Gilje, S. Han, M. Wang, K.L. Wang and R.B. Kaner. A chemical route to graphene for device applications. *Nano Lett.* 7, 3394-3398 (2007).
107. C. Gomez-Navarro, T.R. Weitz, A.M. Bittner, M. Scolari, A. Mews, M. Burghard and K. Kern. Electronic transport properties of individual chemically reduced graphene oxide sheets. *Nano Lett.* 7, 3499-3503 (2007).
108. X. Wu, M. Sprinkle, X. Li, F. Ming, C. Berger and W.A.d. Heer. Epitaxial-Graphene/Graphene-Oxide Junction: An Essential Step towards Epitaxial Graphene Electronics. *Phys. Rev. Lett.* 101, 026801 (2008).

109. S. Wang, P.-J. Chia, L.-L. Chua, L.-H. Zhao, R.-Q. Png, S. Sivaramakrishnan, M. Zhou, R.G.S. Goh, R.H. Friend, A.T.S. Wee and P.K.H. Ho. Band-like transport in surface-functionalized highly solution-processable graphene nanosheets. *Adv. Mater.* 20, 3440-3446 (2008).
110. C. Lay-Lay, W. Shuai, C. Perq-Jon, C. Lan, Z. Li-Hong, C. Wei, T.S.W. Andrew and K.H.H. Peter. Deoxidation of graphene oxide nanosheets to extended graphenites by "unzipping" elimination. *J. Chem. Phys.* 129, 114702 (2008).
111. I. Jung, D.A. Dikin, R.D. Piner and R.S. Ruoff. Tunable electrical conductivity of individual graphene oxide sheets reduced at "low" temperatures. *Nano Lett.* 8, 4283-4287 (2008).
112. D.C. Elias, R.R. Nair, T.M.G. Mohiuddin, S.V. Morozov, P. Blake, M.P. Halsall, A.C. Ferrari, D.W. Boukhvalov, M.I. Katsnelson, A.K. Geim and K.S. Novoselov. Control of graphene's properties by reversible hydrogenation: evidence for graphane. *Science* 323, 610-613 (2009).
113. Z.C. Wu, Z.H. Chen, X. Du, J.M. Logan, J. Sippel, M. Nikolou, K. Kamaras, J.R. Reynolds, D.B. Tanner, A.F. Hebard and A.G. Rinzler. Transparent, conductive carbon nanotube films. *Science* 305, 1273-1276 (2004).
114. N. Saran, K. Parikh, D.-S. Suh, E. Muoz, H. Kolla and S.K. Manohar. Fabrication and characterization of thin films of single-walled carbon nanotube bundles on flexible plastic substrates. *J. Am. Chem. Soc.* 126, 4462-4463 (2004).
115. Q. Cao, S.-H. Hur, Z.-T. Zhu, Y.G. Sun, C.-J. Wang, M.A. Meitl, M. Shim and J.A. Rogers. Highly bendable, transparent thin-film transistors that use carbon-nanotube-based conductors and semiconductors with elastomeric dielectrics. *Adv. Mater.* 18, 304-309 (2006).
116. A.D. Pasquier, H.E. Unalan, A. Kanwal, S. Miller and M. Chhowalla. Conducting and transparent single-wall carbon nanotube electrodes for polymer-fullerene solar cells. *Appl. Phys. Lett.* 87, 203511 (2005).
117. M.W. Rowell, M.A. Topinka, M.D. McGehee, H.J. Prall, G. Dennler, N.S. Sariciftci, L.B. Hu and G. Gruner. Organic solar cells with carbon nanotube network electrodes. *Appl. Phys. Lett.* 88, 233506 (2006).
118. J.v.d. Lagemaat, T.M. Barnes, G. Rumbles, S.E. Shaheen, T.J. Coutts, C. Weeks, I. Levitsky, J. Peltola and P. Glatkowski. Organic solar cells with carbon nanotubes replacing $\text{In}_2\text{O}_3:\text{Sn}$ as the transparent electrode. *Appl. Phys. Lett.* 88, 233503 (2006).
119. T. Radhouane Bel Hadj, B. Takayuki, O. Yutaka and T. Yasutaka. Tin doped indium oxide thin films: Electrical properties. *J. Appl. Phys.* 83, 2631-2645 (1998).
120. H. Kim, C.M. Gilmore, A. Pique, J.S. Horwitz, H. Mattoussi, H. Murata, Z.H. Kafafi and D.B. Chrisey. Electrical, optical, and structural properties of indium--tin--oxide thin films for organic light-emitting devices. *J. Appl. Phys.* 86, 6451-6461 (1999).
121. S.-S. Sun and N.S. Sariciftci. Organic Photovoltaics: Mechanism, Materials, And Devices (Taylor & Francis, London, 2005).
122. G. Fanchini, H.E. Unalan and M. Chhowalla. Modification of transparent and conducting single wall carbon nanotube thin films via bromine functionalization. *Appl. Phys. Lett.* 90, 092114 (2007).

123. D. H. Zhang, K. Ryu, X. L. Liu, E. Polikarpov, J. Ly, M.E. Thompson and C.W. Zhou. Transparent, conductive, and flexible carbon nanotube films and their application in organic light-emitting diodes. *Nano Lett.* 6, 1880-1886 (2006).
124. G. Fanchini, H.E. Unalan and M. Chhowalla. Optoelectronic properties of transparent and conducting single-wall carbon nanotube thin films. *Appl. Phys. Lett.* 88 (2006).
125. H.E. Unalan. in *Materials Science and Engineering* (Rutgers University, Piscataway, New Jersey, 2006).
126. See www.carbonsolution.com.
127. B.J. Landi, C.D. Cress, C.M. Evans and R.P. Raffaele. Thermal Oxidation Profiling of Single-Walled Carbon Nanotubes. *Chem. Mater.* 17, 6819-6834 (2005).
128. B.B. Parekh, G. Fanchini, G. Eda and M. Chhowalla. Improved conductivity of transparent single-wall carbon nanotube thin films via stable postdeposition functionalization. *Appl. Phys. Lett.* 90, 121913 (2007).
129. N.B. Colthup, L.H. Daly and S.E. Wiberley. *Introduction to Infrared and Raman Spectroscopy* (Academic Press, Boston, 1990).
130. U.J. Kim, X.M. Liu, C.A. Furtado, G. Chen, R. Saito, J. Jiang, M.S. Dresselhaus and P.C. Eklund. Infrared-active vibrational modes of single-walled carbon nanotubes. *Phys. Rev. Lett.* 95, 157402 (2005).
131. S.C. Tsang, Y.K. Chen, P.J.F. Harris and M.L.H. Green. A simple chemical method of opening and filling carbon nanotubes. *Nature* 372, 159-162 (1994).
132. H. Hu, B. Zhao, M.E. Itkis and R.C. Haddon. Nitric acid purification of single-walled carbon nanotubes. *J. Phys. Chem. B* 107, 13838-13842 (2003).
133. J. Robertson. Diamond-like amorphous carbon. *Mater. Sci. Eng. R* 37, 129-281 (2002).
134. E.H. Huntress. *Preparation, Properties, Chemical Behavior, & Identification of Organic Chlorine Compounds* (Wiley, New York, 1948).
135. U. Dettlaff-Weglikowska, V. Skakalova, R. Graupner, S.H. Jhang, B.H. Kim, H.J. Lee, L. Ley, Y.W. Park, S. Berber, D. Tomanek and S. Roth. Effect of SOCl_2 treatment on electrical and mechanical properties of single-wall carbon nanotube networks. *J. Am. Chem. Soc.* 127, 5125-5131 (2005).
136. C.-W. Chen and M.-H. Lee. Ab initio calculations of dimensional and adsorbate effects on the workfunction of single-walled carbon nanotube. *Diam. Relat. Mater.* 12, 565-571 (2003).
137. H.-Z. Geng, K.K. Kim, K.P. So, Y.S. Lee, Y. Chang and Y.H. Lee. Effect of acid treatment on carbon nanotube-based flexible transparent conducting films. *J. Am. Chem. Soc.* 129, 7758-7759 (2007).
138. V.C. Moore, M.S. Strano, E.H. Haroz, R.H. Hauge, R.E. Smalley, J. Schmidt and Y. Talmon. Individually suspended single-walled carbon nanotubes in various surfactants. *Nano Lett.* 3, 1379-1382 (2003).
139. M.S. Arnold, A.A. Green, J.F. Hulvat, S.I. Stupp and M.C. Hersam. Sorting carbon nanotubes by electronic structure using density differentiation. *Nature Nanotech.* 1, 60-65 (2006).
140. P. Beecher, P. Servati, A. Rozhin, A. Colli, V. Scardaci, S. Pisana, T. Hasan, A.J. Flewitt, J. Robertson, G.W. Hsieh, F.M. Li, A. Nathan, A.C. Ferrari and W.I. Milne.

- Ink-jet printing of carbon nanotube thin film transistors. *J. Appl. Phys.* 102, 043710 (2007).
141. M.A. Meitl, Z. Yangxin, A. Gaur, J. Seokwoo, M.L. Usrey, M.S. Strano and J.A. Rogers. Solution casting and transfer printing single-walled carbon nanotube films. *Nano Letters* 4, 1643-7 (2004).
 142. S.H. Hur, O.O. Park and J.A. Rogers. Extreme bendability of single-walled carbon nanotube networks transferred from high-temperature growth substrates to plastic and their use in thin-film transistors. *Appl. Phys. Lett.* 86, 243502 (2005).
 143. Y.X. Zhou, L.B. Hu and G. Gruner. A method of printing carbon nanotube thin films. *Appl. Phys. Lett.* 88, 123109 (2006).
 144. J. Li, L. Hu, L. Wang, Y. Zhou, G. Gruner and T.J. Marks. Organic light-emitting diodes having carbon nanotube anodes. *Nano Lett.* 6, 2472-2477 (2006).
 145. E. Artukovic, M. Kaempgen, D.S. Hecht, S. Roth and G. Gruner. Transparent and flexible carbon nanotube transistors. *Nano Lett.* 5, 757-760 (2005).
 146. J.A. Misewich, R. Martel, P. Avouris, J.C. Tsang, S. Heinze and J. Tersoff. Electrically induced optical emission from a carbon nanotube FET. *Science* 300, 783-786 (2003).
 147. A. Star, Y. Lu, K. Bradley and G. Gruner. Nanotube optoelectronic memory devices. *Nano Lett.* 4, 1587-1591 (2004).
 148. J. Chen, V. Perebeinos, M. Freitag, J. Tsang, Q. Fu, J. Liu and P. Avouris. Bright infrared emission from electrically induced excitons in carbon nanotubes. *Science* 310, 1171-1174 (2005).
 149. B.J. Landi, H.J. Ruf, J.J. Worman and R.P. Raffaele. Effects of alkyl amide solvents on the dispersion of single-wall carbon nanotubes. *J. Phys. Chem. B* 108, 17089-17095 (2004).
 150. M.J. O'Connell, S. Sivaram and S.K. Doorn. Near-infrared resonance Raman excitation profile studies of single-walled carbon nanotube intertube interactions: A direct comparison of bundled and individually dispersed HiPco nanotubes. *Phys. Rev. B* 69 (2004).
 151. D.W. Schaefer, J. Zhao, J.M. Brown, D.P. Anderson and D.W. Tomlin. Morphology of dispersed carbon single-walled nanotubes. *Chem. Phys. Lett.* 375, 369-375 (2003).
 152. H. Wang, W. Zhou, D.L. Ho, K.I. Winey, J.E. Fischer, C.J. Glinka and E.K. Hobbie. Dispersing single-walled carbon nanotubes with surfactants: A small angle neutron scattering study. *Nano Lett.* 4, 1789-1793 (2004).
 153. S. Badaire, P. Poulin, M. Maugey and C. Zakri. In situ measurements of nanotube dimensions in suspensions by depolarized dynamic light scattering. *Langmuir* 20, 10367-10370 (2004).
 154. V. Nicolosi, D. Vrbancic, A. Mrzel, J. McCauley, S. O'Flaherty, C. McGuinness, G. Compagnini, D. Mihailovic, W.J. Blau and J.N. Coleman. Solubility of Mo₆S₄.5I₄.5 nanowires in common solvents: a sedimentation study. *J. Phys. Chem. B* 109, 7124-7133 (2005).
 155. M. Tory. Sedimentation of small particles in a viscous fluid (Computational Mechanics Publications, Southampton, 1996).
 156. C.F. Bohren and D.R. Huffman. Absorption and scattering of light by small particles (Wiley, Weinheim, Germany, 1998).

157. J.A. Fagan, J.R. Simpson, B.J. Landi, L.J. Richter, I. Mandelbaum, V. Bajpai, D.L. Ho, R. Raffaele, A.R.H. Walker, B.J. Bauer and E.K. Hobbie. Dielectric response of aligned semiconducting single-wall nanotubes. *Phys. Rev. Lett.* 98 (2007).
158. N. Pimparkar, J. Guo and M.A. Alam. Performance assessment of subpercolating nanobundle network thin-film transistors by an analytical model. *IEEE Trans. Elec. Dev.* 54, 637-644 (2007).
159. C. Kocabas, N. Pimparkar, O. Yesilyurt, S.J. Kang, M.A. Alam and J.A. Rogers. Experimental and theoretical studies of transport through large scale, partially aligned arrays of single-walled carbon nanotubes in thin film type transistors. *Nano Letters* 7, 1195-1202 (2007).
160. Y. Hernandez, V. Nicolosi, M. Lotya, F.M. Blighe, Z. Sun, S. De, I.T. McGovern, B. Holland, M. Byrne, Y.K. Gun'Ko, J.J. Boland, P. Niraj, G. Duesberg, S. Krishnamurthy, R. Goodhue, J. Hutchison, V. Scardaci, A.C. Ferrari and J.N. Coleman. High-yield production of graphene by liquid-phase exfoliation of graphite. *Nature Nanotech.* 3, 563-568 (2008).
161. C. Berger, Z.M. Song, X.B. Li, X.S. Wu, N. Brown, C. Naud, D. Mayo, T.B. Li, J. Hass, A.N. Marchenkov, E.H. Conrad, P.N. First and W.A. de Heer. Electronic confinement and coherence in patterned epitaxial graphene. *Science* 312, 1191-1196 (2006).
162. C. Berger, Z.M. Song, T.B. Li, X.B. Li, A.Y. Ogbazghi, R. Feng, Z.T. Dai, A.N. Marchenkov, E.H. Conrad, P.N. First and W.A. de Heer. Ultrathin epitaxial graphite: 2D electron gas properties and a route toward graphene-based nanoelectronics. *J. Phys. Chem. B* 108, 19912-19916 (2004).
163. J. Coraux, A.T. N'Diaye, C. Busse and T. Michely. Structural Coherency of Graphene on Ir(111). *Nano Lett.* 8, 565-570 (2008).
164. P.W. Sutter, J.-I. Flege and E.A. Sutter. Epitaxial graphene on ruthenium. *Nature Mater.* 7, 406-411 (2008).
165. A. Reina, X. Jia, J. Ho, D. Nezich, H. Son, V. Bulovic, M.S. Dresselhaus and J. Kong. Large area, few-layer graphene films on arbitrary substrates by chemical vapor deposition. *Nano Lett.* 9, 30-35 (2009).
166. K.S. Kim, Y. Zhao, H. Jang, S.Y. Lee, J.M. Kim, K.S. Kim, J.-H. Ahn, P. Kim, J.-Y. Choi and B.H. Hong. Large-scale pattern growth of graphene films for stretchable transparent electrodes. *Nature* 457, 706-710 (2009).
167. G. Eda, G. Fanchini and M. Chhowalla. Large-area ultrathin films of reduced graphene oxide as a transparent and flexible electronic material. *Nature Nanotech.* 3, 270-274 (2008).
168. J.T. Paci, T. Belytschko and G.C. Schatz. Computational studies of the structure, behavior upon heating, and mechanical properties of graphite oxide. *J. Phys. Chem. C* 111, 18099-18111 (2007).
169. J. Chattopadhyay, A. Mukherjee, C.E. Hamilton, J. Kang, S. Chakraborty, W. Guo, K.F. Kelly, A.R. Barron and W.E. Billups. Graphite epoxide. *J. Am. Chem. Soc.* 130, 5414-5415 (2008).
170. D.W. Boukhvalov and M.I. Katsnelson. Modeling of graphite oxide. *J. Am. Chem. Soc.* 130, 10697-10701 (2008).
171. A. Lerf, H. He, M. Forster and J. Klinowski. Structure of graphite oxide revisited. *J. Phys. Chem. B* 102, 4477-4482 (1998).

172. T. Szabo, O. Berkesi, P. Forgo, K. Josepovits, Y. Sanakis, D. Petridis and I. Dekany. Evolution of surface functional groups in a series of progressively oxidized graphite oxides. *Chem. Mater.* 18, 2740-2749 (2006).
173. H. He, J. Klinowski, M. Forster and A. Lerf. A new structural model for graphite oxide. *Chem. Phys. Lett.* 287, 53-56 (1998).
174. Y. Si and E.T. Samulski. Synthesis of water soluble graphene. *Nano Lett.* 8, 1679-1682 (2008).
175. D. Li, M.B. Muller, S. Gilje, R.B. Kaner and G.G. Wallace. Processable aqueous dispersions of graphene nanosheets. *Nature Nanotech.* 3, 101-105 (2008).
176. J.T. Robinson, F.K. Perkins, E.S. Snow, Z. Wei and P.E. Sheehan. Reduced graphene oxide molecular sensors. *Nano Lett.* 8, 3137-3140 (2008).
177. J.T. Robinson, M. Zalalutdinov, J.W. Baldwin, E.S. Snow, Z. Wei, P. Sheehan and B.H. Houston. Wafer-scale reduced graphene oxide films for nanomechanical devices. *Nano Lett.* 8, 3441-3445 (2008).
178. H.A. Becerill, J. Mao, Z. Liu, R.M. Stoltenberg, Z. Bao and Y. Chen. Evaluation of Solution-Processed Reduced Graphene Oxide Films as Transparent Conductors. *ACS Nano* 2, 463-470 (2008).
179. V.C. Tung, M.J. Allen, Y. Yang and R.B. Kaner. High-throughput solution processing of large-scale graphene. *Nature Nanotech.* 4, 25-29 (2009).
180. M. Hirata, T. Gotou, S. Horiuchi, M. Fujiwara and M. Ohba. Thin-film particles of graphite oxide 1: High-yield synthesis and flexibility of the particles. *Carbon* 42, 2929-2937 (2004).
181. M.J. McAllister, J.L. LiO, D.H. Adamson, H.C. Schniepp, A.A. Abdala, J. Liu, M. Herrera-Alonso, D.L. Milius, R. CarO, R.K. Prud'homme and I.A. Aksay. Single sheet functionalized graphene by oxidation and thermal expansion of graphite. *Chem. Mater.* 19, 4396-4404 (2007).
182. P. Blake, E.W. Hill, A.H.C. Neto, K.S. Novoselov, D. Jiang, R. Yang, T.J. Booth and A.K. Geim. Making graphene visible. *Appl. Phys. Lett.* 91, 063124 (2007).
183. A.K. Geim and P. Kim. Carbon wonderland. *Sci. Am.* 298, 68-75 (2008).
184. I. Jung, M. Vaupel, M. Pelton, R. Piner, D.A. Dikin, S. Stankovich, J. An and R.S. Ruoff. Characterization of Thermally Reduced Graphene Oxide by Imaging Ellipsometry. *J. Phys. Chem. C* 112, 8499-8506 (2008).
185. X. Wang, L. Zhi and K. Mullen. Transparent, conductive graphene electrodes for dye-sensitized solar cells. *Nano Lett.* 8, 323-327 (2007).
186. S. Wang, P.-J. Chia, L.-L. Chua, L.-H. Zhao, R.-Q. Png, S. Sivaramakrishnan, M. Zhou, R.G.-S. Goh, R.H. Friend, A.T.-S. Wee and P.K.-H. Ho. Band-like transport in surface-functionalized highly solution-processable graphene nanosheets. *Adv. Mater.* 20, 3440-3446 (2008).
187. S. Watcharotone, D.A. Dikin, S. Stankovich, R. Piner, I. Jung, G.H.B. Dommett, G. Evmenenko, S.E. Wu, S.F. Chen, C.P. Liu, S.T. Nguyen and R.S. Ruoff. Graphene-silica composite thin films as transparent conductors. *Nano Lett.* 7, 1888-1892 (2007).
188. S. Stankovich, R.D. Piner, X.Q. Chen, N.Q. Wu, S.T. Nguyen and R.S. Ruoff. Stable aqueous dispersions of graphitic nanoplatelets via the reduction of exfoliated graphite oxide in the presence of poly(sodium 4-styrenesulfonate). *J. Mater. Chem.* 16, 155-158 (2006).

189. S. Stankovich, R. Piner, S.T. Nguyen and R.S. Ruoff. Synthesis and exfoliation of isocyanate-treated graphene oxide nanoplatelets. *Carbon* 44, 3342-3347 (2006).
190. C. Hontoria-Lucas, A.J. Loez-Peinado, J.d.D. Loez-Gonzalez, M.L. Rojas-Cervantes and R.M. Martin-Aranda. Study of oxygen-containing groups in a series of graphite oxides: Physical and chemical characterization. *Carbon* 33, 1585-1592 (1995).
191. D. Yang, A. Velamakanni, G.a. Bozoklu, S. Park, M. Stoller, R.D. Piner, S. Stankovich, I. Jung, D.A. Field, C.A. Ventrice Jr and R.S. Ruoff. Chemical analysis of graphene oxide films after heat and chemical treatments by X-ray photoelectron and Micro-Raman spectroscopy. *Carbon* 47, 145-152 (2009).
192. S. Tanuma, C.J. Powell and D.R. Penn. Calculations of electron inelastic mean free paths. V. Data for 14 organic compounds over the 50-2000 eV range. *Surf. Interface Anal.* 21, 165-176 (1994).
193. D.-Q. Yang and E. Sacher. Carbon 1s X-ray photoemission line shape analysis of highly oriented pyrolytic graphite: The Influence of structural damage on peak asymmetry. *Langmuir* 22, 860-862 (2006).
194. W. Cai, R.D. Piner, F.J. Stadermann, S. Park, M.A. Shaibat, Y. Ishii, D. Yang, A. Velamakanni, S.J. An, M. Stoller, J. An, D. Chen and R.S. Ruoff. Synthesis and solid-state NMR structural characterization of ^{13}C -labeled graphite oxide. *Science* 321, 1815-1817 (2008).
195. A.C. Ferrari and J. Robertson. Interpretation of Raman spectra of disordered and amorphous carbon. *Phys. Rev. B* 61, 14095-14107 (2000).
196. A.C. Ferrari, J.C. Meyer, V. Scardaci, C. Casiraghi, M. Lazzeri, F. Mauri, S. Piscanec, D. Jiang, K.S. Novoselov, S. Roth and A.K. Geim. Raman spectrum of graphene and graphene layers. *Phys. Rev. Lett.* 97, 187401 (2006).
197. J.A. Robinson, M. Wetherington, J.L. Tedesco, P.M. Campbell, X. Weng, J. Stitt, M.A. Fanton, E. Frantz, D. Snyder, B.L. VanMil, G.G. Jernigan, R.L. Myers-Ward, J. Charles R. Eddy and D.K. Gaskill. Correlating Raman spectral signatures with carrier mobility in epitaxial graphene: A guide to achieving high mobility on the wafer scale. <arXiv:0902.4821v1> (2009).
198. A.C. Ferrari and J. Robertson. Raman spectroscopy of amorphous, nanostructured, diamond-like carbon, and nanodiamond. *Phil.l Trans. R. Soc. A* 362, 2477-2512 (2004).
199. F. Tuinstra and J.L. Koenig. Raman spectrum of graphite. *J. Chem. Phys.* 53, 1126-1130 (1970).
200. G.D. M. A. Pimenta, M. S. Dresselhaus, L. G. Cançado, A. Jorio and R. Saito. Studying disorder in graphite-based systems by Raman spectroscopy. *Phys. Chem. Chem. Phys.* 9, 1276 - 1290 (2007).
201. M. Chhowalla, A.C. Ferrari, J. Robertson and G.A.J. Amaratunga. Evolution of sp^2 bonding with deposition temperature in tetrahedral amorphous carbon studied by Raman spectroscopy. *Appl. Phys. Lett.* 76, 1419-1421 (2000).
202. F. Banhart. Irradiation effects in carbon nanostructures. *Rep. Prog. Phys.* 62, 1181-1221 (1999).
203. S.R.S. Soares, N.M. Balzaretti, R.P. Livi, A.S. Pereira and J.A.H. da Jornada. High pressure annealing of defects induced by ion implantation on graphite. *Nucl. Inst. Meth. Phys. B* 175-177, 474-478 (2001).

204. X. Li, G. Zhang, X. Bai, X. Sun, X. Wang, E. Wang and H. Dai. Highly conducting graphene sheets and Langmuir–Blodgett films. *Nature Nanotech.* 3, 538-542 (2008).
205. J.C. Meyer, A.K. Geim, M.I. Katsnelson, K.S. Novoselov, T.J. Booth and S. Roth. The structure of suspended graphene sheets. *Nature* 446, 60-63 (2007).
206. J.C. Meyer, C.O. Girit, M.F. Crommie and A. Zettl. Imaging and dynamics of light atoms and molecules on graphene. *Nature* 454, 319-322 (2008).
207. G. Wang, J. Yang, J. Park, X. Gou, B. Wang, H. Liu and J. Yao. Facile Synthesis and Characterization of Graphene Nanosheets. *J. Phys. Chem. C* 112, 8192-8195 (2008).
208. R.F. Egerton. *Electron Energy Loss Spectroscopy in the Electron Microscope* (Plenum Press, New York, 1996).
209. D.A. Muller, D.J. Singh and J. Silcox. Connections between the electron-energy-loss spectra, the local electronic structure, and the physical properties of a material: A study of nickel aluminum alloys. *Phys. Rev. B* 57, 8181 (1998).
210. K.A. Mkhoyan, J. Silcox, E.S. Alldredge, N.W. Ashcroft, H. Lu, W.J. Schaff and L.F. Eastman. Measuring electronic structure of wurtzite InN using electron energy loss spectroscopy. *Appl. Phys. Lett.* 82, 1407-1409 (2003).
211. J. Daniels, C.V. Festenberg, H. Raether and K. Zeppenfeld. *Springer Tracts in Modern Physics* (ed. Hohler, G.) (Springer-Verlag, Berlin, 1970).
212. D.R. Lide (ed.) *CRC Handbook of Chemistry and Physics* (Plenum, New York, 2004).
213. P.E. Batson. Carbon 1s near-edge-absorption fine structure in graphite. *Phys. Rev. B* 48, 2608 (1993).
214. D.A. Muller, T. Sorsch, S. Moccio, F.H. Baumann, K. Evans-Lutterodt and G. Timp. The electronic structure at the atomic scale of ultrathin gate oxides. *Nature* 399, 758-761 (1999).
215. W.H. Press, S.A. Teukolsky, W.T. Vetterling and B.P. Flannery. *Numerical Recipes in C++* (Cambridge University Press, Cambridge, England, 2003).
216. S.D. Berger, D.R. McKenzie and P.J. Martin. EELS analysis of vacuum arc-deposited diamond-like films. *J. Philos. Mag. Lett.* 57, 285-290 (1988).
217. J.C. Jerome, P.D. James, B. John and C.L. Joyce. Sputter deposition of dense diamond-like carbon films at low temperature. *Appl. Phys. Lett.* 58, 466-468 (1991).
218. H. Raether. in *Springer Tracts in Modern Physics* (ed. Hohler, G.) (Berlin, 1980).
219. K.A. Mkhoyan, T. Babinec, S.E. Maccagnano, E.J. Kirkland and J. Silcox. Separation of bulk and surface-losses in low-loss EELS measurements in STEM. *Ultramicroscopy* 107, 345-355 (2007).
220. T. Eberlein, U. Bangert, R.R. Nair, R. Jones, M. Gass, A.L. Bleloch, K.S. Novoselov, A. Geim and P.R. Briddon. Plasmon spectroscopy of free-standing graphene films. *Phys. Rev. B* 77, 233406 (2008).
221. G.E. Pike and C.H. Seager. Percolation and conductivity: A computer study. I. *Phys. Rev. B* 10, 1421 (1974).
222. D.S. McLachlan, C. Chitame, C. Park, K.E. Wise, S.E. Lowther, P.T. Lillehei, E.J. Siochi and J.S. Harrison. AC and DC percolative conductivity of single wall carbon

- nanotube polymer composites. *J. Polym. Sci. B: Polym. Phys.* 43, 3273-3287 (2005).
223. I. Balberg. Limits on the continuum-percolation transport exponents. *Phys. Rev. B* 57, 13351 (1998).
 224. S. Gijie, S. Han, M. Wang, K.L. Wang and R.B. Kaner. A chemical route to graphene for device applications. *Nano Lett.* 7, 3394-3398 (2007).
 225. Y. Zhang, J.P. Small, W.V. Pontius and P. Kim. Fabrication and electric-field-dependent transport measurements of mesoscopic graphite devices. *Appl. Phys. Lett.* 86, 073104 (2005).
 226. S.V. Morozov, K.S. Novoselov, M.I. Katsnelson, F. Schedin, D.C. Elias, J.A. Jaszczak and A.K. Geim. Giant Intrinsic carrier mobilities in graphene and its bilayer. *Phys. Rev. Lett.* 100, 016602 (2008).
 227. G. Eda, Y.-Y. Lin, S. Miller, C.-W. Chen, W.-F. Su and M. Chhowalla. Transparent and conducting electrodes for organic electronics from reduced graphene oxide. *Appl. Phys. Lett.* 92, 233305 (2008).
 228. T. Ramanathan, A.A. Abdala, S. Stankovich, D.A. Dikin, M. Herrera-Alonso, R.D. Piner, D.H. Adamson, H.C. Schniepp, X. Chen, R.S. Ruoff, S.T. Nguyen, I.A. Aksay, R.K. Prud'Homme and L.C. Brinson. Functionalized graphene sheets for polymer nanocomposites. *Nature Nanotech.* 3, 327-331 (2008).
 229. R. Verdejo, F. Barroso-Bujans, M.A. Rodriguez-Perez, J.A.d. Saja and M.A. Lopez-Manchado. Functionalized graphene sheet filled silicone foam nanocomposites. *J. Mater. Chem.* 18, 2221-2226 (2008).
 230. A. Yu, P. Ramesh, M.E. Itkis, E. Bekyarova and R.C. Haddon. Graphite nanoplatelet-epoxy composite thermal interface materials. *J. Phys. Chem. C* 111, 7565-7569 (2007).
 231. N. Liu, F. Luo, H. Wu, Y. Liu, C. Zhang and J. Chen. One-step ionic-liquid-assisted electrochemical synthesis of ionic-liquid-functionalized graphene sheets directly from graphite. *Adv. Funct. Mater.* 18, 1518-1525 (2008).
 232. E.W. Hill, A.K. Geim, K. Novoselov, F. Schedin and P. Blake. Graphene Spin Valve Devices. *IEEE Trans. Magn.* 42, 2694 (2006).
 233. X. Sun, Z. Liu, K. Welsher, J.T. Robinson, A. Goodwin, S. Zaric and H. Dai. Nano-graphene oxide for cellular imaging and drug delivery. *Nano Res.* 1, 203-212 (2008).
 234. T. Utsumi. Microelectronics: What's new and exciting. *IEEE Trans. Elec. Dev.* 38, 2276-2283 (1991).
 235. C. Wang, A. Garcia, D.C. Ingram, M. Lake and M.E. Kordesche. Cold field emission from CVD diamond films observed in emission electron microscopy. *Electron. Lett.* 27, 1459-1461 (1991).
 236. K. Okano, S. Koizumi, S.R.P. Silva and G.A.J. Amaratunga. Low-threshold cold cathodes made of nitrogen-doped chemical-vapor-deposited diamond. *Nature* 381, 140-141 (1996).
 237. G.A.J. Amaratunga and S.R.P. Silva. Nitrogen containing hydrogenated amorphous carbon for thin-film field emission cathodes. *Appl. Phys. Lett.* 68, 2529 (1996).
 238. W.A. De Heer, A. Chatelain and D. Ugarte. A carbon nanotube field-emission electron source. *Science* 270, 1179-1180 (1995).

239. A.G. Rinzier, J.H. Hafner, P. Nikolaev, P. Nordlander, D.T. Colbert, R.E. Smalley, L. Lou, S.G. Kim and D. Tomanek. Unraveling nanotubes: field emission from an atomic wire. *Science* 269, 1550-1553 (1995).
240. K.B.K. Teo, M. Chhowalla, G.A.J. Amaratunga, W.I. Milne, G. Pirio, P. Legagneux, F. Wyczisk, D. Pribat and D.G. Hasko. Field emission from dense, sparse, and patterned arrays of carbon nanofibers. *Appl. Phys. Lett.* 80, 2011-2013 (2002).
241. Y. Saito, K. Hamaguchi, T. Nishino, K. Hata, K. Tohji, A. Kasuya and Y. Nishina. Field emission patterns from single-walled carbon nanotubes. *Jpn. J. Appl. Phys.* 36, L1340-L1342 (1997).
242. S.G. Wang, J.J. Wang, P. Miraldo, M.Y. Zhu, R. Outlaw, K. Hou, X. Zhao, B.C. Holloway, D. Manos, T. Tyler, O. Shenderova, M. Ray, J. Dalton and G. McGuire. High field emission reproducibility and stability of carbon nanosheets and nanosheet-based backgated triode emission devices. *Appl. Phys. Lett.* 89, 183103 (2006).
243. K. Hou, R.A. Outlaw, S. Wang, M. Zhu, R.A. Quinlan, D.M. Manos, M.E. Kordesch, U. Arp and B.C. Holloway. Uniform and enhanced field emission from chromium oxide coated carbon nanosheets. *Appl. Phys. Lett.* 92, 133112 (2008).
244. J. Wang and T. Ito. CVD growth and field emission characteristics of nano-structured films composed of vertically standing and mutually intersectiong nano-carbon sheets. *Diam. Relat. Mater.* 16, 589-593 (2007).
245. S. Watcharotone, R.S. Ruoff and F.H. Read. Possibilities for graphene for field emission: modeling studies using the BEM. *Phys. Procedia* 1, 71-75 (2008).
246. S. Bajic and R.V. Latham. Enhanced cold-cathode emission using composite resin-carbon coatings. *J. Phys. D: Appl. Phys.* 21, 200-204 (1988).
247. A.P. Burden, H.E. Bishop, M. Brierley, J.M. Friday, C. Hood, P.G.A. Jones, A.Y. Kyazov, W. Lee, R.J. Riggs, V.L. Shaw and R.A. Tuck. Field emitting inks for consumer-priced broad-area flat-panel displays. *J. Vac. Sci. Technol. B* 18, 900-904 (2000).
248. P.C.P. Watts, S.M. Lyth, E. Mendoza and S.R.P. Silva. Polymer supported carbon nanotube arrays for field emission and sensor devices. *Appl. Phys. Lett.* 89, 103113 (2006).
249. J.D. Carey and S.R.P. Silva. Current-induced conditioning of hydrogenated amorphous carbon thin films for field emission. *Diam. Rel. Mater.* 10, 873-877 (2001).
250. R. Riccardo, C. Aldo Di, F. Angelamaria, O. Silvia, T. Maria Letizia, S. Antonino, F. Roberta, R. Alessandro and V. Felix Jimenex. Field emission from silicon nanowires: Conditioning and stability. *J. Appl. Phys.* 102, 054906 (2007).
251. Q.H. Wang, T.D. Corrigan, J.Y. Dai, R.P.H. Chang and A.R. Krauss. Field emission from nanotube bundle emitters at low fields. *Appl. Phys. Lett.* 70, 3308 (1997).
252. I. Musa, D.A.I. Munindrasdasa, G.A.J. Amaratunga and W. Eccleston. Ultra-low-threshold fieldemission from conjugated polymers. *Nature* 395, 362 (1998).
253. W. Zhua, C. Bower, O. Zhou, G. Kochanski and S. Jin. Large current density from carbon nanotube field emitters. *Appl. Phys. Lett.* 75, 873 (1999).

254. N.L. Rupesinghe, M. Chhowalla, K.B.K. Teo and G.A.J. Amaratunga. Field emission vacuum power switch using vertically aligned carbon nanotubes. *J. Vac. Sci. Technol. B* 21, 338-343 (2003).
255. R. Miller, Y.Y. Lau and J.H. Booske. Electric field distribution on knife-edge field emitters. *Appl. Phys. Lett.* 91, 074105 (2007).
256. L. Schachter. Analytic expression for triple-point electron emission from an ideal edge. *Appl. Phys. Lett.* 72, 421 (1998).
257. N.M. Jordan, Y.Y. Lau, D.M. French, R.M. Gilgenbach and P. Pengvanich. Electric field and electron orbits near a triple point. *J. Appl. Phys.* 102, 033301 (2007).
258. I. Alexandrou, E. Kymakis and G.A.J. Amaratunga. Polymer–nanotube composites: Burying nanotubes improves their field emission properties. *Appl. Phys. Lett.* 80, 1435 (2002).
259. R.H. Fowler and L. Nordheim. Electron emission in intense fields. *Proc. R. Soc. Lond. A* 119, 173-181 (1928).
260. J.D. Levine. Statistical analysis of field emitter emissivity: Application to flat displays. *J. Vac. Sci. Technol. B* 13, 553-557 (1995).
261. K.H. Bayliss and R.V. Latham. An analysis of field-induced hot-electron emission from metal-insulator microstructures on broad-area high-voltage electrodes. *Proc. R. Soc. Lond. A* 403, 285-311 (1986).
262. R.G. Forbes. Low-macroscopic-field electron emission from carbon films and other electrically nanostructured heterogeneous materials: hypotheses about emission mechanism. *Sol. Stat. Comm.* 45, 779-808 (2001).
263. R. Krupke, F. Hennrich, H.v. Lohneysen and M.M. Kappes. Separation of metallic from semiconducting single-walled carbon nanotubes. *Science* 301, 344-347 (2003).
264. D.H. Shin, J.-E. Kim, H.C. Shim, J.-W. Song, J.-H. Yoon, J. Kim, S. Jeong, J. Kang, S. Baik and C.-S. Han. Continuous extraction of highly pure metallic single-walled carbon nanotubes in a microfluidic channel. *Nano Lett.* 8, 4380-4385 (2008).
265. T. Tanaka, H. Jin, Y. Miyata, S. Fujii, H. Suga, Y. Naitoh, T. Minari, T. Miyadera, K. Tsukagoshi and H. Kataura. Simple and scalable gel-based separation of metallic and semiconducting carbon nanotubes. *Nano Lett.*, In press.
266. M.S. Arnold, S.I. Stupp and M.C. Hersam. Enrichment of single-walled carbon nanotubes by diameter in density gradients. *Nano Lett.* 5, 713-718 (2005).
267. A.A. Green and M.C. Hersam. Colored semitransparent conductive coatings consisting of monodisperse metallic single-walled carbon nanotubes. *Nano Lett.* 8, 1417-1422 (2008).
268. M.C. LeMieux, M. Roberts, S. Barman, Y.W. Jin, J.M. Kim and Z. Bao. Self-sorted, aligned nanotube networks for thin-film transistors. *Science* 321, 101-104 (2008).
269. S. Reich, C. Thomsen and P. Ordejon. Electronic band structure of isolated and bundled carbon nanotubes. *Phys. Rev. B* 65 (2002).
270. L. Zhengtang, M.V. Patrick, J.M. Eugene, A.T.C. Johnson and M.K. James. Photoluminescence and band gap modulation in graphene oxide. *Appl. Phys. Lett.* 94, 111909 (2009).
271. S. Park, J. An, I. Jung, R.D. Piner, S.J. An, X. Li, A. Velamakanni and R.S. Ruoff. Colloidal suspensions of highly reduced graphene oxide in a wide variety of organic solvents. *Nano Lett.*, In press.

272. X. Fan, W. Peng, Y. Li, X. Li, S. Wang, G. Zhang and F. Zhang. Deoxygenation of exfoliated graphite oxide under alkaline conditions: a green route to graphene preparation. *Adv. Mater.* 20, 4490-4493 (2008).
273. Y. Liang, D. Wu, X. Feng and K. Mullen. Dispersion of graphene sheets in organic solvent supported by ionic interactions. *Adv. Mater.*, In press (2009).

ACKNOWLEDGEMENT OF PREVIOUS PUBLICATIONS

This thesis dissertation is composed in part of independent articles that have been published previously, are currently in press, or under review. Specifically, part of the material presented in Chapters 4 and 5 are results from (Eda *et al.* *J. Appl. Phys.* 203, 093118 (2008)), (Parekh *et al.* *Appl. Phys. Lett.* 90, 121913 (2006)), and (Lin *et al.* *Org. Elec.* Under review). Chapter 6 and 7 are composed in part of results presented in (Eda *et al.* *Nature Nanotech.* 3, 270 (2008)), (Eda *et al.* *Appl. Phys. Lett.* 92, 233305 (2008)), (Mkhoyan *et al.* *Nano Lett.* 9, 1058 (2009)), and (Mattevi *et al.* *Adv. Funct. Mater.* (2009) In press.). Similarly, part of the results described in Chapter 8 have been previously published in (Eda and Chhowalla, *Nano Lett.* 9, 814 (2009)) and (Eda *et al.* *Appl. Phys. Lett.* 93, 233502 (2008)).

CURRICULUM VITA

Goki Eda

- Education** **Rutgers – The State University of New Jersey**, Piscataway, NJ
 PhD candidate in Materials Science and Engineering, October 2009.
Worcester Polytechnic Institute, Worcester, MA.
 Master of Science in Material Science and Engineering, May 2006.
International Christian University, Tokyo, JAPAN.
 Bachelor of Arts in Physics, June 2003.
- Experiences** **Teaching Assistant, Rutgers University**, Piscataway, NJ, January-May 2007.
Teaching Assistant, Worcester Polytechnic Institute, Worcester, MA, November 2004 - June 2006.
Science instructor, Galileo Workshop, Japan, August 2003-May 2004.

Publications

1. **G. Eda**, C. Mattevi, H. Yamaguchi, H. Kim and M. Chhowalla. Insulator to semi-metal transition in graphene oxide. Under review at *J. Phys. Chem. C*.
2. H.E. Unalan, Y. Zhang, P. Hiralal, S. Dalal, D. Chu, **G. Eda**, K.B.K. Teo, M. Chhowalla, W.I. Milne and G.A.J. Amaratunga. Zinc oxide nanowire networks for macroelectronic devices. *Appl. Phys. Lett.* (2009) In press.
3. C. Mattevi, **G. Eda**, S. Agnoli, S. Miller, K.A. Mkhoyan, O. Celik, D. Mastrogiovanni, G. Granozzi, E. Garfunkel and M. Chhowalla. Evolution of electrical, chemical, and structural properties of transparent and conducting chemically derived graphene thin films. *Adv. Funct. Mater.* (2009) In press.
4. Y.-Y. Lin, S. Miller, B.B. Parekh, **G. Eda**, G. Fanchini, C.-W. Chen, W.-F. Su and M. Chhowalla. Correlation of open circuit voltage with the work function of transparent and conducting single wall nanotube thin film in organic photovoltaics. Under review at *Org. Elec.*
5. **G. Eda** and M. Chhowalla. Graphene-based composite thin films for electronics. *Nano Lett.* **9**, 814-818 (2009).
6. K.A. Mkhoyan, A.W. Contryman, J. Silcox, D.A. Stewart, **G. Eda**, C. Mattevi, S. Miller and M. Chhowalla. Atomic and electronic structure of graphene oxide. *Nano Lett.* **9**, 1058-1063 (2009).
7. **G. Eda**, H.E. Unalan, N.L. Rupesinghe, G.A.J. Amaratunga and M. Chhowalla. Field emission from graphene based composite thin films. *Appl. Phys. Lett.* **93** 233502 (2008).
8. **G. Eda**, Y.-Y. Lin, S. Miller, C.-W. Chen, W.-F. Su and M. Chhowalla. Transparent and conducting electrodes for organic electronics from reduced graphene oxide. *Appl. Phys. Lett.* **92** 233305 (2008).
9. **G. Eda**, G. Fanchini, A. Kanwal and M. Chhowalla. Bundling dynamics of single walled carbon nanotubes in aqueous suspensions. *J. Appl. Phys.* **103** 093118 (2008).
10. **G. Eda**, G. Fanchini and M. Chhowalla. Large-area ultrathin films of reduced graphene oxide as a transparent and flexible electronic material. *Nature Nanotech.* **3** 270-274

- (2008).
11. B.B. Parekh, G. Fanchini, **G. Eda** and M. Chhowalla. Improved conductivity of transparent single-wall carbon nanotube thin films via stable postdeposition functionalization. *Appl. Phys. Lett.* **90** 121913 (2007).
 12. **G. Eda** and S. Shivkumar. Bead-to-fiber transition in electrospun polystyrene. *J. Appl. Polym. Sci.* **106** 475-487 (2007).
 13. **G. Eda**, J. Liu and S. Shivkumar. Flight path of electrospun polystyrene solutions: Effects of molecular weight and concentration. *Materials Letters* **61** 1451-1455 (2007).
 14. **G. Eda**, L. Liu and S. Shivkumar. Solvent effects on jet evolution during electrospinning of semi-dilute polystyrene solution. *Eur. Polym. J.* **43** 1154-1167 (2007).
 15. **G. Eda** and S. Shivkumar. Bead structure variations during electrospinning of polystyrene. *J. Mater. Sci.* **41** 5704-5078 (2006).

Patents

- Development of graphene based composite thin films – Provisional Patent Filed on March 15, 2008.
- Transparent and conducting graphene thin films by solution processing – Provisional Patent filed on Sept 8, 2007.